INTEGRATED MICROSYSTEM TECHNOLOGIES FOR CONTINUOUS PERSONAL MONITORING OF AIRBORNE POLLUTANT EXPOSURES

By

Heyu Yin

A DISSERTATION

Submitted to
Michigan State University
in partial fulfillment of the requirements
for the degree of

Electrical Engineering – Doctor of Philosophy

2021

ABSTRACT

INTEGRATED MICROSYSTEM TECHNOLOGIES FOR CONTINUOUS PERSONAL MONITORING OF AIRBORNE POLLUTANT EXPOSURES

By

Heyu Yin

Exposure to airborne pollutants, including gaseous toxins and particulate matter (PM), threaten human health and are of growing world concern. Unfortunately, the specific mechanisms behind medical conditions induced by air pollutants, as well as the socioeconomic demographics that underpin these conditions, are poorly understood. This is due, in large part, to a lack of accurate data detailing exposure profiles of individuals who suffer from acute and chronic health conditions. Air pollution levels and the activities of individuals exhibit a large degree of spatial and temporal variation, which both challenge the assessment of personal exposures. Moreover, health impacts vary significantly with chemical composition and particle size of pollutants, which further complicates effective monitoring. Utilizing a combination of microfabrication, microfluidics and electrochemical sensing technologies, this thesis research explored a microsystem solution to these challenges that can achieve high spatial resolution by providing a compact, mobile/wearable monitoring device and can achieve high temporal resolution by enabling continuous collection of personal exposure data. To create a compact monitor for multiple gaseous air pollutants, unique microfabrication procedures and electrochemical techniques were established, enabling a gas sensor array that features room temperature ionic liquid electrolyte and achieves high reliability and repeatability. In addition, a novel PM monitoring platform that uniquely employs microfluidics to achieve real-time continuous measurement was introduced, and key component technologies were developed.

First, to measure PM concentrations within a compact microfluidic device, an electrochemical quantification method based on the ionic electret effect was employed for the first time using microfabricated planar electrodes and a microelectronic instrumentation module. Second, to permit real-time analysis of PM across a wide range of particle diameters, multiple generations of a microfluidic size fractionation component were developed. The first microfabricated size fractionation device realized the deterministic lateral displacement (DLD) method with a critical diameter of 2.5 μm and was successfully demonstrated to separate 10 μm and 1 μm particles with around 100% efficiency. The next size fractionation design aimed to provide multi-size separation over a wide dynamic range (~1000) of particle sizes that impact human health, down to ultrafine (nanoscale) PM. The resulting externally balanced cascade DLD concept was implemented within a mathematic model that predicts size fractionation of PM, from 10 μm to 0.01 μm, can be achieved with a minimum total device length of ~41mm using a four-section cascade. Finally, to further miniaturize the size separation device toward a monolithic implementation, an internally balanced cascade DLD design concept that can omit extra inputs and outputs was introduced and thoroughly analyzed using computational fluid dynamics simulations. The combined results of this research overcome many challenges that currently impede the desperately needed realization of personal airborne pollutant monitors offering wearable, real-time and continuous operation for unprecedented spatial and temporal resolution.

Copyright by
HEYU YIN
2021

ACKNOWLEDGEMENTS

I would like to express my great gratitude to my advisor, Dr. Andrew J. Mason for his continuing guidance and support through my PhD research. He has been a great teacher for my academic career. He is always very patient and willing to share his knowledge and experiences on multiple aspects, including self-management, critical-thinking, skills of cooperation and communication, and so on. Within the flexible and resourceful research environment that created by Dr. Mason, all these knowledge and skills he taught me will help me to gain further success in the future academic career.

I am grateful to Dr. Wen Li, Dr. Nelson Sepulveda, and Dr. Changyong Cao for their continuous supporting while serving as my committee members. I would also like to thank Dr. Chuan Wang, Dr. Junghoon Yeom, Dr. Baokang Bi, Brian Wright, and all ECE staffs for their continues support to my research.

I would also like to thank my colleagues in HATlab for their support. Thanks to Lin Li, Yuning Yang, Haitao Li, Sam Boling, Sina Parsnejad, Ehsan Ashoori, Yousef Gtat and Sylmarie Davila Montero. It has always been a pleasant experience to work with them. I would also like to thank Yue Huang, Xiaopeng Bi, Bin Fan who helped me work in MSU KECK microfabrication facility.

Lastly and very importantly, I want to thank my parents, my brothers and my girlfriend, Meng Ke, for their amazing love and support. This work is dedicated to them.

TABLE OF CONTENTS

LIST OF TABLES

LIST OF FIGURES

1 Introduction

1.1 Motivation

Exposure to airborne pollutants, including gaseous air pollutants and airborne particulate matter (PM) pollution, is attributed to 1 in 9 deaths worldwide, resulting in 8 million premature deaths each year, due to increased mortality from stroke, heart disease, chronic obstructive pulmonary disease, lung cancer and acute respiratory infections [1]; 88% of these deaths are attributable to airborne particulate matter (PM) with the remainder attributable to gaseous air pollutants [1], [2]. Gaseous air pollutants can drive proallergic inflammation through the generation of oxidative stress, which is regulated by individual generic susceptibility. Recent epidemiologic studies have also provided valuable insight into the association between gaseous air pollutants exposure and the increases in cardiopulmonary mortality, respiratory and cardiovascular hospital admissions [3], [4]. Meanwhile, airborne PM pollution, especially fine particles with a diameter of 2.5 um or smaller (PM2.5) which can penetrate the thoracic region of the respiratory system and ultrafine particle with a diameter smaller than 1um, has cause severe air quality issues that threaten human life and increase hospital admission and emergency department visits which in further will contribute to global mortality [1], [2].

Gaseous air pollutants typically include sulfur dioxide (SO_2), nitrogen dioxide (NO_2), carbon monoxide (CO), and volatile organic compounds (VOCs) as well [5]. PM pollution, standing for a mixture of solid particles and liquid droplets suspended in air, typically include both coarse particulate matter (PM10), fine particulate matter (PM2.5), and ultrafine particulate (UFP). Both of these pollutants present a tremendous risk to human health and life, and they also create a significant economic burden associated keeping exposure, both short and long term, to air pollutants below safe levels defined by the Air Quality Index. However, due to the **lack of data that accurately relates an individuals' daily exposure** to acute and chronic

health conditions, the specific mechanisms behind medical conditions induced by air pollutants, as well as the socioeconomic demographics of these conditions, are poorly understood. For example, the mechanisms of how exposure to air pollutants drive proallergic inflammation and induce cardiopulmonary disease, such as asthma and allergic rhinitis, are still undetermined [6]. Furthermore, increasing concerns exist for the ultrafine particles (UFP), those less than 100 nm in diameter that are known to be more toxic than larger particulates, though the effects of UFP on health are not yet well understood [7]. Currently, the COVID-19 pandemic, arousing from the spread of the COVID-19 virus (can be categorized as UFP), is continuously ruining the society and threatening human health all over the world. Evidence suggests that long-term exposure to particulate is associated with higher COVID-19 spread and mortality rates [8], [9], especially for indoor environment [10]. However, the determination relationship between exposure to air pollutant and the mortality rate and spread of COVID-19 as well as how the COVID-19 infection transmitted via aerosols is still under study [11], [12].

In order to help collect data to advance scientific understanding of airborne pollution effects, technologies and methodologies resulting in a low cost, compact system to continuously monitoring airborne pollutants concentration would offer a desperately needed and currently non-existent air pollution exposure assessment tool for the determination and characterization of personal exposure to both airborne PM and gaseous air pollutants. This breakthrough in understanding air pollution will allow for what has become an urgent need: highly effective air pollutant regulation, real-time personal exposure management, direct intervention for those individual's most susceptible to the effects of exposure, and ultimately vast reduction of the burden of disease currently inflicted worldwide by air pollution exposures.

1.2 Challenges

Health effects and economic effects associated with airborne pollution are typically

evaluated using a single pollutant approach, yet realistically most people are exposed to mixtures consisting of multiple pollutants (including multiple toxic gases, multiple size fractions and chemical components of PM) that may have independent or combined impacts on health [13]. Individuals especially susceptible to air pollution exposure include those with pre-existing disease, as well as children and the elderly. While over 90% of the world's population lives where air pollution exceeds the World Health Organization (WHO) guideline limits [1], the burden of ill-health from air pollution has distinct spatial disparities. Most of the disease burden is borne by low- and middle-income countries, as well as poor and marginalized populations who tend to live near busy roads and industrial sites characterized by high levels of ambient air pollution. Furthermore, exposures often vary greatly over time, especially for individuals in close proximity to pollution emission sources, such as in cities and some indoor microenvironments. Assessing personal exposure in these areas offers several challenges where both the individual's activities and air pollution levels demonstrate a large degree of spatial and temporal dynamics. Thus, the spatial and temporal variability of urban air pollution levels in combination with indoor exposures and individual's time-activity patterns are key elements of accurate personal exposure assessment [14].

Despite the strong need for high spatial and temporal resolution in air pollution measurement, existing monitoring systems rely largely on the national stationary (e.g., roof top) monitoring stations that do not allow real-time assessment of PM exposures and are typically limited to only one or a few PM sizes and cannot provide real-time data on the elemental components of PM. There were some emerging technologies that try to improve spatial and temporal resolution. However, these methods have limited spatiotemporal resolution and are also limited to only one or a few PM sizes and cannot provide real-time analysis of the elemental components of PM. The challenges to achieving reliable personal air pollution exposure monitoring can be summarized as:

1) how to develop an affordable/low-cost, autonomously operated airborne pollution monitoring system with the capability to provide high spatial resolution;

2) how to develop airborne pollution assessment system with the ability to collect monitoring data with high temporal resolution;

3) how to build a system that can provide promising sensitivity and reliability and analytical capability across diversity of gaseous and PM pollutants.

1.3 Approach and Thesis Goals

The main objective of the thesis is to overcome the challenges described above by advancing the technologies for continuous personal exposure management of airborne pollutants. Currently, the lack of monitoring tools capable of personal, real-time assessment of multiple exposure factors greatly impedes the thorough study of exposure and its health impacts. Such tools would enable successful realization of well-informed interventions to reduce air pollution exposures and improve health of vulnerable and disproportionately impacted individuals, through effective policy and regulation (e.g., identification and reduction of contributing emission source sectors, changes to personal behavior/activity patterns). In contrast to existing airborne pollutant monitoring, with the development of microfabrication technology, such as the micro-electromechanical systems (MEMS) technology, a microsystem (can be defined as a miniaturized system that are capable to be wear by individuals) utilizing the advanced microfabrication and integration process can provide a unique and beneficial approach to develop a easily used, wearable, real-time continuous airborne pollutant monitoring system with high spatiotemporal resolution to study the health impacts in personal pollutant exposure management application.

To achieve the main objective, the proposed airborne monitoring system would have the

combined features of 1) high-sensitivity, good reliability (to enable data accuracy of the daily air pollutant concentration both indoor and outdoor); 2) real-time continuous monitoring (to enable high temporal resolution); and 3) autonomous, wearable, low-cost, low-maintenance implementation (to enable wide distribution to a network of individual users permitting high spatial resolution). Thus, the goals of this thesis research are summarized as:

1) develop a new miniaturized compact platform that is capable of continuous airborne pollutants monitoring in real-time providing valid temporal resolution and capable to be wearable by individuals across wide spectrum to provide adequate spatial resolution as well.

2) advance the technologies that will enhance the performance of the real-time continuous air pollutants monitoring system that enable high spatiotemporal resolution in a miniaturized format, avoiding accumulation of PM that adopted by most methods.

1.4 Thesis Outline

In this thesis, Chapter 2 covers the background and literature review of airborne pollutants monitoring sensors, CMOS electronics, packaging and microfluidics. Chapter 3 states our efforts to develop the RTIL gas sensor for gaseous air pollutants monitoring. Chapter 4 specifies our design for real-time continuous PM monitoring system. Chapter 5 presents the first generation of the development of the key microsystem technologies, including the electrochemical quantification and the DLD based size fractionation. Chapter 6 specifies the model of externally balanced Cascade DLD design for multi-size separation analysis. Chapter 7 presents the numerical analysis of internally balanced multi-size Cascade DLD design and Chapter 8 covers summary, contributions and future work.

2 Background

2.1 Introduction to Airborne Pollutants

Airborne pollutants, a well-known term, typically refers to the atmosphere of various gases, finely divided solids, or finely dispersed aerosols at rates that exceed the natural capacity of the environment to dissipate and dilute or absorb them and therefore cause undesirable health, economic or aesthetic effect. Although the awareness of air pollution has been increased, what air pollution is and what all categories are still not precisely defined as the understanding of air pollutants advances [15]. The Clean Air Act requires EPA to set National Ambient Air Quality Standards (NAAQS) for six common air pollutants, including ground-level ozone, particulate matter, carbon monoxide, lead, sulfur dioxide, and nitrogen dioxide, which is also known as "criterial air pollutants" [16]. As understanding of airborne pollutants advances, such as how outdoor and indoor pollution differ from each other, how anthropological activities change the air pollution, nowadays the definition of airborne pollutants can vary for different studies. Aim at studying how airborne pollutants affect human health, following the guidelines for human exposure assessment [17]–[19], in this thesis work, the focus is on two categories of airborne pollutants: gaseous air pollutants and particulate matter (PM).

2.1.1 Gaseous Air Pollutants

Gaseous air pollutants are emitted from various natural sources, such as volcanoes and forest fires, and anthropogenic emissions which play a more and more important role due to the population growth and industrialization. The principle gaseous environmental pollutants identified by the EPA's National Ambient Air Quality Standards include NO_2 (nitrogen dioxide), CO (carbon monoxide), O_3 (ozone) and SO_2 (sulfur dioxide) [20], and exposure to such airborne toxins are a leading cause of global illness and mortality [21]. Furthermore, flammable and explosive gases including O_2 (Oxygen), H_2 (Hydrogen) and CH_4 (Methane) need to be

observed regularly for occupational safety. It is well known that, under an atmospheric inversion, in which a layer of ground-level cool air is stable and calm when it is trapped beneath a higher layer of warmer air, the gaseous air pollutants can be especially severe. Furthermore, if an atmospheric inversion is accompanied by fog, a so-called “killer smog’s” rich in gaseous air pollutants will be formed that can cause the deaths of thousands of people. The most famous example is the “Great Smog of London” that occurred in early December 1952 [22]. The physical and chemical properties of the gaseous air pollutants can be extremely complicated. In this thesis, only emission, transformation, as well as the toxicity, which directly related to the human health effect, will be reviewed in section 2.2.1.

2.1.2 Particulate Matter

Particulate matter, PM, (also called particle pollution) is a term for a complex mixture of solid particles and liquid droplets found in the air. Since the component of PM is extremely complicated and the shape of PM is irregular, we typically categorize PM particles by aerodynamic properties. Some particles, such as dust, dirt, soot, or smoke, are large or dark enough to be seen with naked eye. Others are so small that they can only be detected with specific instrumentation. Based on the aerodynamic diameter, as classified by EPA, particle pollution includes: PM10, inhalable particles, with diameters that are generally 10 micrometers and smaller; PM2.5, fine inhalable particles, with diameters that are generally 2.5 micrometers and smaller; and ultra-fine particles (UFP), with diameters that are smaller than 0.1 micrometers. The aerodynamic properties not only determine how the particulate are transported in air but also govern how far they can get into the air passages of human respiratory system which also determine how PM affect human health.

Components of PM include finely divided solids or liquids such as dust, fly, ash, soot, smoke, aerosols, fumes, mists and condensing vapors, that can be suspended in the air for

extended periods of time [23]. And chemical constituents of PM can even be more complicated, including inorganic ions (e.g., nitrates; sulfates); elemental and organic carbon; organic compounds (e.g., polycyclic aromatic hydrocarbons); biological compounds (also named as bioaerosols, e.g., endotoxin, cell fragments, fungal spores, pollen, animal dander, bacteria and virus [24], [25]); and metals and trace metal compounds (e.g., arsenic, beryllium, cadmium, chromium, lead, manganese, iron, copper, nickel, zinc, and vanadium) [26][27]. For example, soot (largely elemental carbon and organic carbon) and trace metals (including arsenic, beryllium, cadmium, chromium, lead, manganese and nickel compounds) are part of the "air toxic" PM components identified by the U.S. EPA as having the strongest potential connection to adverse health responses.

Originating from variety of either stationary or mobile sources, PM can be formed directly from primary emissions (categorized as primary source) and indirectly from secondary emissions (categorized as secondary source) via atmospheric transformation. Primary PM sources can be derived from both human and natural activities. Even natural sources, more specifically refer to nonanthropogenic or biogenic sources, contribute to overall PM exposure, human or anthropogenic activities, such as agricultural operations, industrial process, combustion of wood and fossil fuels, construction and demolition, occupy significant portion of PM [23]. Differ from primary sources, secondary PM sources emit air contaminants into atmosphere that form or help form PM through complicated process instead. Those air contaminants, also named as secondary pollutants including SOx, NOx, VOCs, ammonia, and so on, are considered precursors, which will go through the nucleation and growth (or condensation) process to form the PM [28]. For example, trace metals and elemental carbon are of particular concern due to their widespread emission from fossil fuel combustion and industrial processing. Therefore, elemental carbon characterization is a useful tool for source (e.g., diesel emission) identification. Importantly, elemental carbon and trace metals are present

in PM primarily as insoluble components. Personal exposure studies of these components, particularly in the ultrafine size range, have been extremely limited due to the lack of effective personal exposure assessment technology. Even though our understanding of PM formation and its impact on the human health and global climate is very limited, control measures that reduce direct PM emissions and PM precursor emissions tend to have a beneficial impact on ambient PM levels. In order to help people to be aware of what particle pollution levels are in their city or country, EPA have disclosed the air quality index (AQI) as a standard, as shown in Table 2.1 [29]. In this standard, air quality monitors measure PM2.5 and PM10 concentration in μg/m3, index and colored ranges provide indicators of the quality of the air and its health effects to help people take actions to protect their health when particle pollution is high.

Table 2.1. Typical table of air quality index (AQI) which helps to provide indicator of the quality of the air and its health effects

AQI	**$PM_{2.5}$ ($\mu g/m^3$)**	**PM_{10} ($\mu g/m^3$)**	**Air Quality Descriptor**
0-50	0.0-15.4	0-54	Good
51-100	15.5-40.4	55-154	Moderate
101-150	40.5-65.4	155-254	Unhealthy for Sensitive Groups
151-200	65.5-150.4	255-354	Unhealthy
200-300	150.5-250.4	355-424	Very Unhealthy

2.2 Air Pollutants Health Effects and Economic Impact

2.2.1 Gaseous Air Pollutants Health Effects and Economic Impact

Gaseous airborne pollutants are known to threaten human health and safety, causing discomfort, illness, and even death, particularly among susceptible individuals such as those with pre-existing cardiovascular or respiratory problems as well as infants and the elderly [21],

[30]. As a summary, gaseous air pollutants mainly include: 1) sulphur gases, 2) nitrogen gases, and 3) organic gases and vapours [22], [31].

Sulphur pollutant gases mostly refer to colourless but pungent smell sulphur dioxide (SO_2) and hydrogen sulphide (H_2S). Volcanoes and wildfires are the main natural sources of emission for sulphur gases, which on average emit about 12 million tons of sulphur gases per year, of which 90% is SO_2 and 10% is H_2S. In contrast, in case of fossil-fuel combustion, global anthropogenic emission of SO_2 only is about 150 million tons per year, which is about 3.8 times the natural releases [22]. Although human is less sensitive to SO_2 and H_2S than plants, studies show that both short-term and long-term exposure could cause human to suffer asthma or other distresses related to impaired lung function [3], [32]. Moreover, after emitted to the atmosphere, sulphur gases could become oxidized to form so called atmospheric sulphate, which can combine with positively charged ions to form various compounds, such as sulphate particulate aerosols. And these sulphates particulate matter which are ultimately derived from gaseous sulphur could result in the incidence of respiratory and circulatory disease that will be reviewed in section 2.2.2.

The most important nitrogen air pollutants include nitric oxide (NO), nitrogen dioxide (NO_2), nitrous oxide (N_2O), and ammonia (NH_3), emitted from anthropogenic process, mainly fossil-fuel combustion and agriculture soil fertilization, and animal husbandry. Short-term exposure to NH_3 and NO_x in an occupational setting in ppm level can cause impaired pulmonary functions in humans [33]. Moreover, because most atmospheric NO_x become oxidized to nitrate (NO_3^-) that will not only affect acidification of precipitation and ecosystems but also disrupt the Alveolar structures and their function in lungs after diffusion. The environmental damage and human health impact associated with nitrogen gaseous pollutants can be even more severe through long-term exposure [22], [32], [33].

Organic gases and vapors pollutant include hydrocarbons (such as NO, CH_4), volatile organic compounds (VOCs, such as benzene, formaldehyde, aldehyde, phenol), and ozone as well. Most emission of methane are natural and associated with the fermentation of organic matter, while atmospheric hydrocarbons other than methane are emitted from both natural sources (about 200 million tons per year) and anthropogenic activities (about 186 million tons per year, mostly from unburned fuel emitted from vehicles and aircraft which releases during fossil-fuel mining and refining, and evaporation of solvents) [18], [22]. Organic gases and vapors can be toxic to human in an occupational setting of ppm level. Moreover, these gases play a very important role in the photochemical reactions that produce toxic ozone. Ozone in the troposphere (ground-level ozone) is the most damaging photochemical air pollutants, only slightly less than peroxyacetyl nitrate and hydrogen peroxide. Humans, exposure to ozone in ppb level both long-term and short term could suffer from irritating and damaging membranes of the eyes and respiratory system which then will cause a loss of lung functioning [3].

2.2.2 PM Health Effects and Economic Impact

Although the direct connection between PM exposure and health impact is not fully understood, growing number of studies in toxicology, epidemiology and other related fields have demonstrated that PM exposure are closely related to incidence of morbidity and mortality increasing. Especially for infants, elders and people with heart or lung disease, numerous scientific studies have explained PM exposure as the source of various health problems [34]. Airborne PM observed from both indoor and outdoor environment, especially for those form from secondary sources, consists of heterogeneous mixture of solid and liquid particles that suspended in air and will penetrate into human respiratory system. This penetration into the respiratory system has been reported to be responsible for more than 2 million deaths occurring globally each year [27], [35].

PM10, PM2.5 and UFP are inhalable particles and PM10 are likely to deposit in the tracheobronchial branch of lungs while PM2.5 and UFP can penetrate deeper into the respiratory bronchioles and alveoli through human respiratory system when exposed to PM. These particles can further penetrate into blood stream and cause asthma, respiratory inflammation, jeopardize lung functions, promote cancer and cardiopulmonary disease (CPD), which are the causative factors of human non-accidental death [34], [36]–[38]. Moreover, intake or infection of the COVID-19 virus, which can be categorized as an aerosol-transmitted ultrafine bioparticle, will directly disturb human's immune system resulting extremely high mortality rate, not to mention the worldwide economic and social impacts [39], [40]. Even susceptibility to PM pollution may vary with health or age, the health effects of inhalable PM (mainly for PM10 and PM2.5) are well documented by WHO that the risk has been shown to increase with exposure to PM pollution over both short term (hours, days) and long term (months, years) indoor and outdoor. There is little evidence to suggest a threshold below which no adverse health effects would be anticipated [26]. More specifically, these health effects include respiratory and cardiovascular morbidity, such as aggravation of asthma, respiratory symptoms and an increase in hospital admissions and mortality from cardiovascular and respiratory diseases from lung cancer. The daily mortality is estimated to increase by 0.2–0.6% per 10 μg/m3 of PM10 while long-term exposure to PM2.5 is associated with an increase in the long-term risk of cardiopulmonary mortality by 6–13% per 10 μg/m3 of PM2.5 [41]–[46]. Moreover, susceptible groups with pre-existing lung or heart disease, as well as elderly people and children, are particularly vulnerable. It is estimated approximately 3% of cardiopulmonary and 5% of lung cancer deaths are attributable to PM globally, and exposure to PM2.5 reduces the life expectancy of the population of the region (eastern Europe, Caucasus and Central Asian) by about 8.6 months on average [26][46]. However, how ultrafine particles (UFPs) affect human health is not well understood despite the fact that many toxicological studies have

attempted to determine the toxicology of UFP [47]–[49].

2.3 Gas Sensor Technologies Review

Personal exposures to gaseous air pollutants vary significantly in different locations and over time, requiring rapid assessment of gas concentrations for vulnerable individuals. To avoid such threats, variety of portable, low cost, low power, multi-gas sensing technologies suitable for constantly examining the personal surrounding environment have been developed. There are different types of prevalent gas sensing technologies meeting the requirements, including: gas chromatography (GC)-based [50], non-dispersive infrared (NDIR) [51], metal oxide semiconductor [52], conductive polymer [53], MEMS cantilever [54], [55], thermoelectric [56], [57], acoustic resonator [58], bioluminescent [59], chemiresistor [59], [60], chemical field effect transistor (chemFET) [61], electrochemical gas sensing technologies [53], [62] and so on. These technologies have demonstrated capability for sensing multiple airborne quantities of interest. However, several drawbacks are inherent with these existing sensor technologies and/or their on-CMOS sensor fabrication processes. For example, the bioluminescent gas sensor requires an external light source and thus is not a fully monolithic approach; chemiresistor gas sensors suffer significantly from baseline drifts; and cantilever thermoelectric and metal oxide-based gas sensors require high temperature operation that limits battery life for portable applications. Moreover, the bulk MEMS processes used to fabricate cantilever thermoelectric, metal oxide and chemFET-based gas sensors add process complexity that negatively impact device cost.

A detailed comparison among five technologies with the pros and cons summarized is shown in Table 2.1. GC-based sensing technology has been reported to achieve high sensitivity, selectivity, and reliability, but with the disadvantages of typically bulky, expensive, and requiring complex operations and regular maintenance. Although the micro-GC have been

developed, high degree of complexity and sophistication resulting in high production cost is still a challenge [50]. NDIR sensing technology that determining the absorption of an emitted infrared light source through a certain gas also suffers from the expensive and high-power consumption issue [51]. In comparison, metal oxide semiconductor gas sensing technology have advantages including light weight, miniaturized size, quick response time and low cost. However, the requirement of high operation temperature (typical >250 °c) not only limit its applications but also results in high power consumption [52]. Conductive polymer sensing technology, which uses different types of conductive polymer to absorb or react with gases, shows advantages including high sensitivity, short response time, low fabrication cost, but suffers from low selectivity, long-term instability and irreversibility [53]. Electrochemical sensing technology have been proven to be able to detect almost all gaseous air pollutants with high sensitivity, good selectivity, low power consumption, wide dynamic range, and low cost [50].

The performance parameters in Table 2.2 are chosen to represent the metrics important to wearable monitoring of personal air pollutant exposure. Among all compared gas sensing technologies, electrochemical sensors exhibit the best combination of strength, to perform gaseous air pollutant monitoring for individuals. Thus, electrochemical sensors are the starting point for the gas sensor designed and implemented in Chapter 3.

Table 2.2. Comparison of gas sensor technologies

	Sensing technology				
Performance parameters	GC based	NDIR	Metal oxide semiconductor	Conductive polymer	Electrochemical
Detectable air pollutants(CO, NO, NO_2, SO_2, O_3)	All	Most	Most	Several	All
Selectivity	Excellent	Good	Good	Bad	Good
Reliability	Excellent	Good	Moderate	Bad	Moderate
Cost	Very high	High	Low	Low	Low
Responding time	Slow	Fast	Fast	Fast	Moderate
Size	Medium	Large	Small	Small	Small
Power consumption	Very high	High	High	Low	Low

2.4 PM Monitoring Technologies Review

2.4.1 Existing PM Monitoring Systems

The National Ambient Air Quality Standards (NAAQS) reports that long-term PM exposure-related mortality risk, short-term PM exposure-related mortality and morbidity risk remaining, as well as the PM-related welfare effects due to the PM effects on visibility, climate, materials and ecological determination, are remaining the top concern. The health risk and welfare effects from PM pose the requirement for efficient scientific solution for PM pollution abatement and monitoring [63]. Collecting appropriate scientific and technical information available to support quantitative assessments is critical in the integrated science assessment development process. The significance of PM exposure assessment, PM monitoring guidelines posed by EPA and NIOSH, as well as existing PM monitoring systems will be reviewed in this section.

2.4.1.1 Significance of PM Exposure Assessment

Ambient PM is a very complex mixture: it is derived from multiple sources and is comprised not only of primary emissions from stationary and distributed sources, but also from secondary aerosol formed via atmospheric transformation, resulting in highly variable

distributions of PM chemical components across size-fractions. Because of this, it is a challenge to study in epidemiological and toxicological settings. While air quality standards exist for PM10 and PM2.5, health impact analyses are currently insufficient to inform the development of guidelines or standards for ultrafine particles, primarily due to constraints posed by the lack of personal exposure monitoring technology for PM size fractionation and quantification. Likewise, while the U.S. EPA has identified a set of "air toxics" (which include several metals), that pose the greatest potential health threat in areas where both exposures and risk peak due to large population centers. These exposure and health relationships have been poorly studied due to extreme limitations in the personal exposure assessment technologies available to date for classification of PM chemical composition. Most research to date has focused on ambient PM mass and has not involved extensive exposure characterization regarding the effects of specific PM sources, size-fractions, and elemental components on human health. PM is currently regulated on a mass basis, which incorrectly assumes that all particles are toxicologically identical. In order to determine the most effective way to regulate PM and ensure that reductions in PM do improve human health, additional data across PM size-fractions and elemental components are required.

PM exposures vary in both time and space depending on an individual's location relative to the contaminant source, the time of day, lifestyle, and other factors [14]. While studies have linked some chronic exposures to PM with adverse health effects, acute exposures (on time scales of hours) to PM have also been linked with health problems occurring over short time frames. While federal reference methods (FRMs) and federal equivalent methods (FEMs) exist for stationary site monitoring of criteria pollutants on hourly time scales, reliable personal exposure measurement methods over short time scales (~1 min) do not currently exist for most size-fractionated PM and components. In addition, existing non-FRM and non-FEM methods require long time integration periods (~1 day), and because of cost and equipment size

constraints, offer little to no applicability for mobile personal exposure measurements. Therefore, to achieve more effective regulation and health interventions, there is an urgent need for a low-cost, portable, monitoring tool which is capable of personal, real-time assessment of multiple pollutant exposures to enable the thorough study of exposure and its health impacts.

2.4.1.2 PM Monitoring Guidelines

In the global context, short-term and long-term exposure to both indoor and outdoor PM is and will create a heavy burden of health effects. The World Health Organization (WHO) has developed the air quality guidelines for PM to provide exposure-response relationships which help to build up the standards for PM monitoring [26]. In America, the Occupational Safety and Health Act of 1970 (Public Law 91-596) charged the National Institute for Occupational Safety and Health (NIOSH) with the responsibility for the development and evaluation of sampling and analytical methods for workplace compliance determinations[64][65]. Detailed experimental procedures and analytical data for air sampling and analytical method development and evaluation are shown in the federal guidelines for air sampling and analytical method [65]. In recent years, a large body of new scientific evidence has emerged to strengthen the link between ambient PM exposure and health effects and pose more attention to UFP from both indoor and outdoor that justifies reconsideration of those existing standard guideline. However, this guideline, which includes endpoints to set up the baseline as the standard, still can be considered as a starting point for the PM monitoring research. These methods for measuring ambient concentration of specified air pollutants, published by Environmental Protection Agency (EPA) and NIOSH, can be found in the listed designated reference methods and the NIOSH manual of analytical methods (NMAM) [66], [67], have been designated as “reference methods” or “equivalent methods” in accordance with Title 40, Part 53 of the Code of Federal Regulations (40 CFR Part 53) [68]–[70].

2.4.1.3 Stationary PM Monitoring Tools and Guidelines

The most popular method for PM assessment involves capturing PM at stationary sites and subsequently analyzing samples in a chemistry lab. Stationary air monitoring sites utilize bulky equipment to sample PM over an extended time, e.g. one day, into physical filters. The filters allow particles of a specific size fraction to be captured, and multiple filters can be used to capture PM at different size fractions. Existing stationary monitoring sites typically only capture PM10 and PM2.5. To collect PM within the filters, different solid sorbents have been used, such as activated charcoal, silica gel, porous polymers, synthetic sorbents, coated sorbents, molecular sieves and thermal desorption [67]. After sampling, the filters are taken to a remote laboratory where PM is extracted, and its concentration and chemical composition are analyzed using complex instrumentation and chemical processing. EPA and NIOSH will do the subsequent air sampling and components analysis in chemical labs following the NIOSH Manual of Analytical methods (NMAM) [67], which typically utilize those expensive and bulky equipment.

Following the EPA and NIOSH guidelines, US EPA Monitoring and Quality Assurance Group created the National Air Monitoring Stations (NAMS) network to provide nationally consistent data for assessment of trends. According to the report, the EPA anticipates almost 300 monitoring sites with 54 NAMS installed to determine long-term trends of selected PM2.5 constituents and an additional 250 state and local air monitoring stations will be used to enhance the trends network [68]. In these stationary air monitoring stations, a variety of designated reference or equivalent methods have been used, several of which are extensively adopted to evaluate the performance of newly designed PM monitoring systems, which are summarized in Table 2.2 [ref].

Table 2.3. List of designated reference and equivalent methods for the determination of suspended particulate matter in the atmosphere (high-volume method)

PM10		
Monitor	**Specification**	**Manual reference method (RFPS) or equivalent method (EQOM)**
Andersen Model RAAS10-100/200/300 PM10 Single/Multi Channel PM10 Sampler	Configured as a PM10 reference method and operated for a continuous 24-hour sample period at a flow rate of 16.67 Lpm, and in accordance with the Model RAAS105-100 Operator's Manual and with the requirements and sample collection filters.	RFPS-0699-130
BGI Incorporated Model PQ100/200 Air Sampler	Configured as a PM10 reference method for a continuous 24-hours sample period at a flow rate of 16.7Lpm with original firmware.	RFPS-1298-124
DKK-TOA Models FPM-222/222C, FPM223/223C, and DUB-222(S)/223(S) PM10 Monitor	For monitoring PM10 in ambient air (beta attenuation monitor), configured for PM10 with firmware.	EQPM-0905-156
Ecotech Model 3000 PM10 High Volume Air Sampler	Configured with the Ecotech PM10 size-selective inlet with the flow rate set to 1.13m^3/min (67.8m^3/hour).	RFPS-0706-162

PM2.5		
Monitor	**Specification**	**RFPS or EQOM**
Andersen Model RAAS2.5-200 PM2.5 Ambient Audit Air Sampler	Configured as a PM2.5 reference method and operated with software for a continuous 24-hours sample period at a flow rate of 16.67liters/minute.	RFPS-0299-128
BGI Inc. Models PQ200 or PQ200A PM2.5 Ambient Fine Particle Sampler	Operated with firmware for a continuous 24-hours sample period, in accordance with sample collection filters.	RFPS-0498-116
Environment S.A. Model MP101M PM2.5 Monitor	Environment beta attenuation monitor using a glass fiber filter tape roll, operated at a sample flow rate of 16.67 liters/min for 24-hours average measurements of PM2.5, configured with the standard EPA PM10 inlet associated with a BGI very sharp cut particle size separator and using a temperature regulated sampling tube with ambient meteorological sensor.	EQPM-1013-211
Graseby Andersen Model RAAS2.5-100 PM2.5 Ambient Air Sampler	Configured for "Single 2.5" operation, for a continuous 24-hour sample period at a flow rate of 16.67 liters/minute, and in accordance with the sample collection filters.	RFPS-0598-119

TSP: total suspended particulate matter; more detailed information and more reference methods or equivalent methods can be found.

2.4.1.4 Existing Portable PM Measurement Tools

In contrast to the national stationary station strategy, some companies are trying to develop smaller sized commercially available PM monitors which can help individuals to be aware of the PM status in their surroundings. For example, Libelium have developed their Dust Sensor, which have sample flow rate as 220mL/min and max particle count rate as 10000 particles/second [71]. Although the Dust Sensor can provide abundant dataset due to the fast sampling-rate, the reliability and accuracy is limited since its test results are quite sensitive to environmental variability. Dylos Corporation also have developed the Dylos air quality monitors, which can be utilized to monitoring PM with enhanced accuracy [72]. The Dylos air quality monitors are shielded against Electro-Magnetic interference which means it will count accurately even in close proximity to sources of interference, such as industrial machinery, fluorescent lights, and high voltage power supplies found in some air purifiers. As trying to improve the spatiotemporal resolution with more subtle readout strategy, M-DUST and DFROBOT also have developed those smaller sized air monitors which can be used for PM2.5 and PM10 sampling [73], [74]. Focusing on the system miniaturization, Wynd has tried to develop the wearable PM tracker prototype (retails for $189) [75]. Relying on the signal processing, even with limited size-fractions and accuracy, as claimed, this Wynd system can be facilitated as the “on the go” air quality tracking to provide real-time dataset. Other PM monitors are available commercially, but almost all commercially available PM monitors, are in the price range of $400 to $1000, which is too expensive for personal distribution. Moreover, those commercial PM monitors rely on optical methods, specifically light scattering, where the measurement depends on particle shape, material, refractive index and scattering angles that will limit the measurement accuracy. In addition, as discussed in section 2.4.2, light scattering inherently cannot measure ultrafine particles, provides no real-time information on chemical composition of multi-pollutant exposures, and is very sensitive to relative humidity and other

environmental factors [76].

2.4.2 PM monitoring Methods Developed by Research Groups

The challenge of monitoring PM health impacts has also drawn great interest among the academic community. Rapid advances in both sensor technology and wireless communication provide great opportunities for improved exposure assessment. A wide range of studies have been published to address partial solutions for PM measurement. The main technologies that have been explored to measure the concentration of PM include gravimetric methods, optical methods, and electric methods. In addition, several groups have developed electrophoresis and electrochemical methods to help process PM components classification.

2.4.2.1 Gravimetric Methods

Among the gravimetric methods, a semi-continuous method including tapered-element oscillating microbalance and a quartz crystal microbalance (QCM) have been reported to measure the particle mass indirectly from the captured particles with designated filter [69]. On this semi-continuous method, particulates are accumulated on the oscillating microbalance feature and then the time-integrated particles mass measurement can be recorded with the resonant frequency shift. Following this, a 3D printed virtual impact, which was used to avoid assembly tolerance and maintain accurate alignment, integrated with the microfabricated QCM sensor was also developed to pursuit the low cost, low power consumption, ease of use and good portability purpose [70]. Similar to the QCM structure, a film-bulk acoustic resonator (FBAR) structure was also developed to achieve the wearable PM monitoring purpose [77]–[80]. In this MEMS air-microfluidic PM sensor, an air-microfluidic structure, also named as virtual impactor, was used to perform particle separation; a thermophoretic deposition technology was used to help organize and enhance the particulates deposition and the on-chip FBAR sensor was used to record the particle mass related resonate frequency shift, and

according to the laboratory experiment a 2μg/m3 sensitivity was reported by this MEMS PM sensor. The QCM and FBAR structure utilizing the micro-electro-mechanical-systems (MEMS) fabrication procedure help to reach high resolution, but the particle deposition principal along with the overload, noise, mismatch and maintenance issues stop it to be a candidate for wearable continuous PM monitoring device.

2.4.2.2 Optical Methods

Differ from the gravimetric methods, optical techniques are most commonly used not only in commercial available PM monitors but also in the scientific researched smaller PM sensors [81]. The most popularly used technology is light scattering, in which the sampled particles pass by the air path that is illuminated by a high intensity light source and then a miniaturized photodetector was used to collect the light scattered data from the passed particles. In a forward scatter technology, the light scattering theory can be simply explained as a complex interaction between the incident electromagnetic (EM) wave and the target particles. Imaging particle as a spherical shape, according to Mie scattering theory [82]–[85], the scattering angle from a particle is inversely proportional to particle size and the amount of light scattered is directly proportional to particle size. Following this light scattering theory, if the particle size, particle shape, refractive index and scattering angle are known, the measured scattering intensity from the photodetector can be used to analyze the particle concentration. Most of the bulky instruments, such as the aerodynamic particle sizer (APS 3321, TSI), that were developed to analyze particulate matter are utilizing the modified light scattering setup.

There are several research groups working on the miniaturized compact light scattering PM monitors [84]–[88]. They typically integrated a particle separator, such as impactor which utilizes the inertial sizing topology, working as a filter following with the microfabricated optical particle detector. A modified virtual impactor was designed to work as a large particle

trap that will only allow small particles go to the air pass which is between the incident light and the photodetector [84]. Differ from this design, setting up the cut-point, particles smaller than the cut-point of the virtual impactor will remain in both the major and minor flow which help to direct only targeted small particles flow along the detection channel [88]. Light scattering method rely on the information, such as the particle size, particle shape, refractive index and scattering angle. However, because of the complicated components and PM formation, especially for those PM induced from secondary sources, it is very hard to classify this information and which in further will affect the detection accuracy. Moreover, when the particle size, such as in sub-micron particles, is smaller than the wavelength of the incident light, the scattered light intensity will be too weak to be collected by the photodetector which also sets the detection limitation.

2.4.2.3 Electrical Methods

As classified by NIOSH, particulate matter has different electrical properties, such as the dielectric constant, which can be an option for particle detection. By charging the particles, especially for those submicron particles, the alternative electrical particle detector collects the induced charge from the buildup of the naturally charged particles on a dielectric layer on silicon wafer [89]. Similar to this MEMS resistive sensor developed by Bosch, an on-chip MEMS corona discharger tip is fabricated by anisotropically etching of silicon wafer to apply on-chip particle ionization. Then, the current generated because of the trapping of the ionized particles by the high efficiency particulate air (HEPA) filter will help to provide particle concentration measurement [90], [91]. Following this method, by using the measured current (I), the flow rate (Q), the penetration through the discharger (P), the average number of charges per particle (n), and the electronic charge (e = 1.6× 10-19 C), the number concentration of particles (N, which means particle counts per unit volume) can be determined by the equation:

$Pn = \frac{I}{NeQ}$. Another type of electrical PM sensor is solid-state direct capacitive PM sensor which utilizes the dielectric constant change when particle pass by space between two electrode plate of the capacitor [92]–[99]. The capacitive PM counter with one plane electrode and one mesh electrode is based on condensation of water on particles forming water droplets which are fed to a capacitive type detector. Prior to the CMOS design allowing zeptofarad (10^{-21} F) capacitor resolution, an integrated CMOS monolithic on-chip capacitive micrometric PM detector is presented. Based on the differential capacitive readout design, particle deposition on electrode plate of the on-chip capacitor allow us to collect particle concentration with very high sensitivity. However, this planar capacitive design relies on the particle presence which stop it from evolving toward the real-time continuous PM monitoring application.

2.4.2.4 Electrophoresis and Electrochemical Methods

Another key, and currently not well understood, factor in the toxicity of airborne particulates is its chemical composition, which can vary across both time and space relative to personal exposures. Despite recent research identifying adverse health impacts due to chemical components of PM, PM is currently regulated on a mass basis that does not consider the toxicity of chemical components. Trace metals and elemental carbon are of primary concern for a variety of human health-related and natural environment problems due to their widespread use and emission from fossil fuel combustion, industrial, and waste processes. The U.S. EPA “air toxic” pollutants include several trace metals: arsenic, beryllium, cadmium, chromium, lead, manganese and nickel compounds. Additionally, elemental carbon (EC) characterization across size fractions may serve both as a tool for possible emission source identification, as well as assessment of association with health outcomes. For example, EC is the main constituent of diesel exhaust particulate matter (DPM) and has been identified as a surrogate to monitor DPM. As mentioned in section 2.1, different PM components have different health impacts. For

example, heavy metal ions, such as lead and chromium, were supposed to have more severely toxicity. There are also some technologies developed to target on specific PM components. NIOSH have published the 5th version of the manual of analytical methods (NMAM) which typically relies on filters or different PM samplers to collect PM samples and the following PM components analysis were performed in national chemical labs with different physical or chemical methods [67]. Differ from traditional physical or chemical methods, also relying on the bulky and expensive equipment, the capillary electrophoresis technology with resonant contactless conductometric detector has been used to determined ten water-soluble ions (F^-, Cl^-, NO_2^-, NO_3^-, SO_4^{2-}, K^+, Na^+, NH_4^+, Ca^{2+}, and Mg^{2+}) in PM2.5 samples [100]. Another method that has been popularly used is electrochemical methods. A microfluidic multilayer paper-based analytic device (μPAD) was fabricated by wax printing to perform both colorimetric and quantitative electrochemical detection of particulate metals [96, 97]. The colorimetric detection relies on the designed color changes because of the chemical reactions and the quantitative detection utilizes the square-wave anodic stripping voltammetry (SWASV) method to quantify the metal ions concentrations. Unfortunately, these methods still need complicated sampling process which cannot be easily facilitated in miniaturized platform in real-time.

2.4.2.5 Sensor Network and on Drone Approaches

Technologies, including miniaturization of solid-state sensor, compact instrumentation, as well as the wireless sensors networks (WSN), have been advanced greatly in the past decades, providing the capability to make system small. In order to address the increasing demand for real-time monitoring of air quality with improved spatial resolution, a new monitoring paradigm based on pervasive distribution of the sensor to form dense networks is emerging, in particular within the context of “smart cities” [103]. The proposed possible future ubiquitous and dense PM sensor networks, differ from the traditional PM monitoring approaches based on limited number of fixed or mobile stations, can help to ease the poor spatial resolution issue.

Forming a network with pervasive distribution of PM sensors can be viewed as 2D assessment that only cover the spatial resolution requirement in one direction, which in some cases may not be accurate enough to predict the air quality along the height direction. By fixing the PM sensor on top of drone, also known as unmanned aerial vehicle (UAV), a three-dimensional assessment were also reported, trying to rich the dataset across the height direction [104], [105]. In addition, with the integration of signal processing module and network communication technology, the designed spatiotemporal distribution of indoor particulate quantification with a low-cost sensor network is reported to provide better accuracy of real-time mapping of sources and hotspots of air pollutants in an indoor environment [106]. However, even being capable of enhancing the spatial resolution to some extent, without solving the challenges of personal monitors first, these reported network strategies will not only increase the cost burden but also add risk in accumulating errors.

3 Room Temperature Ionic Liquid (RTIL) Gas Sensor for Personal Gaseous Air Pollutant Exposure Monitoring

Electrochemical gas sensor has many advantages making it well suit for personal real-time gaseous air pollutants monitoring application. However, moderate selectivity and responding time of the electrochemical gas sensor was also reported due to the volatility of the aqueous electrolyte which was chosen in traditional electrochemical gas sensor. The low vapor pressure, electrochemical and thermal stability and high ionic conductivity of RTILs provide outstanding properties for electrochemical gas sensors with long operation lifetimes. Utilizing room temperature ionic liquid (RTIL, a nonvolatile and conductive electrolyte) as the electrolyte, our group has developed a miniaturized RTIL-based electrochemical gas sensor [62]. This sensor could be widely deployed to provide continuous gaseous air pollutant exposure data. This chapter describes work done to improve upon the initial RTIL sensor toward a solution for personal real-time gaseous air pollutants monitoring with high spatiotemporal resolution.

3.1 Our Preliminary Work on RTIL Gas Sensors

In conventional electrochemical sensor structure, electrodes are fabricated on a substrate and the electrolyte is then coated on top of the electrodes. RTIL-based electrochemical sensing technology that utilize the traditional electrochemical sensor structure inherits the outstanding performance of liquid-electrolyte electrochemical gas sensors but suffers slow response due to the slow diffusion of target gases from the RTIL surface to the electrodes. Moreover, such RTIL-based electrochemical sensors suffer from large physical dimensions, long measurement time, and variability due to the sensor manufacturing process that limit their use in point-of-exposure monitoring of gaseous hazards [107]. Because the response time is reciprocal to square of the thickness of electrolyte [108], it can be significantly reduced by thinning the RTIL layer [109]–[111]. However, formation of thin RTIL layer is unstable and irreproducible.

Another way to eliminate the gas diffusion process in RTIL is placing the electrode between gaseous analyte and RTIL layer [112]. By fabricating electrodes directly on a gas-permeable membrane, a planar-electrode-on-permeable-membrane (PEoEM) structure that bypasses the slow diffusion of the gas across the RTIL was designed by our group [113]. The RTIL-based PEoEM gas sensor was sufficiently improving the stability and response time by allowing the gas to pass through the backside of the porous flexible substrate. However, due to the bad adhesion between electrode and substrate layers, the repeatability and the long-term stability of the PEoEM gas sensor is not sufficient to meet the spatiotemporal resolution requirement set for this thesis research. Moreover, redox reactions of gas pollutant analytes are not perfectly reversible, and the unreacted byproducts generate a drift in sensor response which is also a critical problem that needs to be resolved. In addition, in order to enable monitoring of multiple air pollutants, a gas sensor strategy that can selectively identify many target analytes at the same time is needed. The selectivity requirement is addressed in section 3.2, the repeatability and long-term stability challenge is addressed through design of a new gas sensor covered in section 3.3, and the drift issue is addressed through the development of a new electrochemical approach covered in section 3.4.

3.2 Verification of Selectivity in RTIL Electrochemical Gas Sensing Technology

Different gas analytes have different electrochemical redox reactions mechanisms. Choosing electrode materials, RTIL content, and electrochemical bias in specific electrochemical method, is critical to determine the sensor performance. To better understand the mechanisms, collaborating with Dr. Zeng's lab at Oakland University, we have studied the electrochemical activities of multiple analytes, including NO_x, SO_2, CO, ozone, formaldehyde, acetaldehyde, o- nitrobenzene, as well as environmental analytes such as CO_2, O_2 and water. Sensitivity, stability and selectivity of a sensor are determined by sensor design parameters

including electrolyte (RTILs), electrode material and electrochemical method options such as redox potentials and scan rates or AC frequency. Tradeoffs between sensor performance and design parameters were studied through a systematic testing and optimization process. To simplify testing, a macro scale version of the PEoEM-RTIL-based sensor, with an electrode area ~2*2 cm^2, was used. Both short-term, in minutes, and long-term, in months, experiments were performed with sensors exhibiting a combination of different design parameters for the selected target analytes.

The sensor parameter combinations that provide the best sensing performance are listed in Table 3.1. These results demonstrate selectivity for several target analytes and define the materials and methods will be applied to the design of a new miniaturized PEoEM-RTIL-based gas sensor with improved performance. Notice the sensing of each target gas analyte require a specific combination of the design parameters, single sensor cannot monitor multiple gas pollutants simultaneously. A strategy to resolve this challenge is to design a sensor array, which is consist of multiple sensors, with the feature that each sensor utilizes its own design parameters.

Table 3.1. Summary of design parameters for five selected gases

	CH_4	SO_2	H_2	O_2	CO_2
Concentration range	1% - 5%	Above 30 ppm	0.5% - 5%	10% - 21%	0.03% - 0.1%
WE	Pt[1]	Au	Pt	Au or Pt	C or C/Au
RE	Pt or Ag	Pt	Pt or Ag	Pt or Ag	Pt or Ag
CE	Pt or Au	Pt or Au	Pt	Pt or Au	Pt or Au
Ionic Liquid	C4mpy Ntf2	C4mpy Ntf2	C4mpy Ntf2 + 10mM HNTf2 [2]	C4mpy Ntf2	C4mpy Ntf2 + 10mM HNTf2
Measurement methods	Method-1: 0.9V for 600s, then -1.2V for 80s; method-2: switch between 0.9V to -1.2V every 80s.	Constant -1.8 V.	Constant 0.4V.	Constant -1.2V.	Constant -2.5V.
Regeneration or cell maintains	No extra maintain requirement	No extra maintain requirement	Keep temperature lower than 60°C	High temperature could clean the cell	High temperature could clean the cell
Responding time during the concentration change	20-40s	50s	15-30s	20-40s	20-40s
Warm-up time[3]	120s	120s	100s	120s	120s
Data calibration	Method 1 require calibration; method 2 don't require	Require calibration	No calibration required	No calibration required	No calibration required
Selectivity	Good	Interference from O2.	Good	Good	Good
Stability (3 months test)	Good	Good	Good	Reactivation is required	No data

Note: 1. Materials: Au represent gold, Ag represent silver, Pt represent platinum, C represent carbon; 2. $HNTf_2$ is a commercially available and highly versatile super Brønsted acid that can be used to adjust the ionic liquid property; 3. Warm-up time represent the time that required before the data collection.

3.3 Microfabricated Planar RTIL Electrochemical Gas Sensor

As discussed in section 3.1 and 3.2, our preliminary RTIL sensor using the PEoEM structure provides good response time compare to traditional RTIL sensor, and the sensor array strategy can expand the selectivity. In terms of sensor performance including repeatability and long-term stability, the essential design factors have been reported to be: sensor structure [109], [111], electrode geometry [111], [114], [115], electrode position [116], electrolyte viscosity [109], [110], [117], [118], fabrication process, and sensor assembly. The preliminary work did not thoroughly study these design factors. In this section, building upon our preliminary work, design and fabrication of a new microfabricated planar RTIL electrochemical (MPRE) gas sensor with considerations of these factors will be presented.

3.3.1 MPRE Sensor Design

The first factor that need to be considered is the sensor structure. As reported in our work [113], [119], we have developed the MPRE gas sensor on top of porous PTFE structure, as shown in Figure 3.1 (a, b) for the purpose of short response time by allowing the gas reach the electrode-electrolyte interface through the porous substrate. Because the porous PTFE is hydrophobic to RTIL while porous electrode is hydrophilic to RTIL, this backside gas input design can bypass the slow diffusion of gas across RTIL. However, because the porous PTFE is served as the substrate for the following electrode fabrication, both electrode dimension and thickness has to be big enough to maintain good connection which in return will determine the conductivity of the electrode. Moreover, the limited electrode dimension and thickness, as well as the increased electrode surface roughness, will certainly increase the noise level, although the surface roughness do increase the sensing area. As an alternative, as shown in Figure 3.1 (c), a monolithic RTIL gas sensor structure which utilizing the fabricated electrode on top of silicon substrate was also developed to study possible solution to enhance the reliability while sacrifice the response time [120]. The trade-off between two structures has to be studied because the requirements for different applications varies accordingly. Targeting for personal real-time gas pollutants monitoring with good temporary resolution in which the response time is among the top priorities, we will focus on the MPRE on top of porous PTFE structure.

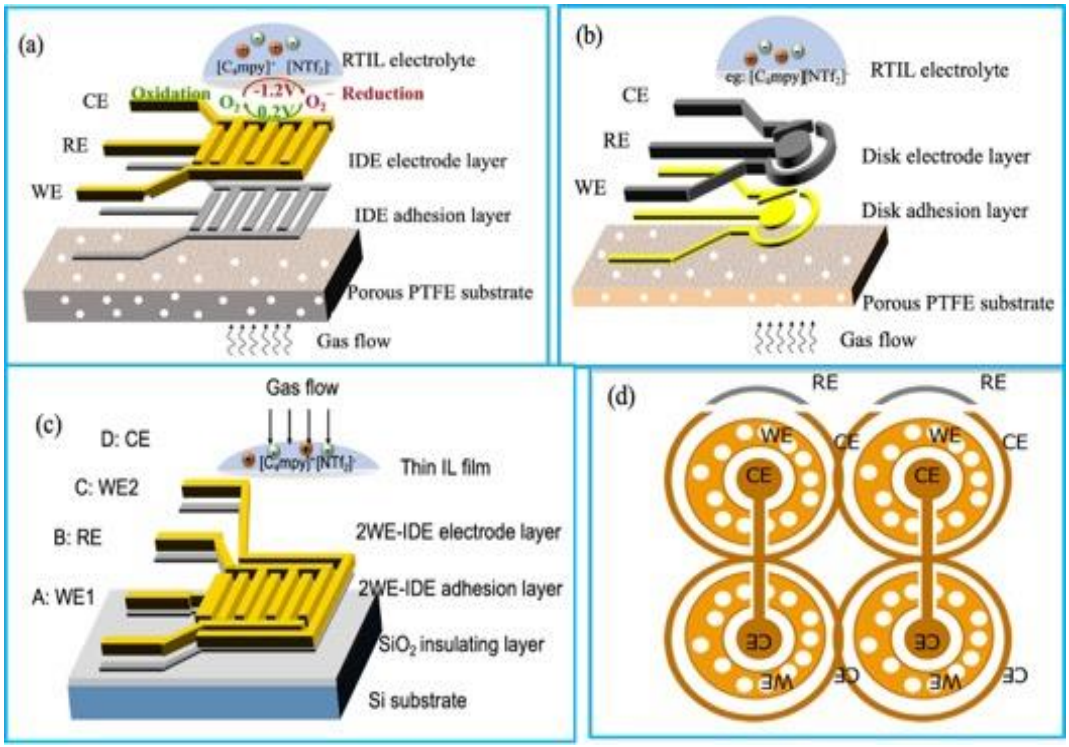

Figure 3.1. (a) interdigitated electrode design; (b) disk-shape electrode design; (c) four electrode structure design; (d) four sites sensor array with shared counter electrode design.

Electrode geometry is also a critical factor that will determine the sensor performance [111], [114], [115]. Disk-shape electrode and interdigitated electrode (IDE) are the most two common electrode geometry choice for a three-electrode electrochemical gas sensor design. Compare to disk-shape design, IDE increases the effective surface-to-volume ratio, which ultimately increase the conductivity, diffusion, and eventually the sensitivity of the sensor [121], [122]. However, in micro scale disk-shape design, mass transport, which means diffusion of the analyte to the WE surface, is controlled by hemispherical diffusion instead of linear diffusion between the electrolyte and the WE surface. It is reported that hemispherical diffusion at micro-disk electrode at a planar structure have shown enhanced mass transport resulting improved sensitivity [112], [123]–[125]. In this chapter, as shown in Figure 3.1 (a, b), for sensor geometry consideration, both interdigitated and disk-shape electrode geometry have been designed and fabricated for the following gas concentration measurements.

For electrode position arrangement, as reported, it is recommended that the reference electrode (RE) be placed outside the current path and near the WE, where the potential distribution is uniform with small IR drop [116]. In this thesis work, we follow the rule to put WE in the middle of WE and CE and try to minimize the distance between WE and RE. As shown in Figure 3.1 (d), we have also designed a new geometry, featuring with shared CE, varied WE-RE distance and porous WE surface, to study both electrode geometry and position arrangement. Consideration for electrolyte viscosity, fabrication process, as well as sensor assembly will be explained in section 3.2.2. To measurement multiple gas simultaneously, electrode array will be designed.

3.3.2 MPRE Sensor Fabrication and Array Assembling

Many traditional microfabrication processes are difficult to perform on porous PTFE substrates due to the flexibility of this material and roughness and porosity of its surface. Based on our prior work [11], PTFE can be affixed to a glass holder to resolve the flexible substrate challenge, and AZ4620 photoresist can be used to form thick layers (~10μm) that permit thin-film metals to be patterned using lift-off on the rough and porous PTFE surface. However, this prior process utilized thermal evaporation for thin-film metal deposition, which introduces high energy metal atoms that can raise the temperature of the PTFE surface higher than 300°C. Above 115°C, PTFE can undergo vitrification, molecular transformation to glass, that introduce stress to the substrate surface that promotes undesired peeling of thin-film metals. Furthermore, it can affect PTFE pour size on the surface that may hinder gas flow through the substrate.

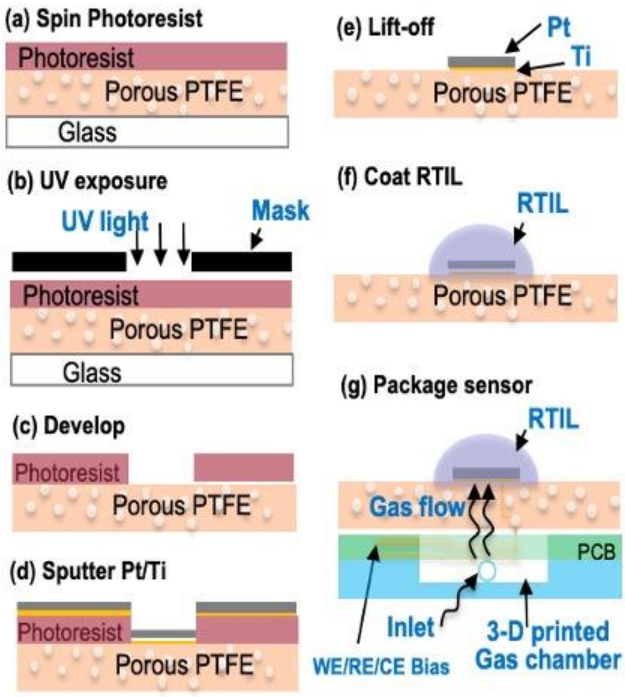

Figure 3.2. Microfabrication process for the MPRE gas sensor.

To improve the shortfalls of our prior process, both magnetron sputtering and Electron-beam evaporation have been tried to enhance the adhesion. Sputtering releases metal atoms through momentum exchange due to collisions rather than heating and results in less heating of the PTFE surface during deposition. Finally sputtering was chosen for thin-film metal deposition rather than thermal evaporation or Electron-beam evaporation. Additionally, following the technique parameter listed in Table 3.1, the electrode metal was changed to platinum for different electrochemical properties, and a titanium adhesion layer was included to further improve reliability of metal attachment to the rough PTFE substrate. Figure 3.2 describes the final microfabrication process used to create the MPRE gas sensor. First, a glass slide was cleaned in oxygen plasma and PTFE with 4μm average pour size (POREX PM23J) was affixed by double- sided tape. Then a 10μm layer of AZ4620 photoresist was spin-coated at 2100 RPM on the PTFE surface, and the desired electrode areas were exposed through a photomask. The glass slide was removed, and the thick photoresist was developed. Then, 50Å titanium followed by 3000Å platinum was deposited via sputtering. This metal thickness was

experimentally determined to form continuous traces on the porous PTFE surface. The planar thin-film metals were then patterned via lift-off of photoresist in acetone overnight followed by ultrasonic vibration for 5 minutes. Following electrode patterning, an RTIL film was deposited on the surface via pipette to cover the electrode sensing area. The RTIL chemical composition can be tailored to different gas targets. For multiple gases (oxygen, methane, sulfur dioxide, ozone) we are interested, 1-butyl-1-methylpyrrolidinium bis-(trifluoromethylsulfonyl)-imide ([C_4mpy][NTf_2]) (viscosity ~ 60 mPa·s, IOLITEC. Inc.) was used as the RTIL electrolyte.

Fabricated electrodes, as shown in Figure 3.3(a, b), were first inspected under microscope to make sure no short circuit or open circuit exist. As shown in Figure 3.3(c, d), optical dimension characterization for both disk-shape electrode and IDE electrode showed that there is ~20-50 μm variation due to the porous substrate. To study the electrode geometry, an interdigitated-disk electrode was also designed and fabricated, as shown in Figure 3.3(e, f). In contrast to etching process which require chemical reaction, lift-off is purely physical pattern process. Because the porosity of the PTFE substrate could induce potential chemical trapping that in further ruin the purity of the RTIL, only lift-off can be chosen as the last step of the electrode fabrication. However, even we typically soak the samples inside acetone overnight with additional 5 minutes ultrasonic process, there were still some Pt residue left among some EB-evaporation fabricated samples leading to a short circuit connection between electrodes, as shown in Figure 3.3(f). One possible reason is the heat accumulation from the thick metal deposition process could change the photoresist property that make it difficult to be resolved by acetone. The Pt residue can be partially removed by increase the ultrasonic power and time carefully without destroy the adhesion between PTFE and the metal layer.

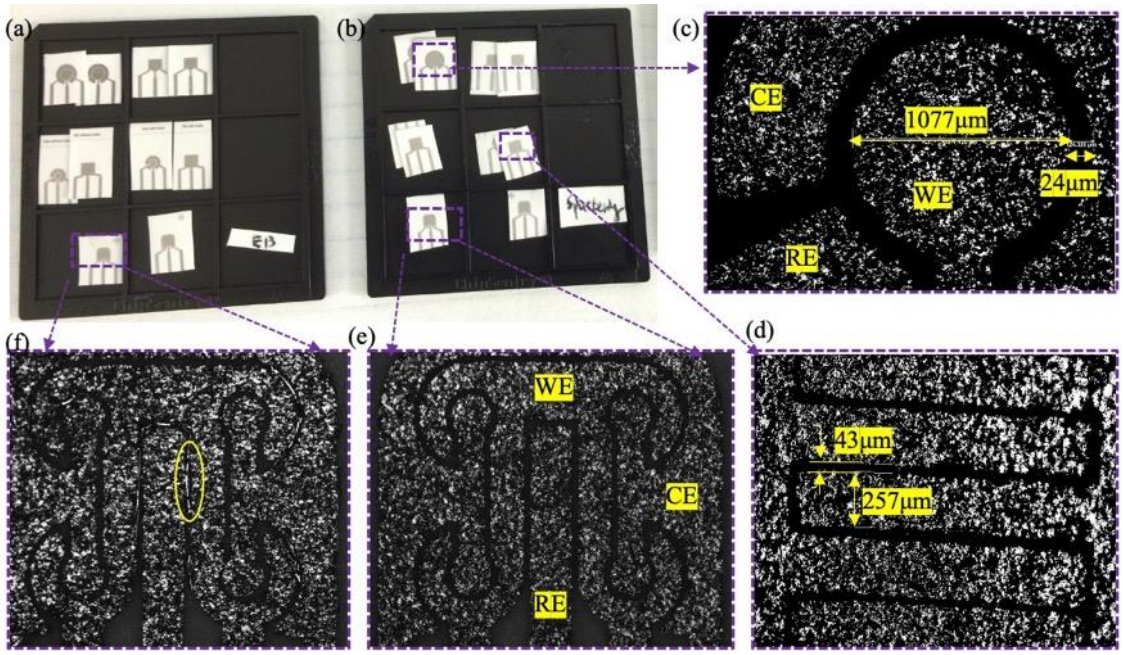

Figure 3.3. (a) Microfabricated Platinum electrode utilizing EB-evaporation; (b) Microfabricated Platinum electrode utilizing magnetron sputtering; (c) disk-shape electrode with porous design; (d) IDE electrode with porous design; (e) interdigitated disk electrode; (f) failed electrode due to lift-off issue.

The fabricated electrodes were then investigated with more precise tools, including atomic force microscope (AFM), scanning electron microscope (SEM), and focused ion beam microscope (FIB), to better characterizing the surface morphology and understanding how the porous substrate affect the microfabrication. Figure 3.4(a) shows a photograph of a fabricated MPRE gas sensor after mounting on the PCB but before RTIL deposition. The overall size of the reported MPRE sensor is about 7 × 8 mm^2, but the sensor geometry can be tailored to different shapes and sizes to suit application needs. The optical microscope view in Fig. 3.4(b) defines the structure of the three electrodes of the reported MPRE sensor; the diameter of WE is about 1050 μm, and the width of CE and RE is about 550 μm. The gap between WE and CE is about 130 μm with a gap of 140 μm between RE and CE. As shown in Figure 3.4(c), the surface morphology of the porous PTFE substrate was measured by AFM, reporting a root mean square (RMS) roughness of ~209 nm. Fig. 3.4(d) shows a close-up scanning electron microscope (SEM) image of the platinum electrode topography. Due to the porosity of the

PTFE substrate, the electrode surface can also be observed to be the rough and porous, which will effectively enhance the sensing area. Fig. 4(e) provides a side view of a rough spot on the electrode using focused ion beam (FIB). The silver and black areas represent the PTFE substrate, and the grey area indicates the electrode surface. The continuous junction area with uniform color between the substrate and the electrode indicates good adhesion between the substrate and the electrode despite of the rough substrate surface.

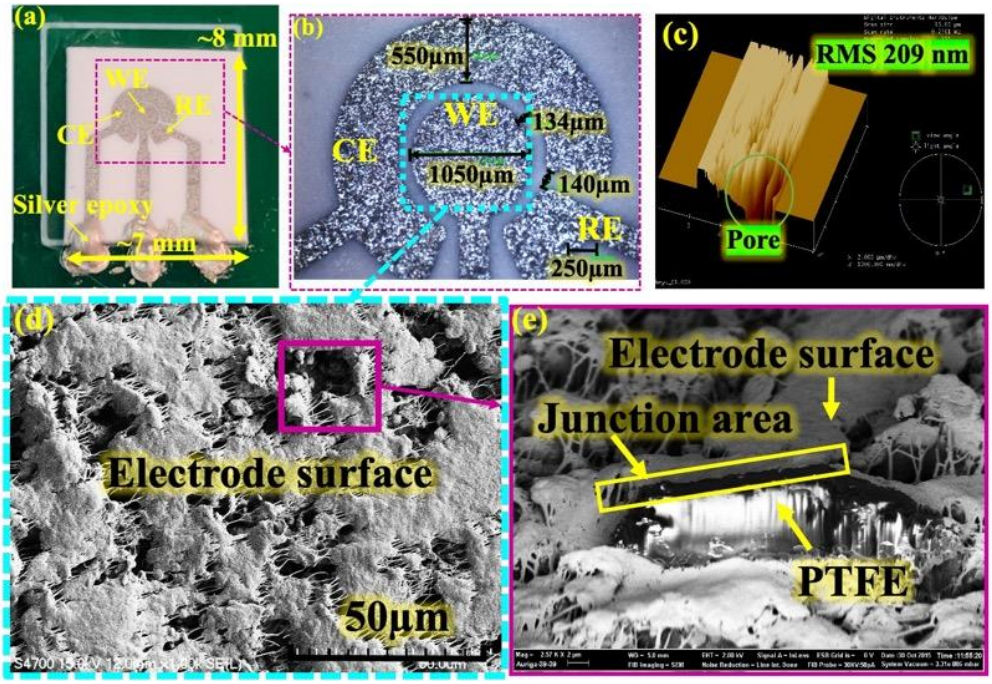

Figure 3.4. (a) MPRE gas sensor array under package; (b) MPRE gas sensor array integrated with electronics; (c) MPRE gas sensor electrode.

For sensor system assembling, as shown in Figure 3.5(a), the fabricated MPRE sensor was firstly attached to a custom PCB board and a 3D printed gas chamber. Gas sensor electrodes were connected to PCB traces using conductive silver for connection to external epoxy instrumentation. A hole was drilled through the PCB beneath the active sensing area, allowing gas to enter the device through the attached low-volume gas chamber. Connecting the MPRE sensor array with our developed sensor drive/readout circuitry, signal processing model, as well as the signal networking part, an integrated RTIL gas sensing system is shown in Figure 3.5 (b). After packaging shown in Figure 3.5 (c), the system can be wearable/portable to solve

spatiotemporal challenge of air pollutants monitoring.

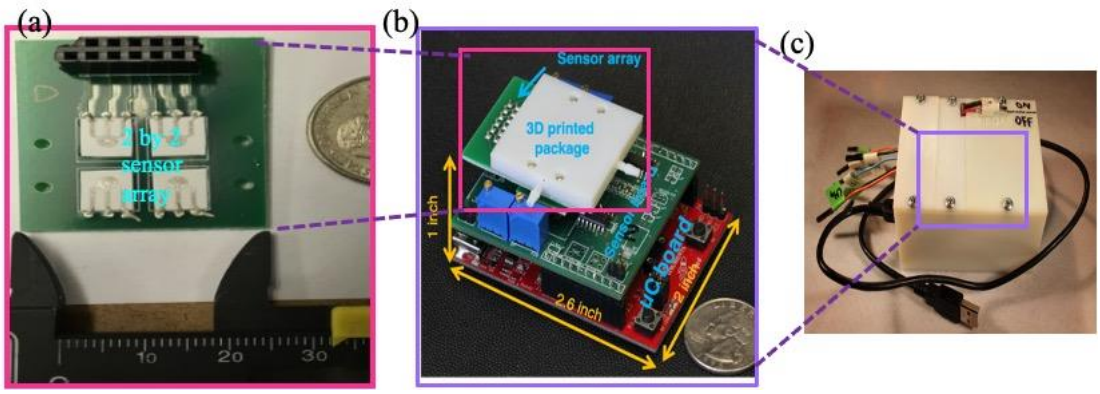

Figure 3.5. (a) 2 by 2 MPRE gas sensor array after interconnection; (b) RTIL gas sensing system that integrated sensor array, circuitry, signal processing and signal networking together; (c) Portable/wearable RTIL gas sensor package.

3.4 Electrochemical Test for Gaseous Airborne Pollutants

Multiple electrochemical methods, such as impedance, cyclic voltammetry, amperometry, and coulometric methods, have been applied with RTIL based electrochemical gas sensor, including both homemade bulky sensor and our microfabricated MPRE gas sensor. Prior work with RTIL gas sensors has demonstrated two important performance challenges that need to be overcome: 1) long measurement time; 2) drift induced by the reaction by-product accumulation. In this section, a new electrochemical approach, transient double potential amperometry (DPA) method, will be studied to solve the issues, and measurement results of multiple toxic gas utilizing our microfabricated MPRE gas sensor will be presented.

3.4.1 Experimental Setup

The packaged MPRE sensor was placed in a desiccator filled with calcium carbonate to minimize humidity because moisture is a known interferent in RTIL-based gas sensors that must be addressed using compensation or filtering techniques prior to real-world applications. A CHI 760 (CH Instrument, USA) was utilized for oxygen and methane tests, and a VersaSTAT MC potentiostat (Princeton Applied Research, USA) was used for sulfur dioxide and ozone

tests. A Gas Blender 103 (MCQ Instrument, Italy) and digital mass flow controllers (MFC, MKS Instruments Inc) were used for automatic gas mixing and flow control. The total gas flow rate in all tests was set to 200 standard cubic centimeters per minute (sccm) unless stated otherwise. N_2 was used as the background gas to mix with other gases in order to achieve air samples with different concentrations. All gases were purchased from Airgas Inc and used without further purification. Dry compressed air was used as the oxygen source, which contains ~ 21% oxygen.

3.4.2 Rapid Test Approach to Overcome the Long Response and Drift Challenge

Prior work with RTIL gas sensors has demonstrated two important performance challenges. The first is long measurement time, generally on the order of 100 s of seconds, using traditional electrochemical methods that must ensure a stable current response after sufficient decay of the charging current and, consequently, impede real-time monitoring applications. The second is reaction by-product accumulation on the sensor surface leading to drift that ultimately limits the operation lifetime of the sensor. Because by-product generation occurs during sensor measurement, it is exacerbated by long measurement times [126]. Making measurements quickly while reversing by-products to minimize the accumulation, a transient double potential amperometry (DPA) method was explored to resolve these challenges wherein double potentials for both oxygen reduction and superoxide radical (O^{2-}) oxidation are applied to reverse by-products and transient reaction currents are recorded without waiting for the charging currents to decay. When employed for fast oxygen measurement, transient DPA measurement is based on the reverse reaction of oxygen and superoxide as given by

$$O_2 + e^- \rightleftharpoons O_2^- \tag{3.1}$$

It is worth noting that the superoxide radical is not stable in a humid atmosphere where reaction with water would suppress the reverse reaction due to its high capability for reduction

as shown by [127]

$$2O_2^- + H_2O \rightarrow O_2 + HO_2^- + OH^- \quad (3.2)$$

Thus, the reaction of O_2/O_2^- must be verified in RTIL during oxygen measurement in air. The transient DPA technique that was employed is illustrated in Fig. 3.6. An oxidation potential (E_O) was first applied on WE for the oxidation period (T_O) to oxidize all reaction products. Subsequently, a reduction potential (E_R) was applied for the reduction period (T_R) to reduce oxygen. A typical response current from transient DPA during oxidation and reduction periods is shown in Fig. 3.6 (b). Notice the response current experiences fast decay at the beginning of the oxidation and reduction periods due to exponential decay of the charging current. At some relatively long time into each period, the current will stabilize after sufficient decaying of the charging current, as illustrated by the conventional amperometry reduction sample point tb. In contrast, transient DPA extracts a transient sample current at a much earlier time in the reduction period, rep- resented by ta, permitting measurements to be made much more quickly, and consequently limiting long-term by-product accumulation.

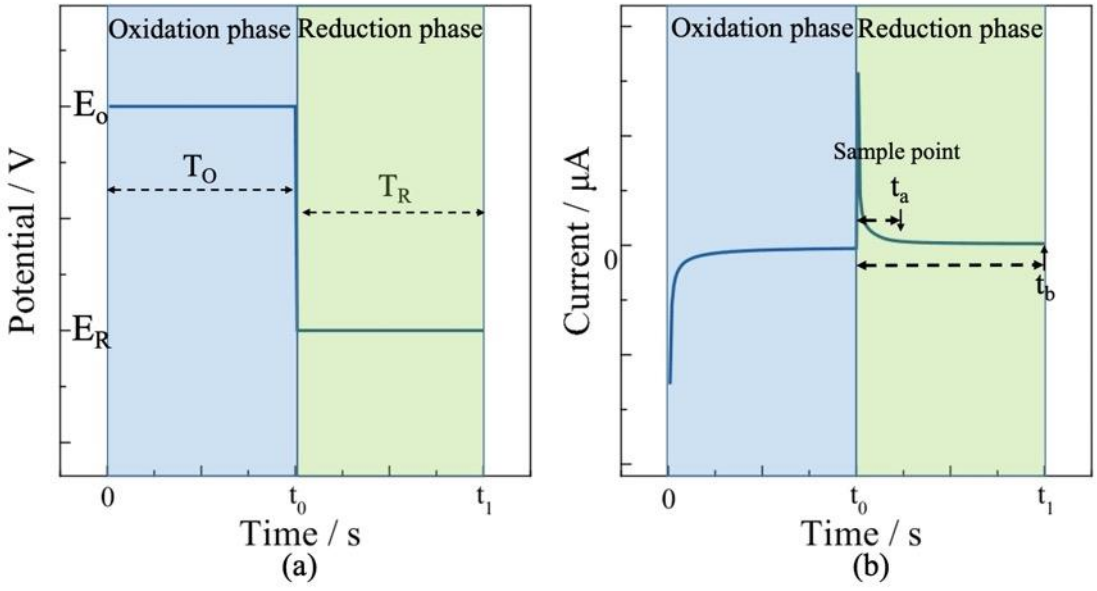

Figure 3.6. Principle and parameters of transient DPA for reversible reactions: (a) The potential

vs. time applied on WE; (b) typical WE current response vs. time. E_O, oxidation potential; E_R, reduction potential; T_O, oxidation period; T_R, reduction period; t_a and t_b, sample points in the reduction phase.

Experimental study with varied E_O, oxidation potential, reduction potential, oxidation period and reduction period; suggests that parameter combination when set E_R, as -1.2 V, E_O, as 0.2 V, T_R, as 2 s, T_O, as 2 s minimum measurement time and repeatability error. Utilizing the transient DPA method with the parameters, quantitative analysis of oxygen in air to validate the feasibility of the method for sensing applications. Compare to constant potential amperometry, in transient DPA method, an oxidation potential is applied to effectively re-oxidize by-products and decrease by-product accumulation on the surface of the WE. Since by-products accumulation may interfere with target gas diffusion and cause current drift during measurement, a comparison was made to evaluate the repeatability difference between constant potential amperometry and transient DPA. As shown in Fig. 3.7 (a), N_2 was first pumped into the gas chamber for 30 min to eliminate all possible interferants. Afterwards, alternating samples of N_2 and 50% compressed air were introduced for 5 min each in five sequential gas concentration cycles. A constant potential of −1.2 V was applied on the WE, and the current shown in Fig. 3.7 (b) was recorded with a 10 Hz sampling frequency. In a subsequent test with the same gas concentration cycles, transient DPA was applied at about 4 s before each N_2 purge. The recorded transient DPA reduction current vs. time is shown in Fig. 3.7 (c), while the inset plots the transient DPA reduction current vs. time overlapped for all five gas cycles. Transient DPA exhibits much higher current response mainly because it includes a charging current. From these experimental datasets, values were extracted at the end of each gas cycle for repeatability analysis. For constant potential, response currents of each gas concentration cycle were averaged during the last 2 s of each cycle. For transient DPA, the reduction current at t = 2 s was extracted. The repeatability observable in Fig. 3.7 (b) and the inset of Fig. 3.7(c) is compared in Fig. 3.7 (d). Over the five gas cycles, the RSD in constant potential amperometry

is 4.48% while the RSD in transient DPA is only 1.65%. The deviation of transient DPA is 63.2% less than that of constant potential amperometry, and the apparent downward drift in constant potential is conceivably due to by-products accumulation. In addition to better repeatability, transient DPA benefits from a greatly reduced measurement time compared to constant potential amperometry, which makes it more suitable for real-time monitoring of gaseous hazards.

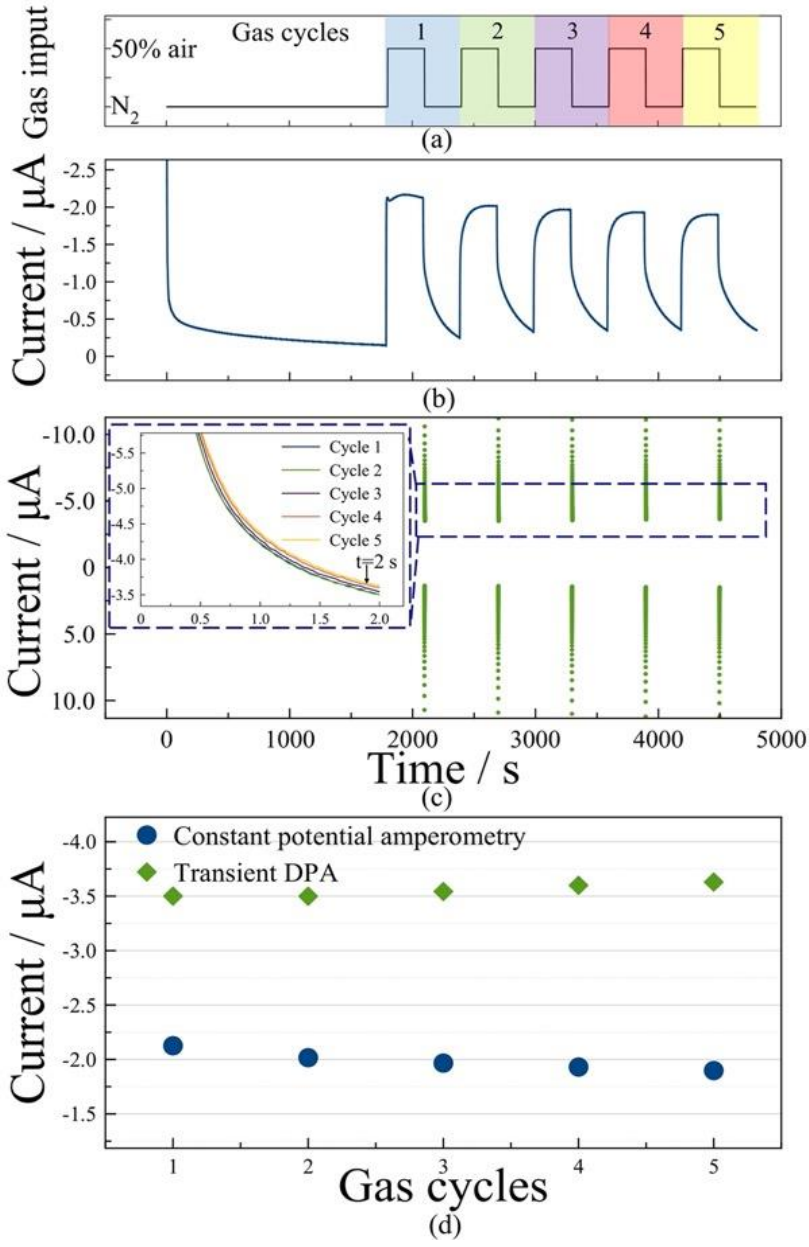

Figure 3.7. Performance comparison of constant potential amperometry and transient DPA for five cycles of alternating gas concentrations between N2 and 50% air: (a) gas concentration

cycles vs. time; (b) constant potential amperometry current response vs. time; (c) transient DPA current response vs. time; (d) reduction current comparison using constant potential amperometry (circle) and transient DPA (square). The inset in (c) shows the transient DPA reduction current plots overlapped for five gas cycles.

3.4.3 Electrochemical Test for Multiple Gas Pollutants

3.4.3.1 Oxygen-methane Coupling Test

With the fabricated MPRE gas sensor array, the potentials for oxygen reduction and methane reduction were set as −1.2 V and 0.9 V, respectively. The period for reduction and oxidation were set to 10 s each. By adjusting flow rates of 100% air and 10% methane, six samples of different methane concentration were tested, and each concentration was tested five times using double potential chronoamperometry. Each gas sample was continuously pumped for 30 min before measurement to maintain a stable gas environment. Recorded current at 10 s (end point of reduction phase) and 20 s (end point of oxidation phase), shown in insets of Fig. 3.8 (a), were extracted for further sensor calibration. The calibration curve in Fig. 3.8 (b) shows that the MPRE sensor reduction-phase current magnitudes exhibit a positive linear relationship to oxy- gen concentration, with a sensitivity of 0.22 μA/[% oxygen] and a linearity of 0.96 for oxygen sensing, presenting a resolution of 0.60% oxygen in oxygen-methane coupling test. The calibration curve in Fig. 3.8 (c) shows that the MPRE sensor oxidation-phase currents exhibit a positive linear relationship to methane concentration, up to at least 6% methane, with a sensitivity of 0.31 μA / [% methane]. As shown in red zone in Figure 3.8 (c), somewhere between 6% and 8% methane, the current amplitude was observed to start decreasing with higher methane concentrations. This phenomenon is believed to be attributed to the incomplete oxidation of methane at high concentrations. Excess methane could lower the current response due to insufficient sup- ply of oxygen for oxidation, which limit the methane detection range of the MPRE sensor.

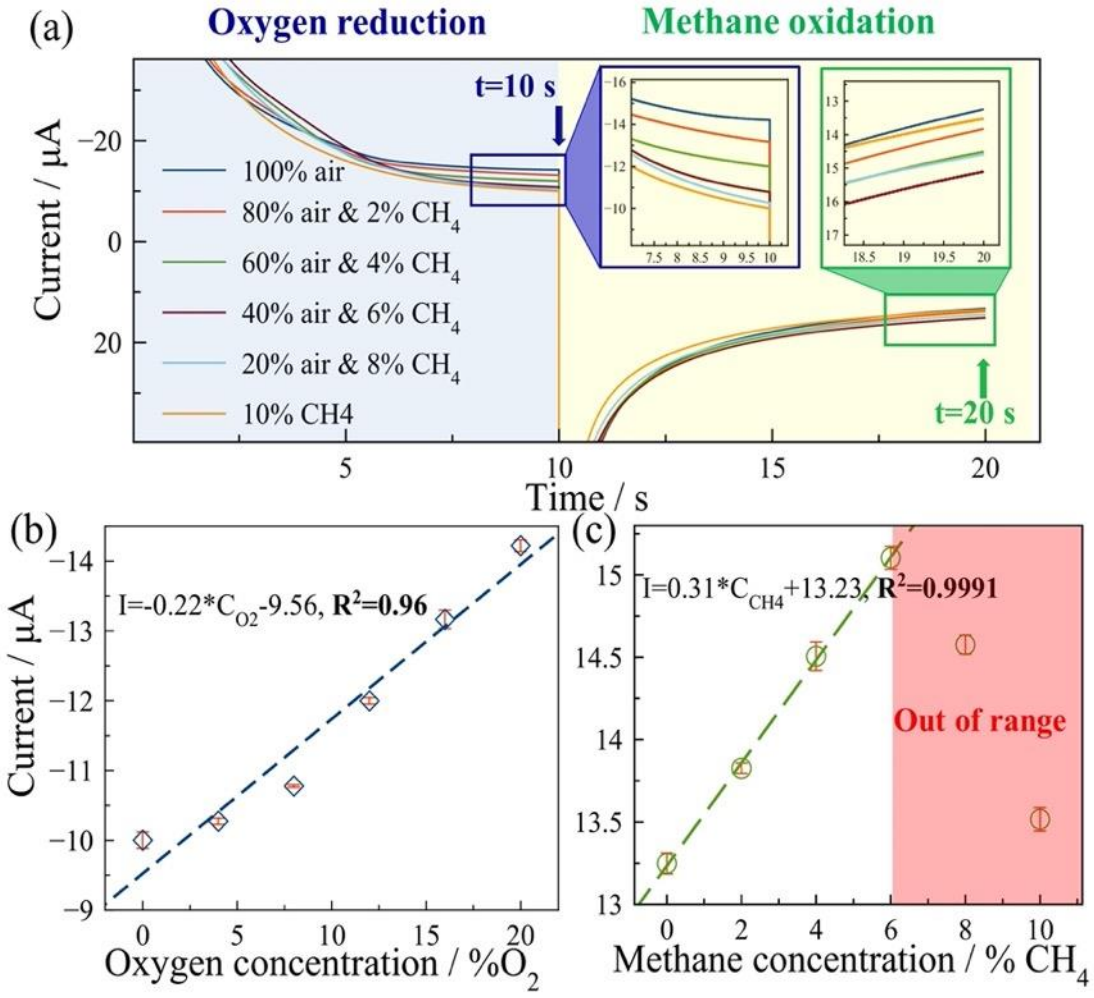

Figure 3.8. The methane-oxygen coupling test: (a) The current response of the MPRE sensor in the coupling tests: oxygen reduction (-1.2 V), methane oxidation (0.9 V); (b) Oxygen measurement calibration; (c) Methane measurement calibration, in which red zone indicates methane out of range.

3.4.3.2 Sulfur Dioxide Sensing

For sulfur dioxide sensing, negative potential of −1.5 V was applied for 10 s to measure sulfur dioxide reduction current. Six samples with concentrations varying from 0 ppm (part per million in volume) to 2500 ppm were tested by setting the flow rate of nitrogen to 100 sccm and varying the flow rate of a 5000 ppm SO_2 source from 0 sccm to 100 sccm with 20 sccm increments. The reduction current for different SO_2 concentration measurement is shown in Fig. 3.9 (a). Reduction current at both 3 s and 10 s were extracted for calibration and are plotted in Fig. 3.9 (b). The sensitivity of the MPRE sensor for SO2 measurement is 0.13 μA/100 ppm

and 0.18 μA/100 ppm at 3 s and 10 s with a linearity of 0.92 and 0.97, respectively, suggesting that longer reduction time could enhance the sensitivity. As shown in Figure 3.9 (c), a resolution of 209 ppm for SO_2 sensing was achieved with the MPRE sensor.

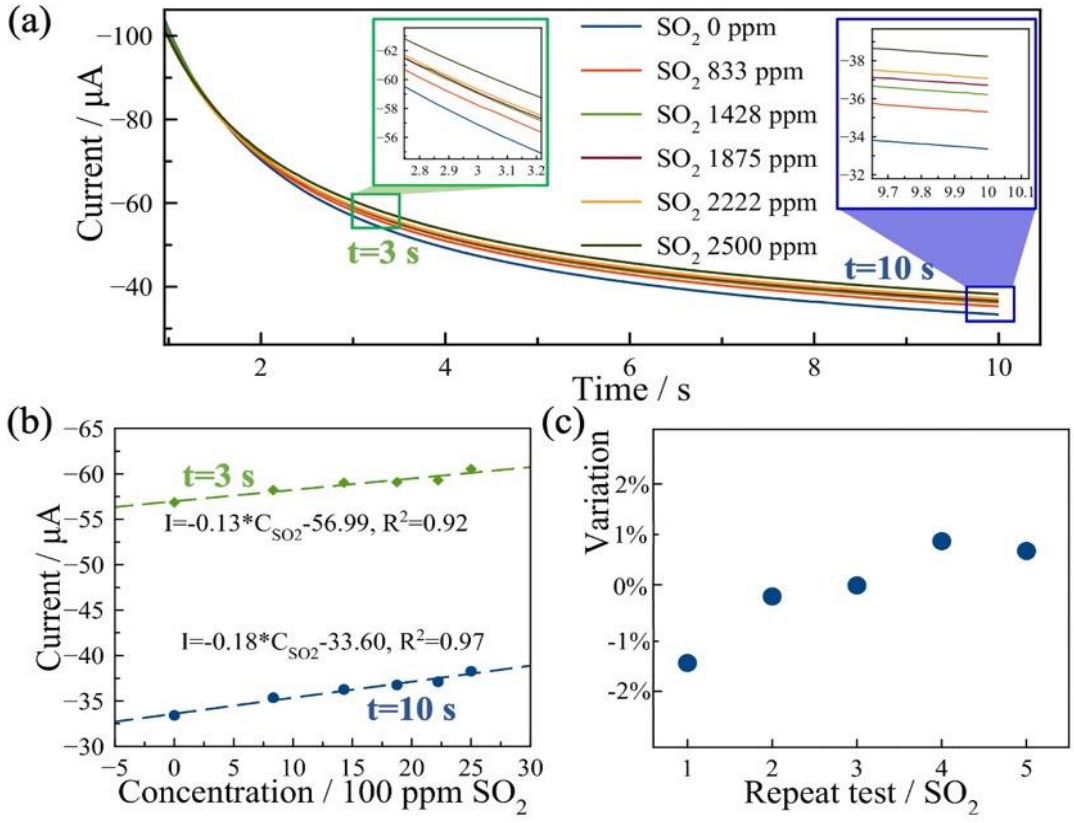

Figure 3.9. Sulfur dioxide measurement: (a) SO_2 reduction current; (b) The calibration of the sensor using currents at 3 s (green) and 10 s (blue); (c) The relative variation of five repeat tests using currents at 10 s in 2222 ppm SO_2.

3.4.3.3 Ozone Sensing

After conditioning at 0 V for 10 min, −0.8 V was applied to the sensor for 10 s for ozone reduction. Six different gas samples were tested with concentration increasing from 0 ppm to 1000 ppm in 200 ppm increments. As shown in Fig. 3.10 (a), typical decaying current responses were obtained with current amplitude increasing with O3 concentrations. Currents at 3 s and 10 s were extracted and are plotted in Fig. 3.10 (b). For ozone measurement, the sensor exhibited a sensitivity of 0.11 μA/100 ppm and 0.064 μA/100 ppm with linearity of 0.916 and

0.921 at 3 s and 10 s, respectively. The sensitivity decreases with longer reduction time, while the linearity increases slightly. Five repetitive tests were conducted for 800 ppm O_3 as shown in Fig. 3.10 (c), and the MPRE sensor presents a resolution of 92 ppm in ozone sensing based on the largest variation. The RSD in the tests is 1.85%, exhibiting good repeatability of the MPRE sensor for O_3 measurement.

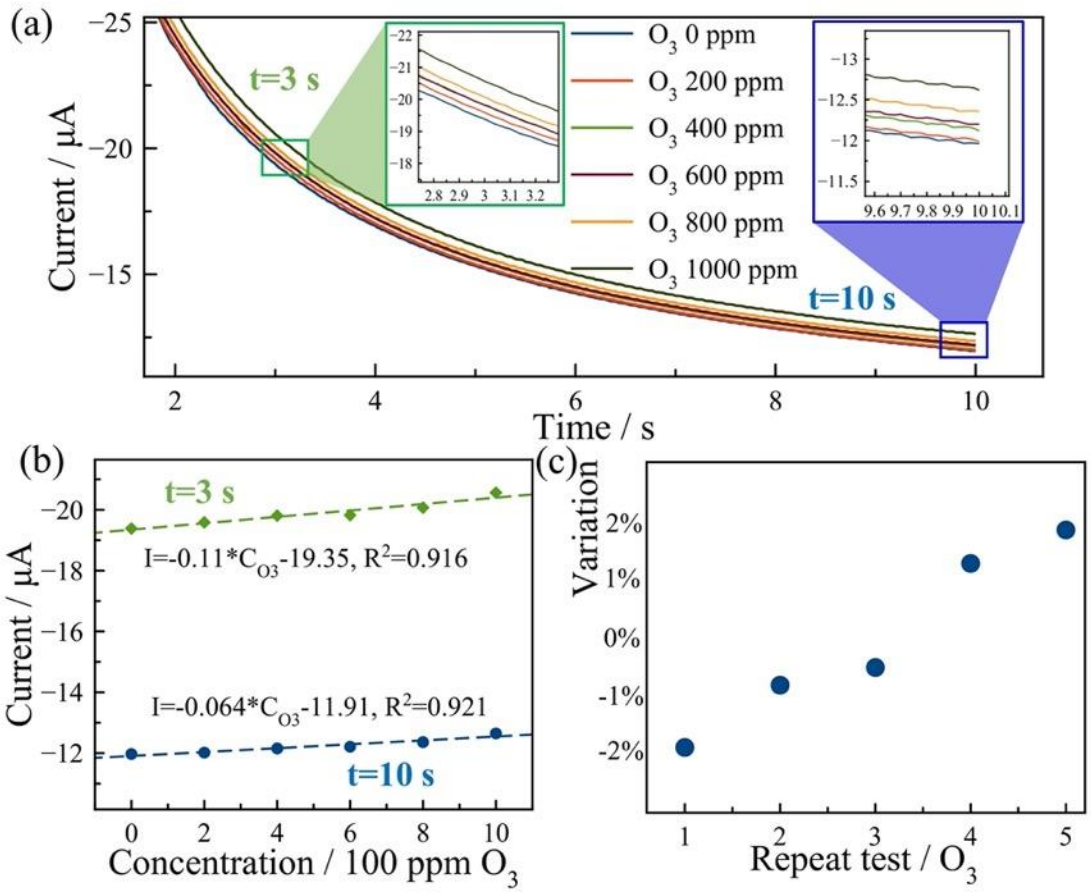

Figure 3.10. Ozone measurement: (a) The current response of the MPRE sensor in O_3 measurement. (b) The calibration of the sensor using currents at 5 s (green) and 10 s (blue); (c) The relative variation of five repeat tests in 800 ppm O_3.

3.5 Conclusion

Utilizing RTIL as the electrolyte, following the new microfabrication procedure and electrochemical approaches, the MPRE gas sensor have been successfully used to record the sensing of multiple gaseous air pollutants, including oxygen-methane, sulfur dioxide and ozone, with high sensitivity and good repeatability. Sensor Selectivity can be achieved by judicious

choice of electrode materials, RTIL chemical composition and electrochemical method (particularly bias voltage) with data processing algorithms that have been widely applied in electronic nose systems. Furthermore, a high sensitivity multi-channel CMOS circuit has already been developed in our group for air quality monitoring based on an RTIL-based gas sensor array [128]. Thus, the MPRE gas sensor, together with the CMOS circuit provides a very promising platform toward a miniaturized, inexpensive, rapid-response, low power, multi-gas sensing array for point-of-exposure monitoring of gaseous hazards with the capability to solve the spatiotemporal challenge.

4 Microfluidic Platform for Continuous Personal PM Monitoring

In addition to gaseous elements, particulate matter (PM) plays a significant role in airborne pollutants. PM contains species with a range of solubilities (from insoluble soot to hygroscopic salts) and complex morphologies, all of which vary temporally, spatially, and with PM size due to constantly changing emissions and atmospheric reactions [129]. For this reason, PM is also a challenge to accurately collect and quantify at the personal exposure level and thus a challenge to study from a toxicological perspective. As reviewed in Chapter 2, existing non-FRM and non-FEM methods require long time integration periods (~1 day) and large, immobile, expensive, and specialized equipment. In addition, because of the significant challenges posed by personal PM monitoring, including the large degree of spatial and temporal dynamics and need for size-fractionated elemental component analysis, existing portable exposure monitors are ineffective for real-time assessment of multi-pollutant exposures as well. The Health Effects Institute recently reported that a lack of high quality PM measurements across size and components make it very difficult to definitively determine PM impacts on human health, stating "more advanced approaches…will be needed so that exposure at the individual or population level can be assessed more accurately" [130]. To achieve more effective regulation and health interventions, additional data across PM size-fractions and elemental components are required, and novel approaches are needed to facilitate personal exposure monitoring over short time scales.

In this chapter, the existing technology options for a real-time continuous PM monitoring system are reviewed, and an autonomous microfluidic PM monitoring platform is introduced. The new PM monitoring platform was designed to greatly enhance environmental health research, enable development of accurate health impact models and personalized exposure management strategies, and informed pollution regulation.

4.1 Requirements Analysis and Design Approach

As reported by the EPA published national ambient air quality standard, particulate counts in PM samples typically are small (~ 1.56-3.59×10^7/m^3 for unhealthy PM level with an AQI of 151-200). So, a PM capture section that pre-concentrate the particulates just like that as done by filters in stationary systems is essential part to improve the particle counting efficiency. Analysis of liquid aggregates is by far the most common analysis form. However, in nature, PM is airborne, suspended within a gaseous environment. As analyzed in following section, to process PM utilizing the microfluidics technology and electrochemical classification (specify and determine the PM components) technology with their satisfactory separation performances, it is necessary to capture PM from air into a liquid sample. The PM capture not only act as a pre-concentrator but also introduce the PM from gaseous environment into microfluidic environmental, could perfectly guarantee the usage of microfluidic separation and electrochemical detection for PM monitoring.

A key and currently not well understood factor in the toxicity of airborne particulates is its size fractionation across fine spatial and temporal resolutions relative to personal exposures. At a most basic level, the size or aerodynamic diameter of PM determines its penetration into the human respiratory system and its subsequent related impacts on health. Thus, the ability to assess PM across size fractions is of paramount importance. Moreover, we have found that size fractionation prior to quantification (measure the PM concentration by weight/volume or count particle number/volume) and classification (specify and determine the PM components) allows us to consider new measurement modes that are well suited to application goals (real-time, continuous, etc.) and only viable when particles being analyzed are within a known size range. For example, both the capacitive quantification and electrochemical quantification, which will be analyzed in following sections, rely on knowing PM size. Most existing PM monitoring instruments rely on physical filters to aggregate particles of specific size over time and are thus

not suitable for real-time, continuous measurement. In contrast, microfluidics provides a low-cost alternative for continuous size fractionation that has been well demonstrated in biological application (e.g., cell sorting) for elements of similar diameter to PM.

After performing size fractionation, a real-time continuous quantification section with single particle resolution that enable high spatiotemporal resolution in a miniaturized format, together with a PM elemental component analysis section that help to collect information about the elemental components associated with health impacts should also be designed to perform PM quantification and classification. The PM quantification and component classification data across multiple size will lead to more relevant air pollutant regulation, intervention for individual's most susceptible to exposure, and ultimately improvement of overall public health.

Microfluidic technologies, a multidisciplinary technology that deal with precise control and manipulation of fluids that are geometrically constrained to micro or even smaller size, have been widely studied for decades that cover almost all aspects of fluid related life sciences [131], [132]. The boosting developments of microfluidic devices and systems, such as microfilters, microseparators, microchannel integrated sensors and so on, provide a unique and beneficial combination of PM preconcentration and size-fractionated particle counting and component analysis to develop an easily used, wearable, real-time continuous PM monitoring system with high spatiotemporal resolution.

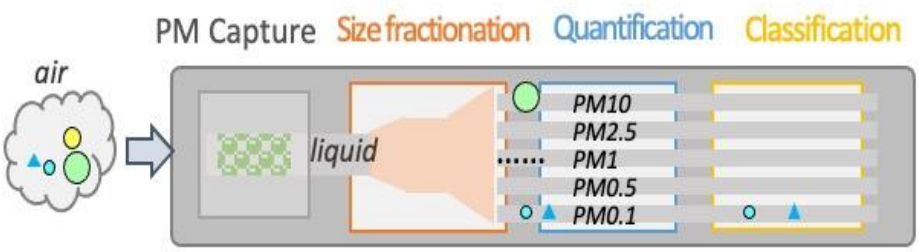

Figure 4.1 Architecture for continuous PM monitoring for personal exposure management featuring capture, size-fractionation, quantification, and elemental classification components.

Based on the analysis above, to solve the challenge of real-time continuous personal exposure assessment, we developed a microfluidic PM monitoring system consisting of the four components shown in Fig. 4.1: capture, size fractionation, quantification and classification. The PM capture will not only pre-concentrate the PM samples but also help to perform sample to liquid interfacing. The size fractionation section before detection allow more design margin for PM quantification and classification. Utilizing novel microfluidic particle separation, combined with on-chip PM quantification and classification could potentially present a unique opportunity for expected features of 1) real-time continuous monitoring (to enable high temporal resolution); 2) online size-fractionated PM mass and elemental composition analysis (to enable rich exposure datasets); and 3) autonomous, wearable, low-cost, low-maintenance implementation (to enable wide distribution to a network of individual users permitting high spatial resolution).

4.2 Technology Options for Continuous PM Monitoring

As reported, monitoring tools capable of personal, continuous, real-time PM monitoring assessment is lacking. However, if inspecting individual parts of the proposed PM monitoring system, as shown in Fig. 4.1, there are published research that can be suitable technology options. In this section, suitable particle capture, microfluidic size fractionation, on-chip quantitative particle detection and on-chip particle classification following with compact system integration technology are reviewed and compared to help designing the proposed wearable, real-time, continuous PM monitoring system.

4.2.1 Methods for Particle Capture

Before the PM size fractionation, quantitative PM detection and PM components classification, a suitable aerosol sampling method which work like a filter or particle sedimentation device to collect PM particles is necessary [67][133]. A modified virtual

impactor have been utilized to work as a large particle trap [134]. In this design, large particle which have large initial force will be trapped in the particle trapping region. As analyzed, following microfluidic size fractionation and electrochemical classification rely on the particles stay in liquid phase, but this modified virtual impactor still work on air phase. Alternatively, as shown in Fig. 4.2, another two particle trapping methods, including the purely air-liquid phase interfacing and the corona charge platform integrated with MEMS air-liquid interface, can help to trapped targeted PM particles into the fluid [135], [136]–[139]. As shown in Fig. 4.2 (a), in the air-liquid trap, a periodic array of anchored liquid-bridges worked as a stationary particle trap, when air pass by the microchannel, particles can be trapped along the air-fluidic path during the air-liquid interfacing. However, the schematic of how particle will be trapped, what trapped efficiency can be achieved utilizing this design is still unknown. In addition, after particle trapping with anchored liquid array, how to direct liquid array toward the following size fractionation channel is still a challenge. As shown in Fig. 4.2 (b), the alternative particle trapping topology which also can introduce the PM particles into liquid phase is the corona discharge based electrostatic precipitators (ESPs) integrated with a microfabricated perforated Si diaphragm which served as the air-microfluidic interface. In this method, an ESP that consists of a discharge and a collection electrode with voltage bias between them to create very strong electric filed, aerosol particles direct by the pump acquire positive charges in a positive corona or negative charges in a negative corona through either active field charging or diffusion charging. While pure air could be avoided, the charged aerosol particles will be tracing by the drag and electric force to reach the air-microfluidic interface and be directed into the liquid phase to go through following size fraction process. This point-of-care electrostatic precipitators (PoCESP) integrated with microfabricated air-microfluidic interface is more complicated, but perfectly solve the aerosol sampling process [137][140].

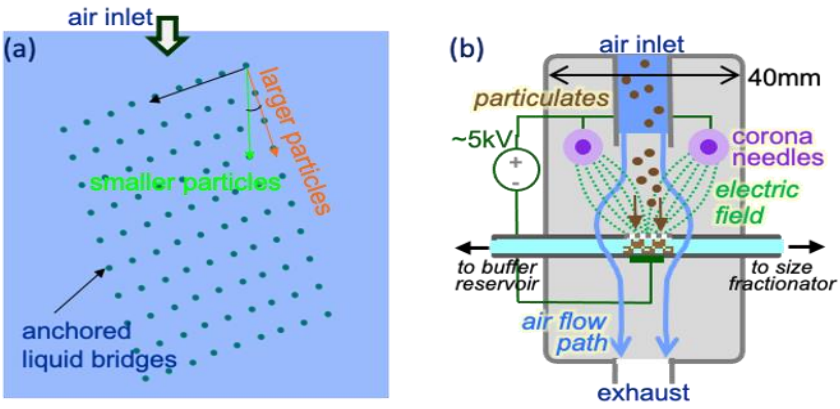

Figure 4.2. Particle traps: (a) anchored liquid array based stationary deterministic lateral displacement (DLD) phase for particle separation and trapping system; (b) electrostatic precipitators (PoCESP) integrated with microfabricated perforated Si diaphragm which served as the air-microfluidic interface work as PM trap.

Although perfectly fit with the subsequent microfluidic size-fractionation and component analysis, either the anchored liquid array trap or the perforated diaphragm air-liquid interface suffers from low trap efficiency, which to some extent will rise up the power consumption by extra sampling runs. In contrast, utilizing the inertial air-liquid interface, a curved microchannel was reported to achieve ~98% particle collection efficiency at a particle diameter of 1 μm [141], [142]. The concept of curved microchannel utilizing inertial air-liquid interface to trap aerosol sample into liquid is shown in Fig 4.3. The fluid flows inside the microchannel are Dean flows, composing of two symmetric vortices at the top and bottom of the channel. The pressure gradient of the air flow between the center and wall of the channel leads to the Dean flow which influences the particle movement along the curved channel. Due to the inertial of the particles, the two-phase fluid, sampling air and collecting liquid, forms a stratified flow in the curved microchannel and particles are transferred from air into the liquid phase by particle centrifugal and drag forces. Although the inertial air-liquid interface has excellent particle collection efficiency, the method is limited for particles that are smaller than 600nm due to the extremely small inertial.

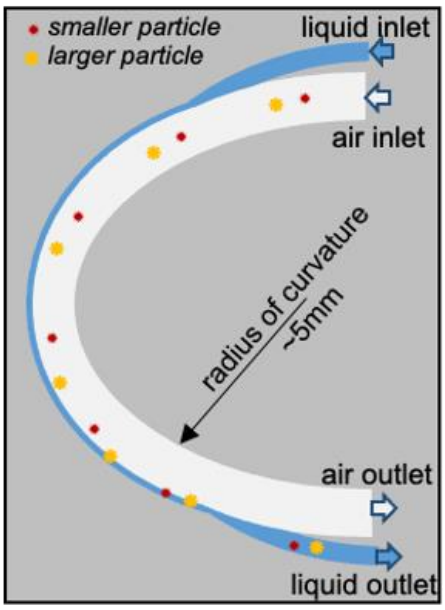

Figure 4.3. Concept of a curved microchannel utilizing inertial air-liquid interface to trap aerosol sample into liquid.

4.2.2 Methods for Continuous Size Fractionation

Among the methods for sampling air listed by NIOSH, the sampling device can include all kinds of filters, impactors, cyclones, impingers, wetted-surface bioaerosol samplers, condensation-based bioaerosol samplers, electrostatic samplers, passive bioaerosol samplers and so on [67]. Some of these sampling methods utilize microfluidic technology in a miniaturized format, can be considered as technique options for the microfluidic PM size fractionation. Existing microfluidic, separation methods can be categorized as either active or passive. Active microfluidic separation technology typically need to incorporate an external force, such as dielectrophoresis, electrophoresis, acoustophoresis, immuomagnetic force and optical force, which is too complicated to be integrated within the compact system [143]. In contrast, passive methods only rely on the specifically designed microchannel structure and internal forces. Passive methods including impactor, cyclone separator and deterministic lateral displacement (DLD) separation, are perfect option for the PM size fractionation. Since cyclone separator typically have quite large volume, which is not suitable for system miniaturization, here only impactor (including virtual impactor) and DLD separator will be reviewed.

4.2.2.1 Inertial microfluidics

The inertia of particles, overcomes the viscous drag force linked with their mass (size), will drive the particles onto an impaction plate to affect their flow path and thus separate the particles based on size. Most widely used inertia approach includes cyclone, inertial impactor (Fig. 4.4 (a)), and virtual impactor (VI, Fig. 4.4 (b)). Typically induced by thermophoresis or electrostatic forces, based on Navier-Strokes theory and set desired 50% cut-off diameter for the impactor, particles smaller than cut-off diameter will transmitted through the impactor following the major flow while large particles will be avoided and direct to minor flow, as shown in Fig. 4.4. The penetration efficiency curve of impactors determines the separation efficiency of desired particles. As known, inertial impactors typically have better penetration efficiency, however, inertial impactors typically suffer from particle build up issue. Differ from inertial impactor, vertical impactors expelled large particles from the major flow and divert them around a tight corner following the minor flow. Compare to inertial impactor, vertical impactor typically has worse penetration efficiency performance which in return resulting low separation efficiency. Several group have tried to study how particles performance in the air-phase-based microfluidic channel, which potentially can help to optimize the vertical impactor performance [144]–[146].

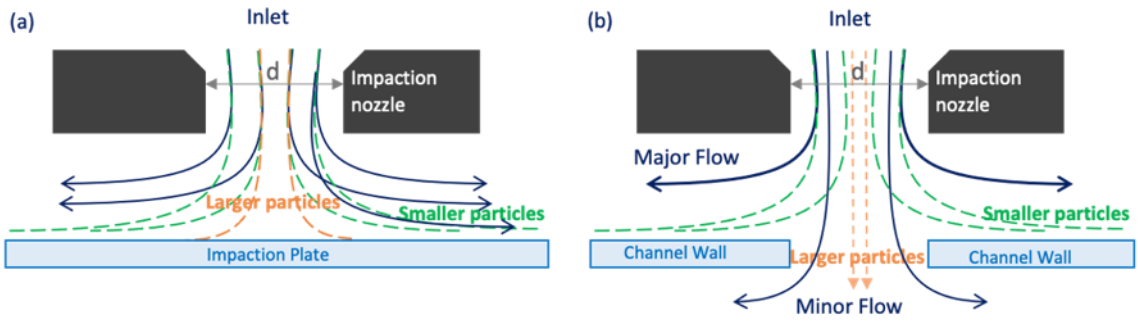

Figure 4.4. Inertial impactor (a) and virtual impactor (b).

Due to the nozzle design, when targeting UFP with inherently small sizes which in return require small nozzle size, the small nozzle will lead to great challenges for high-throughput

size fractionation. In order to improve the throughput, a reverse wavy channel structure using viscoelastic fluids with the addition of biocompatible polymer was presented to sort submicron particles [147]. The sorting device was consisting of periodically repeated wavy channel structures. By periodically reverse the crimp direction, the Dean secondary flow, generated by the wavy channel, will periodically reversed to facilitate particle focusing compared with traditional straight channels. Testing with exosomes and other particles contained biofluids, they have achieved high-throughput exosomes separation with purity higher than 92%. This wavy channel design was reported to be able to sort 30nm sized particle, however, the requirement of the viscoelastic fluid for the creation of the Dean secondary flow and the limited separation efficiency determine it fit the biological application.

4.2.2.2 Deterministic Lateral Displacement (DLD) Separation

Differ from impactors, an alternative for passive separation is the deterministic lateral displacement (DLD) method that utilizes asymmetric bifurcation of laminar flow around pillar arrays for particle separation [148], [149]. The more efficient hydrodynamic DLD microfluidic technology was first reported by Huang et al. to separate particles on the basis of size in continuous flow with a resolution of down to 10 nm as well as pretty high separation efficiency [150]. As shown in Fig4.5, DLD separator relies on the fact that, when particles flow through an array of pillars set at a gradient to laminar flow, those larger than a designed cut-off size (D_c) will be bumped off their flow path to follow the pillar gradient while smaller particles will follow laminar flow, enabling separation at downstream outlets after passing through 10s to 1000s of pillars. Because of the high efficiency advantage, DLD has been extensively studied, employed and modified by researchers in terms of theory, design, microfabrication and application to develop newer, faster and more efficient tools for separation of millimeter, micrometer and even sub-micrometer sized particles. A modified I-shape pillar which could induce a rotation in non-spherical particles that will in further enhance separation efficiency

has been reported [148]. Moreover, different novel pillar shape design, multi-size separator as well as the electrostatic force-modulated DLD system have also been reported to show 100% separation efficiency for three types of particles [149], [151]. Compare to impactors, the hydrodynamic DLD separation with its higher separation efficiency is better option for PM size fractionation.

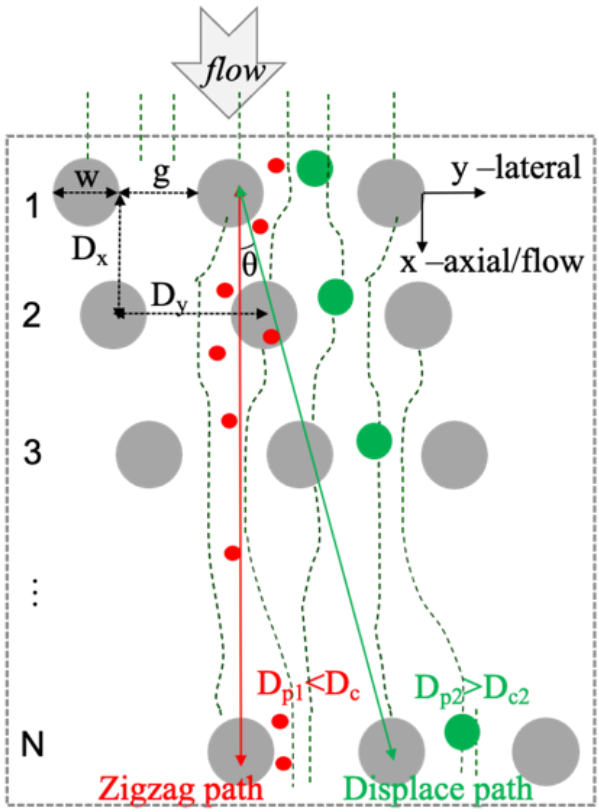

Figure 4.5. DLD separation theory: in the three fluid streams in the gap, large particles (D_{p2}) will be displacement along the flow path, small particle (D_{p1}) keep its initial streamline path.

4.2.3 Methods for Continuous Quantification

A real-time continuous quantification microsystem that enables high spatiotemporal resolution in a miniaturized format is the key element for a PM monitor. Facilitating the miniaturization technology, an on-chip continuous PM quantification system, avoiding accumulation of PM that adopted by most methods, will greatly simplify the usage with improving the spatiotemporal resolution. As analyzed in section 2.4.4, compared to optical and

gravimetric PM detection, electrochemical detection can offer accurate PM quantification as well as the potential for classification of chemical composition [152]–[154]. Meanwhile, the electrical, especially the capacitive quantification methods have advantages, such as the potential to measure UFP with its high sensitivity, the potential to be real-time and continuous, easier to be fulfilled by microfabricated on-chip quantification device, and easier to be miniaturized which in further reduce the difficulty of make the whole system wearable. In addition, take advantage of the powerful CMOS circuit readout circuits, on chip electrochemical or capacitive PM monitoring integrated with CMOS circuitry with the integration strategy promise the on-chip capacitive PM quantification a great option.

4.2.3.1 Electrochemical Quantification

Electrochemical method is widely known to offer detection, quantification, as well as the potential for classification of chemical composition of PM. Furthermore, recent literature shows that electrochemical readout can be performed in compact microelectronic chips [155], which permits highly integrated electrochemical readout for PM quantification. Because of high sensitivity, repeatability and selectivity, and their potential for compact size and low power consumption, electrochemical measurement methods are good candidates for portable/wearable systems. However, miniaturization of electrochemical sensor toward the goal of high spatiotemporal resolution is still lack of study. With consideration of integrating a miniaturized microfabricated PM sensor with compact electronics together, a new method for electrochemical quantification will be presented in Chapter 5.

4.2.3.2 On Chip Planar Capacitive Detector and Parallel Capacitive Detector

On-chip capacitively PM quantification can be simply categorized as planar capacitive detector and parallel capacitive method, the planar capacitive PM detector measure the particle concentration based on the accumulation of the capacitance change when particle settle down

on top of the electrode surface, while parallel capacitive PM detector measure the particle concentration based on the accumulation of the capacitance change when particle pass by the space between two electrode plates.

Several groups have developed the on-chip planar capacitive particle detection. A 2-D acoustic particle focusing enables sheathless chip Coulter counter with planar electrode configuration was developed to provide the path towards small flow cytometers to measure particles [156]. Another hybrid differential 3-stage and 5-stage ring oscillator based capacitance sensors were designed and integrated with CMOS circuitry resulting in attofarad sensitivity to achieve single particle detection [96]. In the meantime, a monolithic on-CMOS capacitive detection of micrometric airborne particulate matter was also developed [93]. The multi-channel lock-in architecture, as well as the 65 zetofarad resolution CMOS readout circuitry design, allow this structure to mapping of both indoor and outdoor PM in the 1-30 μm range. However, because of the capacitive detection rely on the settle down of the particles on top of the electrode plate surface, the planar capacitance configuration is not suitable for real-time continuous PM detection.

Another configuration for solid-state direct capacitive PM detector is the parallel-plate microelectrodes for in flow detection of PM. A plate bottom electrode with covered mesh top electrode structure was developed to measure nanoparticle in air [94], [95], [97]. By measuring the time dependent changes of electric capacitance under impact of water droplets containing airborne nanoparticles, which affect the dielectric of the capacitor, the capacitive-type counter could potentially be used to measure PM. However, this structure still relies on the particle deposition on top of the bottom electrode surface which hinder it evolve toward the real-time continuous PM monitoring purpose. Several groups have published mathematically analysis of the Coulter counter based parallel capacitive PM detection [157][158]. This mathematically

analysis enlighten us that building up parallel capacitive plate based on the vertical sidewall electrode along the microchannel that particle will pass by is the solution for real-time continuous PM monitoring.

4.2.3.3 Lab-on-CMOS Integration for High Resolution On-chip PM Quantification

As can be concluded from previous capacitive detection review, in order to reach single particulate particle counting, especially for UFP, a CMOS circuitry that can help to reach attofarad or even zetofarad resolution is necessary. However, when measure submicron particles or even UFPs and the capacitive change due to particle pass by may reach zetofarad sensitivity, the noise issue would be a great challenge. Moreover, for high throughput capacitive electrodes array design, the wiring and noise issue could be more significant even with the CMOS designed high resolution readout circuitry design. Our group recently introduced the "lab-on-CMOS" concept that realize multichannel lab-on-chip functions utilizing microfluidics with sensing on the surface of a CMOS chip [159], [160]. To meet this challenge, the lab-on-CMOS integration technology, defined as system that provide miniaturized monolithic direct on CMOS capacitive electrode structure which help to hander both noise and high throughput challenges [161][162]. Under the umbrella of point-of-care for both healthcare related biosensors and environmental related environmental monitors, lab-on-chip and lab-on-CMOS technology have been thoroughly studied. Lab-on-CMOS integration technology typically can be categorized as system package without extending substrate, such as packaging rely on wire-bonding, and system package with extending substrate which including flip-chip method and so-called chip-in-carrier method.

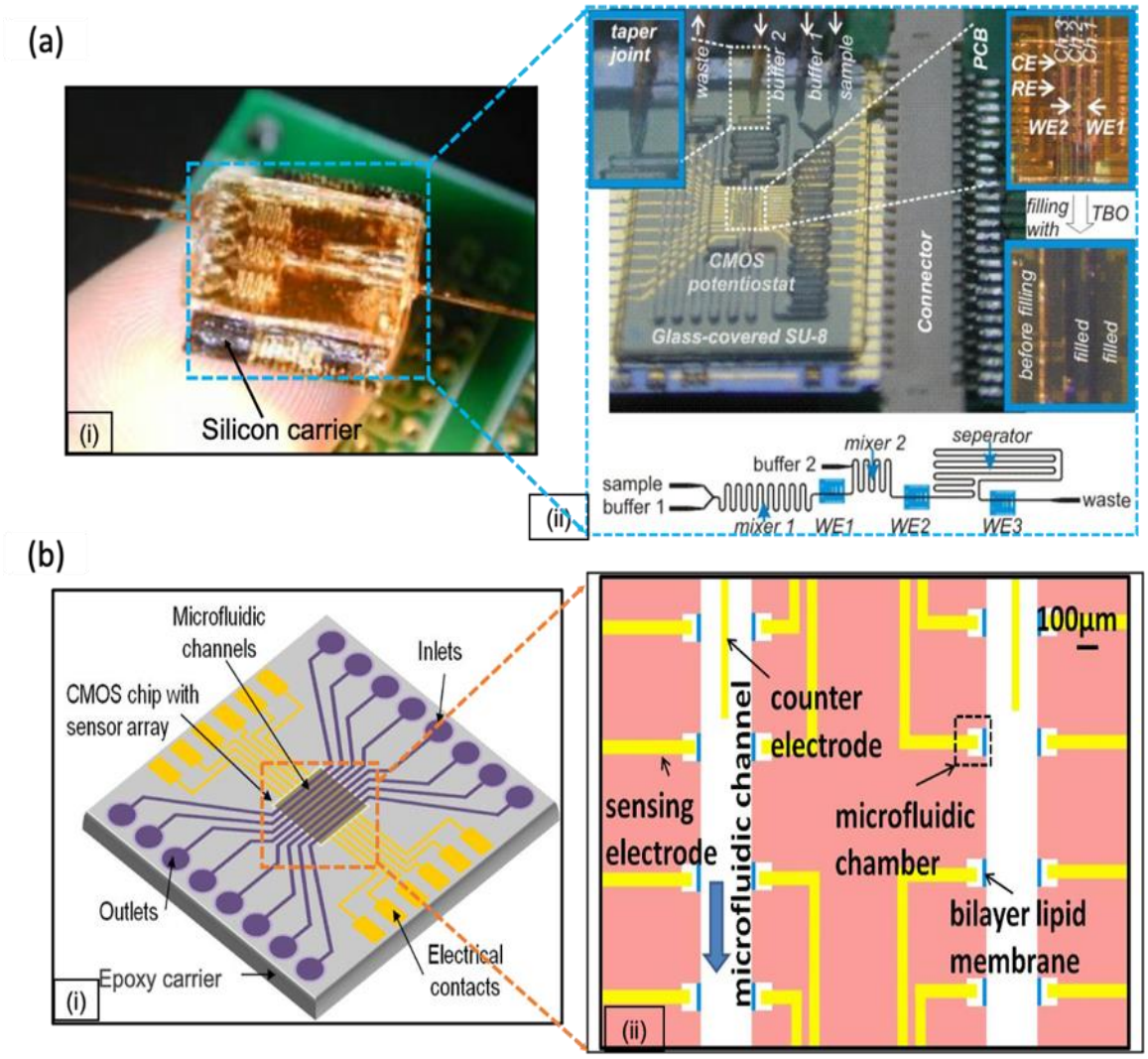

Figure 4.6. The chip-in-carrier lab-on-CMOS package: (a) chip-in-carrier package while silicon wafer as the carrier; (b) chip-in-carrier package while epoxy as the carrier.

Without extending the substrate, there were several group work on combining post-CMOS electrode fabrication, protecting the CMOS chip with polymer material and connect the readout through wire bonding [163], [164], [165], [166], [167][168]. This topology allows on-CMOS electrode detection, but the surface limitation of CMOS chip hinder the microfluidic design too much. On the contrary, the chip-in-carrier procedure and the flip-chip topology that extending the workable surface is more likely to solve the system package. Utilizing the flip-chip bonding machine, the flip-chip bonding strategy have been developed for lab-on-CMOS package on a flexible polyimide PCB [169]. More mature topology, chip-in-carrier method, are studied by a lot of research group. As shown in Fig. 4.6 (a: i, ii), the chip-in-carrier package while etched

silicon wafer serve as the carrier have been developed by our group for biomedical applications via carefully alignment [170]. By deep-RIE, a silicon wafer was etched to serve as the carrier, and CMOS chip was put into the etched pattern following by passivation and metallization process. This chip-in-silicon method need very expensive equipment, and the vertical and transverse displacement between chip and holder because the un-avoided non-perfect alignment still stay as a challenge. Instead of utilizing etched silicon wafer as holder, we have also developed the epoxy or polymer based chip-in-carrier procedure, as shown in Fig. 4.6 (b) [171], [172]. In these chip-in-epoxy package system, self-alignment can be performed by utilizing the formation of the epoxy or polymer carrier by capillary force. At the same time, there are also several groups rely on undisclosed equipment to perform so called fan-out wafer level packaging (FOWLP), which can also be an option if the technology can be shared [173], [174][175]–[178].

4.2.4 Method for Continuous Classification

As mentioned in section 2.4, apart from the NIOSH published referenced method which typically require bulky and expensive equipment, several group have tried to develop the electrochemical methods, such as the square-wave anodic stripping voltammetry (SWASV) method, to perform miniaturized PM components classification [101], [102], [179]. However, the proposed methods typically require long time and complicated sample treatment before the electrochemical classification which can only been performed in laboratory environment and is not suitable for wearable real-time personal continuous PM classification. To address this challenge for real-time PM classification, separating the PM size and composition variables by real-time continuous size fractionation (as proposed herein), new options for composition analysis emerge. For example, it has been shown that when a particle collides with a microelectrode, transient interactions generate detectable events at the electrode [180]. Using electrochemical detection by electrocatalytic water oxidation, this modality enables

identification of unique interfacial electrochemical processes related to PM composition, especially for trace metals. By first removing the size variable, we plan to build upon this modality to generate a new method for real-time PM component classification.

4.3 A Platform for Real-time Continuous PM Monitoring

To enable a comparative analysis of approaches for a new PM monitoring platform, Table 4.1 summarizes the technology options from Section 4.2 for continuous PM assessment and defines pros and cons for each technology. From Table 4.1, the following conclusions can be drawn: 1) For PM capture, the well-developed ESP method is a better option than an anchored liquid to capture particles from air into liquid phase; 2) For size fractionation, the hydrodynamic DLD separation is preferred option because of its very high separation efficiency and multi-size separation capability; 3) For quantification, developing an electrochemical quantification platform or a parallel capacitive counter with vertical sidewall electrode exhibits better performance for continuous real-time monitoring; 4) For classification, electrochemical methods, especially the collision-based electrochemical classification strategy is well suited for use with the above technologies.

Table 4.1. Comparison of existing technology options.

PM design	**Tech options**	**Pros**	**Cons**
PM capture	Anchored liquid array	Easy fabrication	Low capture efficiency
	Electrostatic precipitator (ESP)	Acceptable capture efficiency	Complicated system
	Inertial air-liquid interface	High trap efficiency	Limited particle size
Size fractionation	Inertial impactor	Better penetration efficiency	Suffer from particle build up issue
	Virtual impactor	Avoiding the particle build up issue	Low separation efficiency
	Deterministic lateral displacement (DLD)	100% separation efficiency with multi size fractionation function	Device fabrication is more complicated compare to impactors
Quantification	Electrochemical quantification	Higher sensitivity; compatible with liquid samples	Limited resolution; lack of single particle counting capability
	Planar capacitive method	Easier fabrication procedure	Not suitable for real-time continuous detection
	Parallel capacitive method	Higher sensitivity; more suitable for flowing samples	Complicated fabrication procedure
Classification	NIOSH referenced method	Well developed	Bulky and expensive
	Electrochemical method	Miniaturized PM components classification	Less well studied and characterized

Based on this analysis, we have designed the wearable autonomous PM (aPM) platform shown in Fig. 4.7. This platform was designed to perform real-time continuous PM analysis, thus solving the challenges posed by the high spatiotemporal resolution and enabling the capability to perform quantification and component classification analysis across all/many PM size requirement. The PM capture component will serve as a pre-concentrator and extract PM from air and embedded it into liquid sample. Since PM that larger than 10 μm is of limited concern for exposure, PM10 size cut, such as commercially available exchangeable filters, will be integrated into the input of the system to exclude large particles and hold back possible clogging while using a miniature fan (e.g., ABS series, Delta Electronics) to pump air sample

into the platform. Following the PM capture component, PM contained liquid samples will be pumped through the microfluidic PM size fractionation component to produce five size-fractionized PM samples (PM10 – PM0.1) for the following PM quantification and classification. PM mass measurement (for concentration information) or PM counting (for single particle resolution measurement) as well as the elemental component analysis for PM samples across all five size will be performed separately within the PM quantification component and the PM elemental classifier, respectively. Miniature pumps (e.g., RP-TX Series, Takasago Electric) will be applied to provide negative pressure at the outlet of the microfluidic system to drive the PM samples in a flow rate range from 0.1uL/min to 1mL/min. For consistent measurement over a period of time (such as a day), reservoirs for buffer solution, electrolyte solution and waste liquid could be designed with ports allowing them to be filled and emptied, respectively. In the aPM platform, a CMOS chip for electrochemical or capacitive quantification together with a custom board instrument for electrochemical classification readout can be designed to apply electronic bias and provide readout function. Moreover, a commercial low power microcontroller with built-in Bluetooth module (e.g., CC2642R, TI) could be embedded for system control and front-end processing of measurement data such as PM mass estimation, and wireless connection to a smart phone, permitting user configuration and uploading data. Utilizing a periodic sampling routine that permits many of the system's components to cycle through low power states, the power consumption of the aPM monitor reducing power consumption can be restricted to only about 1W (mainly consumed by the ESP capture component and microfluidic pump). By embedding a rechargeable DC battery (e.g., LiHV+ 1600 4S), the aPM monitor is anticipated to operate for a few days (~1000 samples/day).

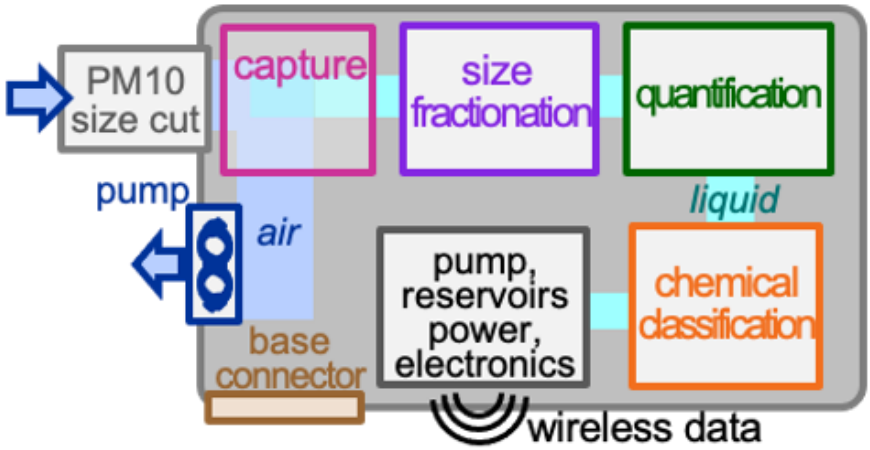

Figure 4.7. Schematic of the designed aPM monitor for real-time continuous, microfluidic-based size-fractionation, quantification, and elemental classification.

The aPM platform is also suitable for future expansion of functionality. For improved sensor performance with calibration of secondary sensitivities, temperature and humidity sensors could also be included to enable recording environmental variables along with PM exposure data. For battery charging, liquid samples refilling and liquid waste disposal, an aPM base station can be designed in a desktop format to performed maintenance every few days by simply connecting the aPM monitor to the base through the base connector. In addition, a custom software platform can also be applied to the system to enable automated sensor testing and curation of results.

By wearing the aPM monitor through individual' daily life, a quantified PM concentration (weight/volume or particle number/volume) as well as a PM element component exposure analysis (such as heavy metal ions and their concentration) will be expected to be collected as individual moves throughout various microenvironments. Moreover, by exporting the measurement results through wireless data communication, the user's smart phone can display personal exposure history and, optionally, share data with researchers to study the impacts of exposure and develop models for effective intervention.

In addition to the immediate benefits to users of the aPM monitoring system, a network of aPM devices offers tremendous potential for broader impact in exposure management. As shown in Fig. 4.8, a low-cost personal continuous real-time aPM system would enable a vast human network of data collected in real-time to generate the high spatiotemporal resolution necessary to better inform health impact analyses and subsequently develop effective intervention strategies to manage exposures and improve health. The aPM monitor would enable successful realization of well-informed interventions to reduce air pollution exposures and improve health of vulnerable and disproportionately impacted individuals, through effective policy and regulation (e.g., identification and reduction of contributing emission source sectors, changes to personal behavior/activity patterns). In the long term, the aPM system could facilitate real-time alerts and personalized exposure management strategies using future aPM-enabled health impact models. Furthermore, future aPM monitors could share data by users to create a live map of real-time local PM conditions or a myriad of other app/cloud-based services for enhancing public health and safety.

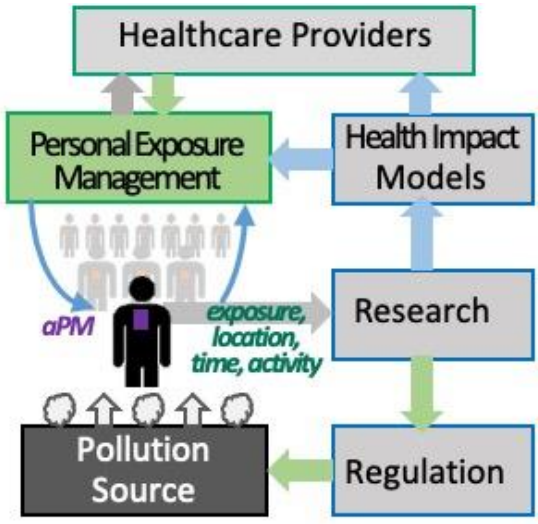

Figure 4.8. Model of airborne exposure illustrating the role of a personal PM monitoring system in personal exposure management.

4.4 Discussion

Although there are existing technology options that could be applied for particle trap, particle size fractionation, particle quantification, and the elemental component analysis, which are the four critical parts of the developed aPM platform, advancing the key technologies and the system integration to develop a functional aPM platform is still undetermined. As indispensable processes to streamline the implementation of the aPM platform for continuous real-time wearable PM monitoring, the electrochemical quantification and DLD microfluidic size fraction of PM will be studied in Chapter 5.

5 Advancing Key Technologies for PM Monitoring

PM is a very complex mixture chemically and physically (variable size and shape) and generally occurs in low concentrations (µg/m^3). Because both particle size and composition affect detectable PM properties (impedance, optical, etc.), common sensors are not suitable for component classification. As discussed in Chapter 4, the need for personal-level monitoring with fine spatial and temporal resolution, as shown in Fig. 5.1, makes it very challenging to develop tools that can truly identify and quantify PM component exposures in real-world, real-time applications. To address this challenge while developing the aPM monitoring system defined in Chapter 4, two key technologies, quantification and size fractionation, were developed. First, particle quantification utilizing electrochemical approach is presented in section 5.1. Then, size fractionation utilizing microfluidic DLD method is presented in section 5.2.

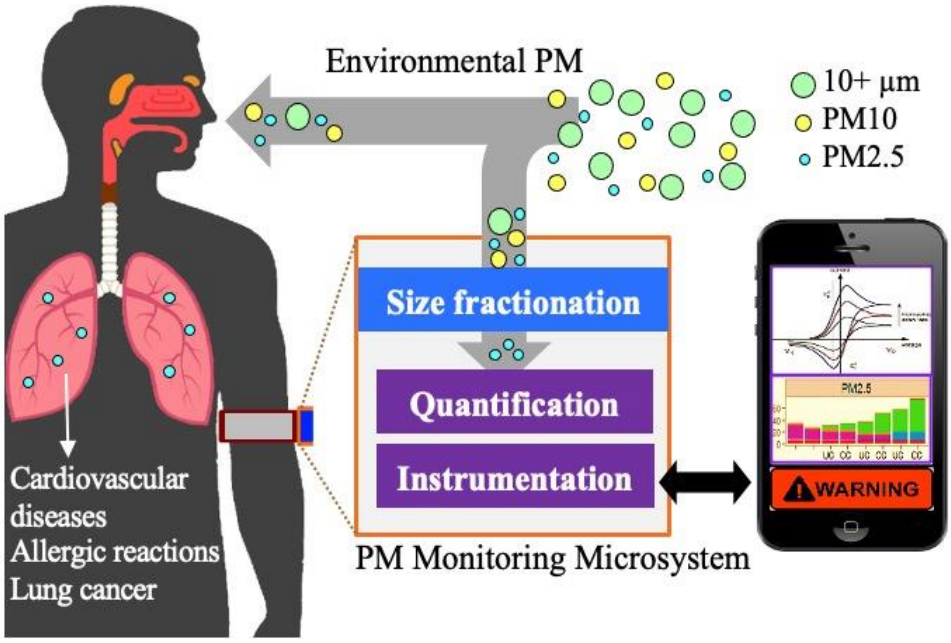

Figure 5.1. Concept of a portable/wearable fine PM monitoring system for measurement of acute individual exposure to particulate pollutants.

5.1 Electrochemical Quantification

To demonstrate electrochemical measurement of particle concentration for different size, multiple electrochemical methods, including AC impedance, cyclic voltammetry (CV) and differential pulse voltammetry (DPV), were performed with commercial carbon electrodes, commercial gold electrodes and microfabricated gold electrodes. Electrochemical measurements were performed using both commercial equipment and a custom thumb-sized, fully autonomous, electrochemical circuit that enables measurement results to be uploaded to smart device for signal processing, display and generation of local alerts. Called aMEASURE, the custom instrumentation module is based on a prior palm-sized system [181] and has the versatility to replace bulky electrochemical equipment for many sensor applications.

5.1.1 Sample Preparation and Test Setup

Major chemical components of PM2.5 and PM10 are nitrate, sulfate, ammonium, carbon, geological material, sodium chloride and liquid water. One study shows that the ionic carbonaceous composition of PM indicates that the PM was largely sulfate and organic carbon, with a significant fraction being elemental carbon [182]. Although the chemical components of PM vary, the physical properties, such as density and the surface properties, of PM2.5 particles are comparable to polystyrene latex beads of the same size, which make polystyrene beads a good model for PM2.5 particles in laboratory studies [183], [184].

Commercial polystyrene bead solutions (Sigma-Aldrich, 10 wt% concentration) were obtained with 1 µm and 10 µm particles. Each particle-containing solution was diluted by a factor of 10 and treated under ultrasonic for over 1 hour before each test to ensure the beads were not clustered. Several 80 mL samples with variable particle concentrations were prepared for electrochemical measurement. Each 80 mL sample contained 24 mL of electrolyte solution (8 mL KCl, 16 mL $K_3[Fe(CN)_6]$), *P* mL of particle-containing solution and (56-*P*) mL of DI

water, where *P* is a variable volume of 10:1-diluted particle-containing solution. *P* was varied from 0 to 5 mL and represents the relative particle concentration that increases with *P*.

According to product information, the number of the particles can be calculated by [183]:

$$N = (1.823*10^{11})/d^3 \quad (5.1)$$

where d is the diameter of the microparticle in microns. Based on equation (5.1), after dilution the 1 μm particle concentration for P = 0 mL, 1 mL, 2 mL, 4 mL and 5 mL samples is 0, 0.01252, 0.02504, 0.05008 and 0.0626 wt% (weight per volume), respectively. For simplicity, we just use P to represent the particle concentration in subsequent results.

For electrochemical measurements, a CHI 760 (CH Instrument, USA) electrochemical instrument was utilized for AC impedance, CV and DPV methods. Additional measurements using a custom thumb-sized electrochemical system are presented in section 5.1.6. Studies were conducted with commercial carbon, commercial gold, and custom microfabricated gold electrodes. All electrodes were immersed into beakers containing the 80 mL solutions of variable particle concentrations. Electrodes were cleaned between tests to avoid cross contamination between samples. The results below demonstrate some of the options available to designers who can analyze tradeoffs in cost, size, and performance to meet application needs.

5.1.2 Electrochemical Detection with Commercial Carbon Electrode

AC impedance measurement of PM concentrations with commercial carbon electrodes was previously reported by our group [185]. The distinctly different impedances observed due to particle deposition on the carbon electrode verify that electrochemical impedance can effectively detect samples of different particle sizes. For each sample, five repetitive tests showing good repeatability were reported.

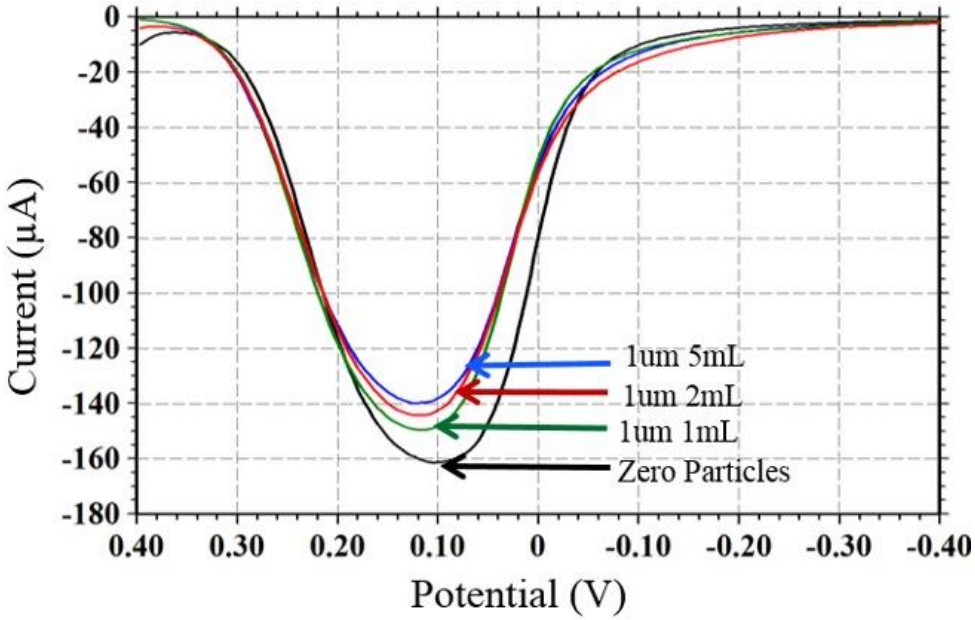

Figure 5.2. Differential pulse voltammetry (DPV) results with commercial carbon electrode for different sample solution, smaller current was collected for sample with higher particle concentration.

To study another electrochemical method with commercial carbon electrodes, DPV measurements were also performed. The voltage range was set from -0.4 V to 0.4 V with 4 mV increments, the pulse amplitude was 0.05 V, the pulse width was 0.2 s, the sample width was 0.01 s, and the pulse period was 0.5 s. As shown in Fig. 5.2, redox reaction currents were observed to decrease as concentration of 1 µm particles increased from $P = 0$ to $P = 5$ mL. This agrees with expectations since higher concentrations will result in faster particle deposition on the carbon electrode thus lowering the reduction current. The deposition of particles was verified by SEM images reported in [185] that show particles becoming trapped in the fibrous surface of carbon electrodes. This deposition limits the utility of carbon electrodes for long term continuous monitoring.

5.1.3 Electrochemical Detection with Commercial Gold Electrode

To overcome the particulate trapping limitation of carbon electrodes, gold electrodes were studied due to their very smooth electrode surface. A commercial gold electrode (CHI101) was chosen as the working electrode together with a platinum (CHI115) counter electrode, and a Ag/AgCl (CHI111) reference electrode. Cyclic voltammetry (CV) tests were first performed on different PM samples prepared. The voltage range was set from -0.2 V to 0.8 V with a 0.1 V/s scan rate. For each concentration, the same test was performed at least three times to assess repeatability. As shown in Fig. 5.3 (a), for the base "Zero Particle" sample, the redox current peak is the smallest, and the current increases with particle concentration. Based on the current increase observed through this test and the concentration of particles involved, the current sensitivity to a single polystyrene particle was calculated to be around 3 aA/particle. Based on the U.S. EPA National Ambient Air Quality Standard, the necessary limit of detection would be ~100 nA for unhealthy PM levels (PM concentration per day of 65.5-150.4 μg/m3 (particle count of 1.56-3.59 × 107) produces an unhealthy air quality index (AQI) of 151-200 [184]). Utilizing the DLD separation device as a preconcentrator and integration with high resolution CMOS electronics, this electrochemical measurement appears suitable for real-world PM monitoring.

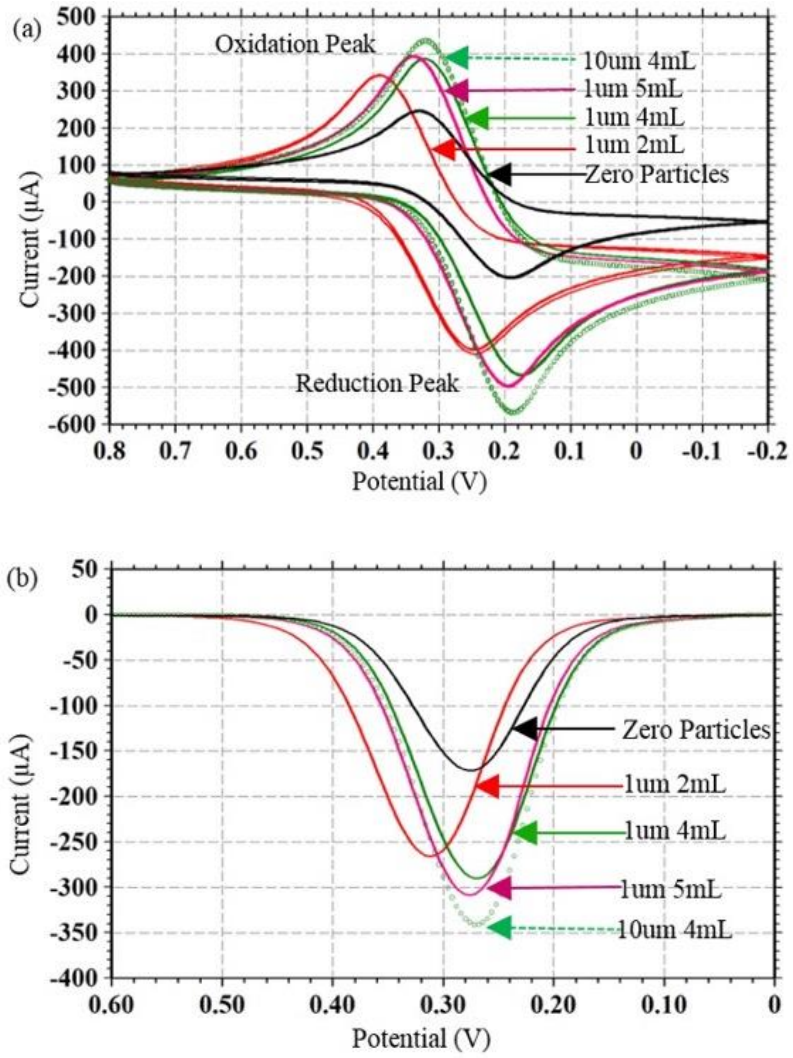

Figure 5.3. (a) Cyclic voltammetry (CV) measurements with commercial gold working electrode for five samples with different particle concentration and different sizes producing clearly distinguishable results; (b) DPV measurements result for the same sample solution.

To further study the PM-electrode reaction and improve sensitivity by extracting Faradic currents from the background charging current, the same PM samples were tested using DPV. The DPV stimulus voltage parameters were set to: range, -0.2 V to 0.8 V; step size, 4 mV; amplitude, 0.05 V; pulse period, 0.5 s; pulse width, 0.2 s; and sample width, 0.0167 s. As shown in Fig. 5.4 (b), the base "Zero Particle" sample shows ~170 μA peak current, and the redox peak current increase with particle concentration, as observed with CV. The variation between tests was calculated as around 1 μA, which verified that the DPV test is repeatable. The response at one concentration (P = 4 mL) was also measured for 10 μm particles, and the results

in Fig. 5.4 suggest that current increases with particle size.

5.1.4 Ionic Electret Theory Analysis

Notice that the results with carbon electrodes (Fig. 5.2) show current decreasing with PM concentration while results with gold electrodes (Fig. 5.3) show an increasing response with concentration. Because the particles in our study are non-conductive, one might naturally expect the conductivity of the sample, and therefore the response current, to decrease with PM concentration. However, both the CV and DPV results in Fig. 5.3 directly contradict that assumption.

Further analysis of the polystyrene beads surface characteristics suggests that the "ionic electret theory" can help explain the observed phenomenon. As reported by the Whitesides's group [186], [187], an electret is a material that has a permanent, macroscopic electric field at its surface, and ionic electret is a material that has a net electrostatic charge due to a difference in the number of cationic and anionic charges in the material. According to their definition, polystyrene micro-particles that contain a number of covalently bound sulfonate ions and a smaller number of sodium counterions are classified as ionic electrets. The product specifications for the polystyrene micro-particles used in our tests indicate that they were produced by polymerization of styrene under conditions that induce spontaneous coalescent bead formation [183]. The polymerization is terminated when two chains react to make a sulfate-terminated polymer chain. As reported in [187], these terminal sulfate groups located on polystyrene bead's surface contribute to a negative zeta potential (around -80 mV) that causes anions ($Fe(CN)_6^{-4}$) from the surrounding aqueous phase to preferentially accumulate on the particle surface, as shown in Fig. 5.4. Then, when the particles move toward an electrode surface, ions exchange will occur between the particles and the electrode surface, as previously reported [182], [186], [188]. The particles, working as ionic electrets, thus introduce another

path to help $Fe(CN)_6^{-4}$ move to the electrode surface. In summary, we believe that the micro-particles will enhance the diffusion process and amplify the redox reaction current. The bulk of naturally occurring PM consists of sulfate, organic carbon, and elemental carbon, all of which are all classified as ionic electrets [186], [189], [190]. Hence, we expect that natural PM particles will also enhance diffusion through the ionic electret effect during electrochemical measurements, though this hypothesis remains untested.

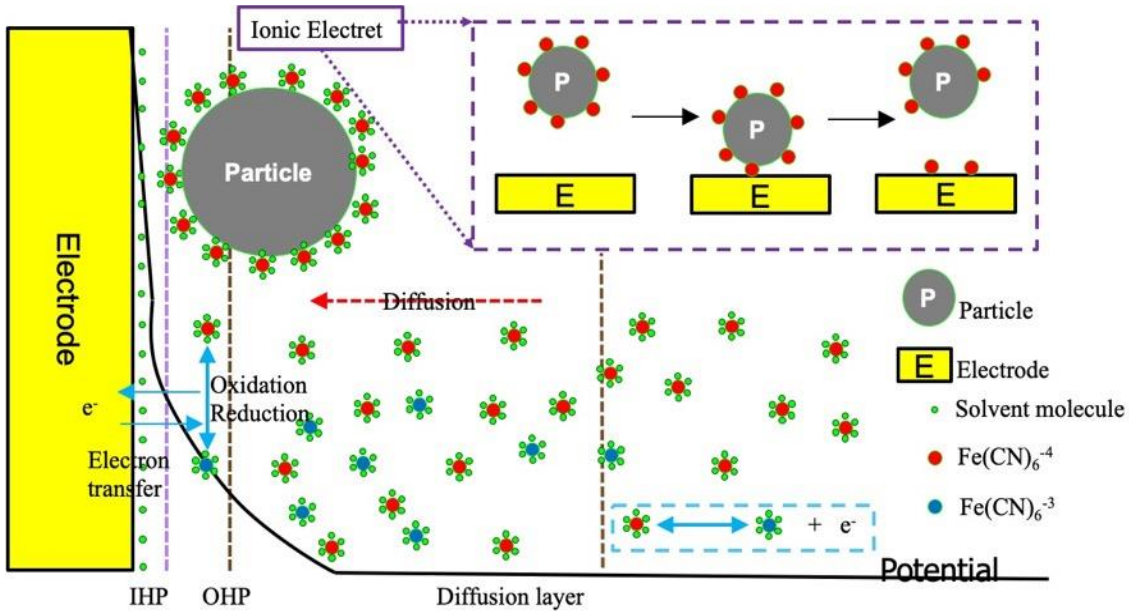

Figure 5.4. Electrode double layer schematic for ionic electret theory analysis. The IHP (inner Helmhotz plane), the OHP (outer Helmhotz plane) and diffusion layer are labeled. On the electrode surface, redox reaction of the Ferricyanide ions introduce electron exchange between ions and the electrode. The inset shows how particles in the solution work as ionic electrets that enhance the diffusion process.

Because we hypothesize that particles working as ionic electrets will only enhance diffusion, verifying that PM concentration does not impact kinetic current would further validate the hypothesis. For mass-transfer-controlled reactions, when no convection exists, Faradic current can be expressed as:

$$\mathrm{J}_i(x) = -\mathrm{D}_i \frac{\partial \mathrm{C}_i(x)}{\partial x} - \frac{\mathrm{z}_i F}{RT} \mathrm{D}_i \mathrm{C}_i \frac{\partial \phi(x)}{\partial x} \tag{5.2}$$

where $J_i(x)$ is the flux of ions at distance x from the surface, D_i is the diffusion coefficient, $\frac{\partial C_i(x)}{\partial x}$ is the concentration gradient at distance x, $\frac{\partial \phi(x)}{\partial x}$ is the potential gradient, and z_i and C_i are the charge and concentration of species *i*, respectively. Thus, equation (5.2) shows that Faradic current is the summation of diffusion and kinetic components. AC impedance measurements are commonly employed for detailed analysis of diffusion and kinetic induced current, with kinetic currents dominating at high frequency and diffusion at low frequency, as shown in Fig.5.5 (a). However, at low frequencies (lower than 0.1 HZ), measurement time is long enough for particles to settle out of the sample solution and falsify the test results. Thus, to test if PM concentration affects high frequency impedance, where kinetic currents should dominate, AC impedance tests were performed at 0.1 – 100k Hz. The resulting Nyquist plot in Fig.5.5 (b) shows that the high frequency results are constant for all PM concentrations with slight variations at lower frequencies where diffusion currents start to contribute. Because the kinetic current does not change with PM concentration, we must conclude that the observed response to PM (Fig. 5.3) is due to diffusion current. In turn, this confirms our hypothesis that the ionic electret effect only enhances the diffusion process without affecting kinetics.

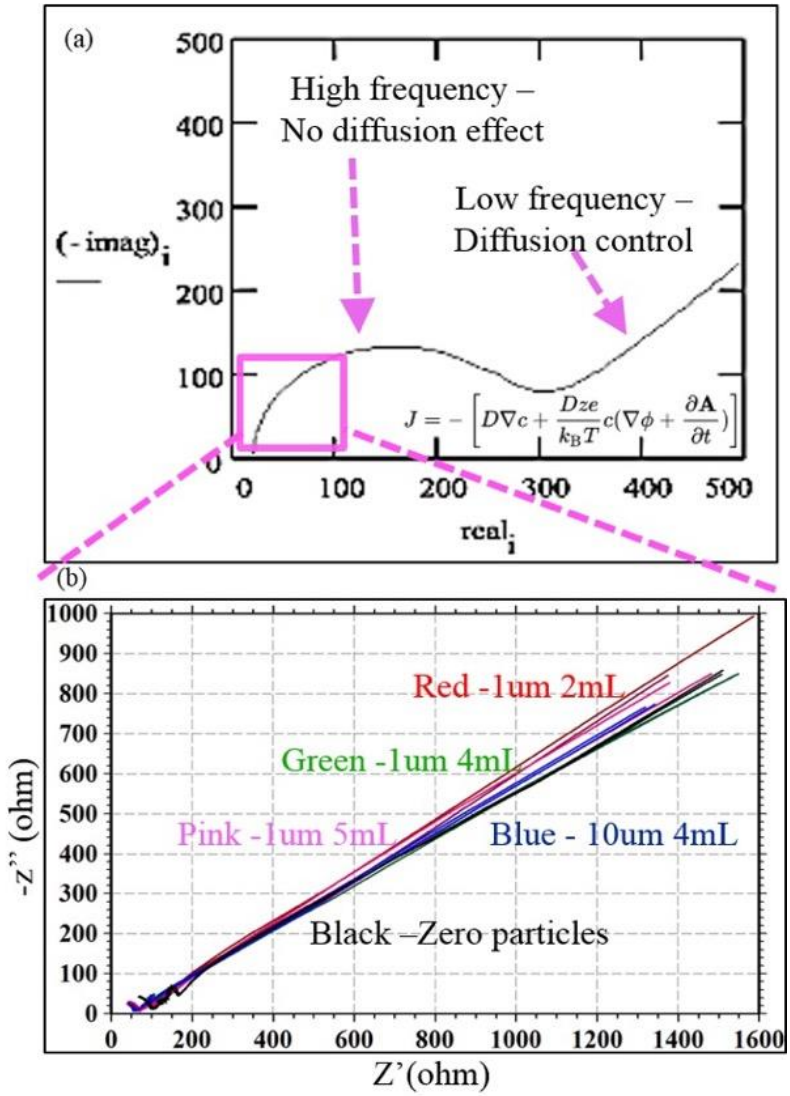

Figure 5.5. (a) The standard Nyquist plot for a mixed control model; (b) AC impedance measurements with commercial gold working electrode for different sample solutions.

5.1.5 Electrochemical Detection with Microfabricated Gold Electrode

Toward the goal of a portable, low-cost PM monitoring system, we fabricated miniaturized (0.13 mm^2) planar gold electrodes to compare their electrochemical performance with larger (0.78 mm^2) commercial electrodes. Gold was deposited on glass slides using thermal evaporation and patterned into electrodes using a lift-off process. PM samples with *P* = 0, 1, and 3 mL were prepared and both CV and DPV measurements were performed. The results in Fig. 5.6 show the same direct correlation between peak current and particle concentration as obtained with commercial gold electrodes. The net current amplitude is lower

by a factor of ~5 compared to the commercial electrodes, which is roughly the surface area ratio between the two electrodes.

5.1.6 CV measurement results with aMEASURE

To demonstrate that electrochemical particulate measurements can be performed with compact instrumentation, a custom module that produces electrochemical stimulus and records sensor response was developed. For portable or wearable applications, key attributes for instrumentation are small size and low power consumption for long operation lifetime from a battery supply. Versatility is also a key requirement because the instrumentation circuitry must seamlessly perform a diversity of electrochemical methods and be able to report results to a myriad of host systems, ideally with limited user intervention. To this end, we have designed a custom thumb-sized, fully autonomous, electrochemical readout circuit called aMEASURE, which is based on a prior larger system [181] and has the capabilities to replace bulky electrochemical equipment for many sensor applications.

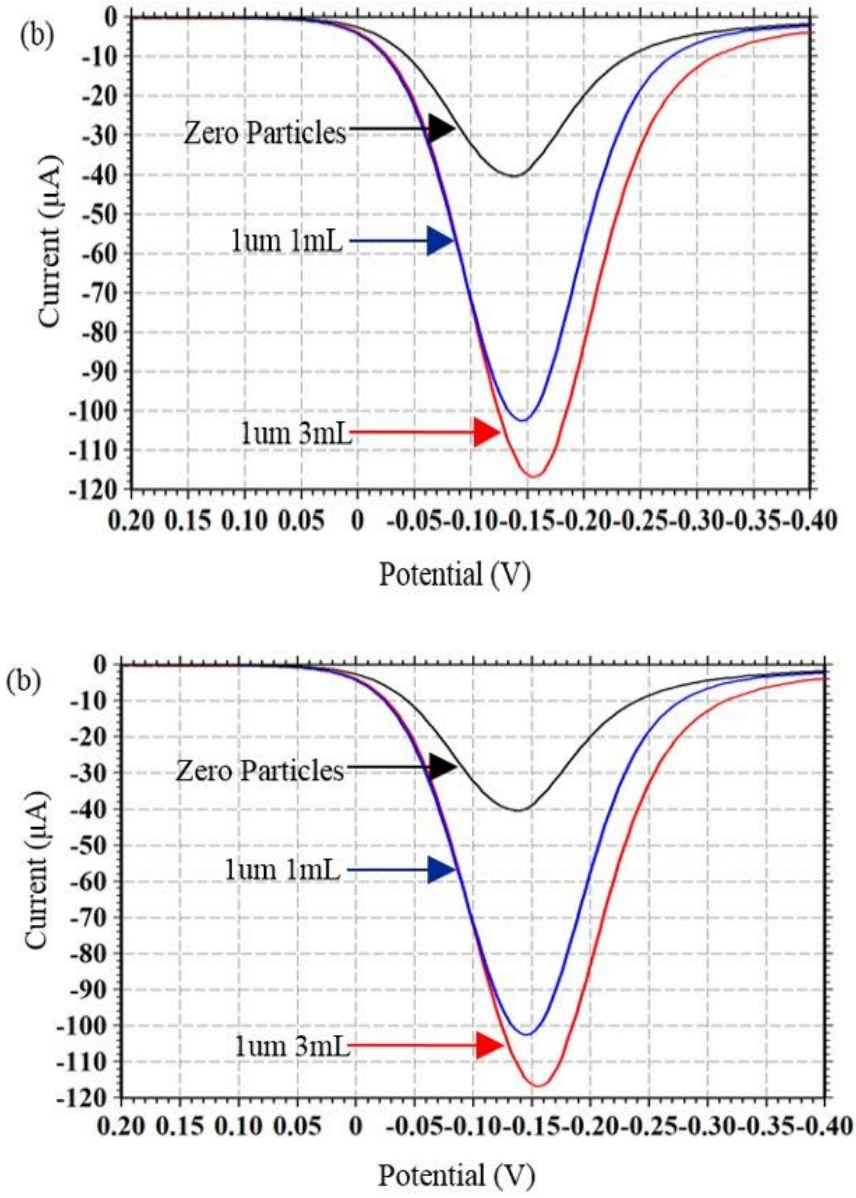

(b)
Zero Particles
1um 1mL
1um 3mL
Current (μA)
Potential (V)

Figure 5.6. Electrochemical tests with microfabricated gold electrodes: (a) CV results for three samples with different particle sizes producing clearly distinguishable results; (b) DPV results for the same three samples.

To verify PM sensing with the custom aMEASURE electrochemical instrument, it was connected to the commercial gold working electrode used in section IV.C, and CV measurements were repeated and compared with the commercial CHI 760c instrument. The results for multiple PM concentrations are shown in Fig. 5.7 (a). A calibration curve showing oxidation peak current vs. PM concentration is plotted in Fig. 5.7 (b) for both aMEASURE (Fig. 5.7 (a)) and CHI760 (Fig. 5.3 (a)) instruments. The maximum standard deviation across

4-6 measurement cycles was 2.2 µA for aMEASURE and 6.7 µA for CHI. The linear trend lines show a very similar response curve from the two instruments and validate the capability of aMEASURE to perform electrochemical PM measurements in compact/wearable form.

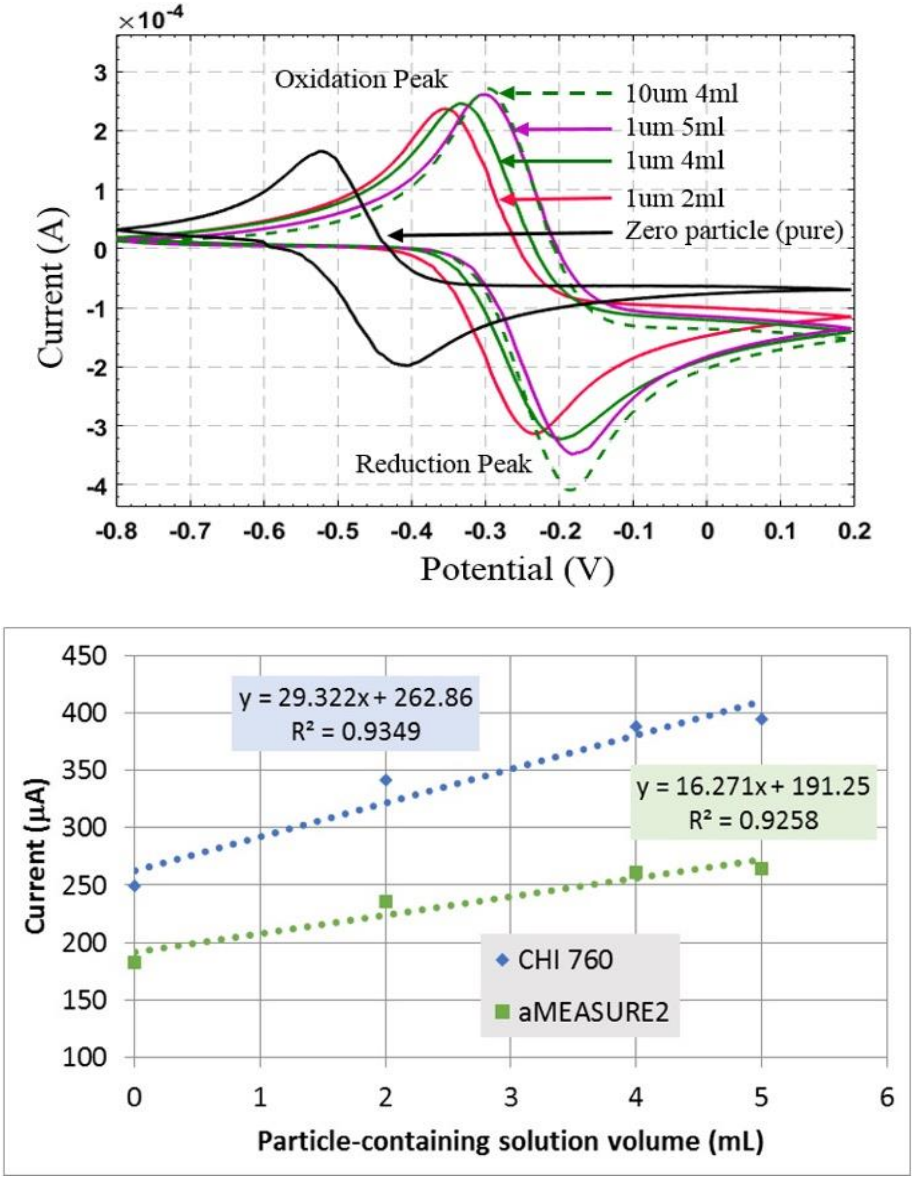

Figure 5.7. (a) aMEASURE CV test results with commercial gold working electrode for different sample solutions; (b) Oxidation peak current vs. 1 µm particle concentration and linear fit lines for aMEASURE and CHI instruments.

5.2 Microfluidic Size Fractionation

DLD separation method provides the capability to continuously separation particles with high separation efficiency, resolution, predictable and easy operation. In order to effectively

implement the proposed electrochemical quantification method, specifically based on the ionic electret effect, the DLD separation module is placed ahead of the quantification module. For microfluidic particulate separation, we adopted the deterministic lateral displacement (DLD) method [191] that utilizes asymmetric bifurcation of laminar flow around pillar arrays for particle separation. Particles choose their path through the pillars deterministically based on their individual size, which produces high separation efficiency with very high size resolution. By carefully designing the pillar size, spacing and array gradient, a DLD microchannel device can separate particles above a specified critical size. Particles larger than the critical size are bumped off their initial flow path and displaced laterally to follow the designed pillar gradient. In contrast, small particles less than the critical size continually flow along their original fluid streams unaffected by the pillar array. Utilizing the DLD method, I-shaped pillars have been reported that will induce a rotation in non-spherical particles that can enhance the separation efficiency [148], [192]. Because PM is also irregularly shaped, we chose to incorporate I-shaped pillars into our separation microchannel to increase separation efficiency.

5.2.1 I-shaped DLD Separation for PM Size Fractionation

The basic principle of DLD separation [193] is illustrated in Fig. 5.8, which shows the flow of particles that are larger and smaller than the critical separation diameter of the array. Large particles will bounce along the pillars and follow the pillar gradient, displacing them from their laminar streamline and projecting them toward the bottomof the microfluidic channel. In contrast, small particles less than the critical size continually flow along their original fluid streams unaffected by the pillar array. As reported, 0.1 μm resolution can be achieved with a high separation DLD design [193]. However, due to the anisotropic effect, how particle around the critical diameter would perform in a DLD device can vary in traditional circle pillar based DLD device [194]. We have used I-shaped pillar design wherein the grooves inside them introduces a rotation of non-spherical particles that enhance the separation

efficiency, decreasing the chance for them to return to their laminar streamline. This rotation is also illustrated in Fig. 5.8. In contrast, small particles take a zigzag path to follow the laminar streamline, occasionally sliding upward between pillars to follow their initial streamline and projecting toward the middle of the microfluidic channel.

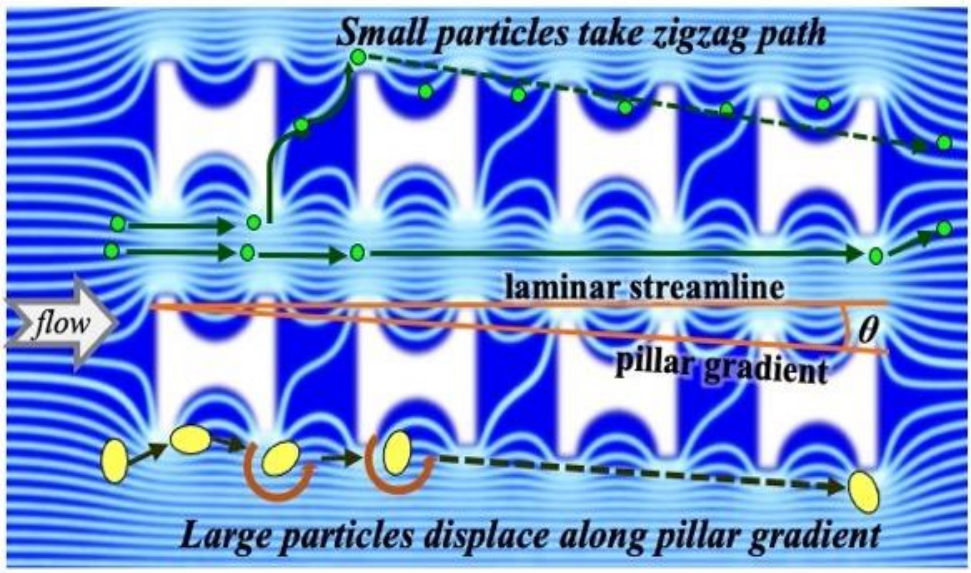

Figure 5.8. Illustration of the DLD separation principle with I-shaped pillars. Streamlines are as shown as white lines. Small particles follow their initial streamline paths while large particles are pushed along the pillar gradient.

For DLD pillar arrays, the size of particles that will be separated from the streamline is determined by the gradient of the pillar array. The critical separation diameter, D_C, which is the minimum diameter of particles that will follow the pillar gradient (i.e. separate from the streamline) can be calculated by [148]:

$$D_C = 1.4gN^{-0.48} \tag{5.3}$$

where g is the gap size between pillars and N is number of rows (in direction of laminar flow) per shift in columns (perpendicular to laminar flow).

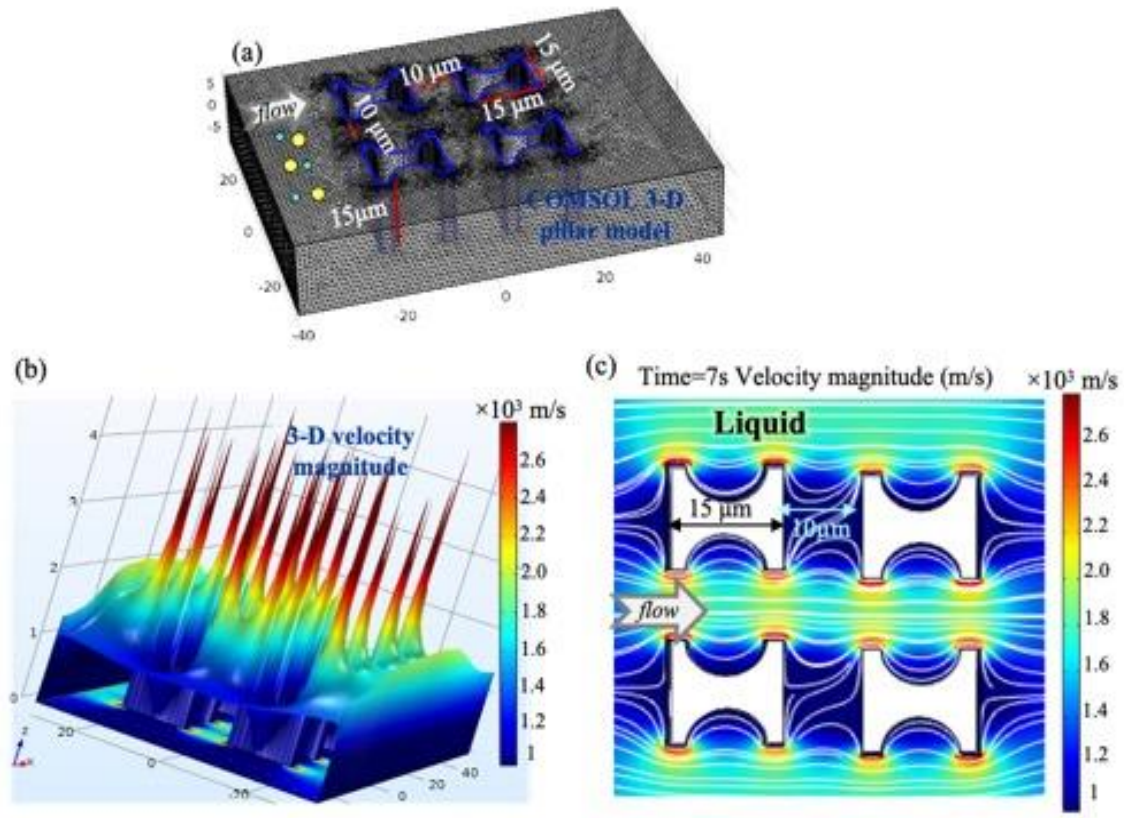

Figure 5.9. COMSOL 3-D model and simulation results for I-shaped pillar in a DLD microchannel: (a) the 3-D model with fine mesh defined; (b) the velocity magnitude (m/s) distribution at time = 7 sec in liquid at 20°C with the density set to 1000 kg/m^3, the dynamic viscosity set to 8.90×10^{-4} Pa-s, and the kinematic viscosity set to 1.0035×10^{-6} m^2/s; (c) 2D projection of velocity magnitude (m/s) distribution of mid-plane at time = 7 sec.

To design the PM microfluidic separation device, COMSOL Multiphysics fluid flow simulations were performed for a DLD structure with I-shaped pillar array. This study provided insight into the fluidic velocity profile and the effect of the pillar array on laminar flow in liquid samples with 2.5 µm as the critical separation diameter. Fig. 5.9(a) shows the COMSOL 3D model of a 4-pillar segment. Following the reported DLD design approach that will separate micro particles of various sizes [9], we chose the I-shaped pillars to be 15 µm × 15 µm × 15 µm (height) with a 10 µm gap between pillars. Fig. 5.9(b) shows that the 3D simulated velocity magnitude exhibits peaks at the corners of the pillars as predicted by DLD theory. Fig 5.9(c) is the 2D projection of the velocity magnitude distribution at the middle of the pillar height showing simulated streamlines. COMSOL simulation shows that large particles passing

between pillars will experience different velocities along different portions of the particle, which can induce rotation that helps the particle follow the pillar gradient and thus enhance separation efficiency. Fig. 5.9(b) results were obtained using a liquid sample with physical parameters listed in the figure caption that were taken from [195]. To separate particles greater than 2.5 μm for PM 2.5 monitoring, D_C = 2.5 μm. For g = 10 μm, calculation from equation (5.3) shows that $N \approx 41.8$. The angle of the pillar gradient, θ, shown in Fig. 5.8, can be determined from

$$\theta = tan^{-1}(1/N) \tag{5.4}$$

For N = 41.8, $\theta \approx 1.4°$ was used to set the pillar gradient.

5.2.2 I-shaped DLD Microchannel Fabrication

The separation device consists of a microchannel on a silicon wafer and PDMS lid, and a detailed fabrication process is as shown in Fig. 5.10 (a, b, c). Firstly, a microchannel with an I-shaped pillar array was constructed in a silicon water using deep reactive ion etching (deep-RIE). In step 1, the wafer was first spin coated with HDMS to improve adhesion of SPR220 photoresist that was spin-coated at 2000 rpm to form a 3.15 μm layer and patterned using photolithography. A 90 second prebake at 115ºC and 5 second exposure through the photomask were then performed and followed by a 90 second post-bake at 115 ºC. AZ 726 was then used to develop the SPR220 to transfer the pattern. The device was then etched using deep-RIE (STS Pegasus) to produce approximately 15 μm depths. In step 2, the PDMS lid was created using the soft lithography fabrication process shown in Fig. 5. 10(b). After curing, the PDMS was peeled off the silicon wafer and cut into blocks ~20-30% larger than the microchannel dimensions, and then the inlets and outlets were punched into the solid PDMS block. Lastly, in step 3, oxygen plasma treatment was performed on both the PDMS and silicon microchannel

to prepare them for bonding. A mask aligner was used during the bonding process to ensure that the inlets and outlets on the two components were properly aligned. The bonded device was then thermally treated in an oven at 130 ºC for more than 1 hour to enhance the bonding strength.

The final fabricated microchannel is shown in Fig. 5.10(d) along with a close up of the fabricated I-shaped DLD pillar array. The height of the overall microchannel was set as 15 µm and the overall microchannel width (W) was set to 2 mm and the length (L) to 20 mm. The sample inlet was placed in the middle of the channel while buffer inlets enter to the left and right of the sample inlet to ensure the sample entered in the middle of the DLD separator microchannel. At the outlet, the long pillar separation channel was divided into 40 columns that were then binned into three fluid outlet channels. The DLD microchannel was designed to displace all particles larger than 2.5 µm to the "Bottom-out" outlet while allowing particles smaller 2.5 µm to a maintain a laminar flow path and exit at the "Middle-out" outlet.

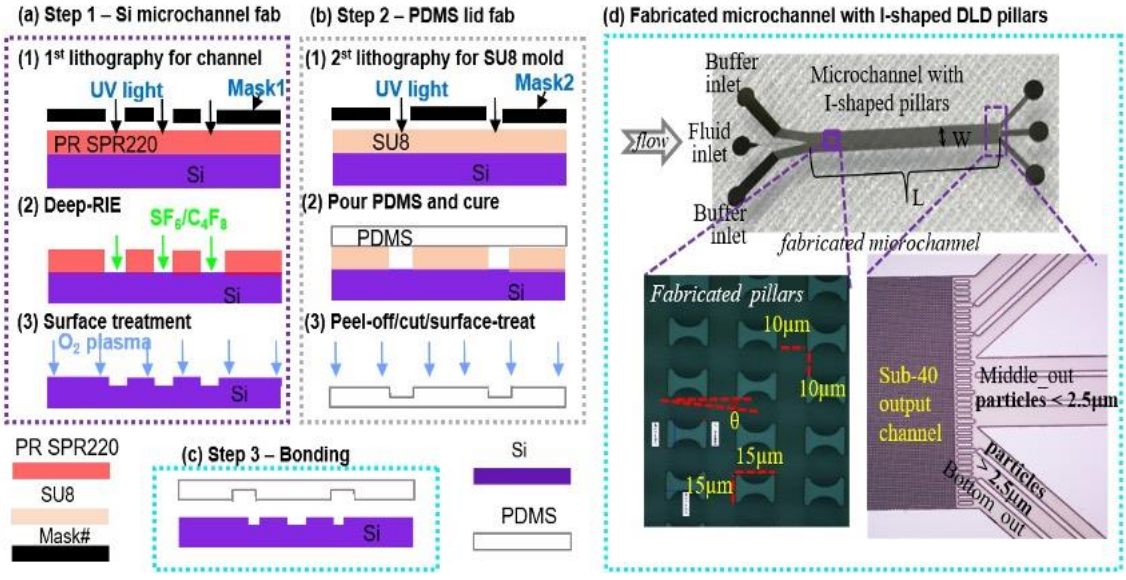

Figure 5.10. (a, b, c) Fabrication process for an I-shaped DLD pillar array microchannel; (d) The fabricated microchannel showing pillar dimensions and routing of the 40 channel outputs to three fluid outlets where particles are separated by size.

5.2.3 Particle Separation Results

To verify microfluidic particulate separation, polystyrene beads were chosen because they are commercial available in various sizes appropriate for PM studies and have the same density as PM [28, 29]. Prior to separation experiments, 1% w/v Pluronic F127 (Sigma Aldrich, USA) and DI-water were pumped into the microfluidic device to avoid clustering of particles as well as adhesion of particles to microfluidic channel walls. 1 mL of 1 µm and 10 µm polystyrene bead solutions (10 wt% concentration, contain 1 µm and 10 µm beads ~1) were both diluted 10 times before mixing to prepare the test sample. The experiment setup is shown in Fig. 5.11 (a), where the test sample solution containing the diluted mix of 1 µm and 10 µm particles was pumped into the sample inlet at the rate of 0.5 µL/min using a syringe pump. Two other syringe pumps were then used to introduce phosphate-buffered saline (PBS) buffer solution into side inlets at the rate of 0.2 µL/min. As seen in Fig. 5.11 (a), the solutions exiting from the three device outlets were collected in separate reservoirs. The entire separation experiment was recorded using a camera attached to the microscope on top of a probe station.

Because the sample solutions were pumped in the middle of the microfluidic channel, the smaller particles were expected to appear in the Middle-out and larger particles at the Bottom-out outlets. Following repeated experiments with the same results, the recorded videos clearly show the 10 µm polystyrene beads being shifted to flow along the pillar gradient to the Bottom-out outlet. As desired, the 1 µm polystyrene beads were observed to follow their initial flow paths to collect at the Middle-out outlet without being affected by the pillars. These results exactly match design expectations. To further confirm the separation efficacy, samples from each of the collection reservoirs were extracted by pipettes and examined under a microscope. As shown in Fig. 5.11(b), the Bottom-out outlet contained only 10 µm particles with no observable 1 µm particles, while the Middle-out outlet contained only 1 µm particles with no observable 10 µm particles. Additional experiments were run to observe the impact of flow

rate on separation performance. As expected, at low flow rates, below 0.1 µL/min, 1 µm particles were occasionally observed at the Bottom-out outlet due to particle diffusion.

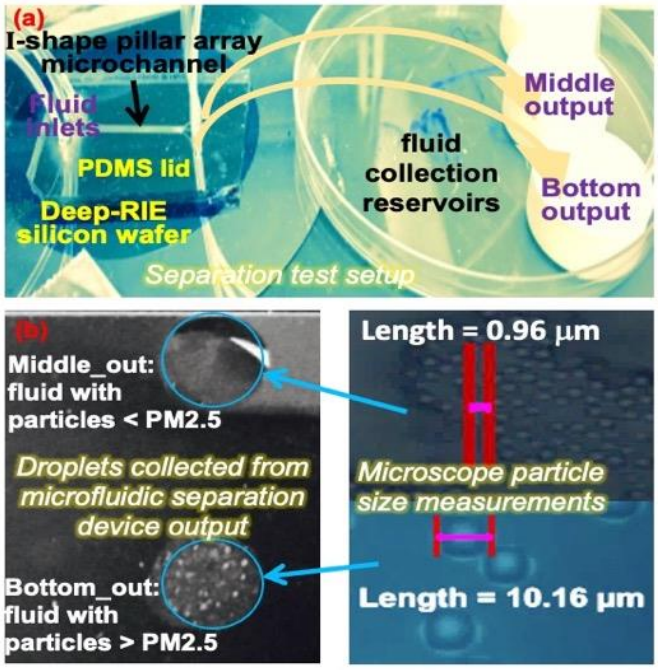

Figure 5.11. Particle separation device test setup and results: (a) the DLD separation device consist of a deep-RIE silicon microchannel and PDMS lid and separates large particle to the bottom (Bot) output; (b) Samples collected from the output and measured by a microscope show that the particles were properly separated.

5.3 Discussion

Two key technologies of the aPM monitoring system, quantification and size fractionation, was developed in this chapter. The new approach for continuous quantification of particles that expresses a resolution suitable for fine PM measurement and a capacity for miniaturization to support wearable monitoring using a unique combination of particle size fractionation and electrochemical quantification. However, as expected, large particle in electrochemical measurement can present same result compare to multiple small particles if the total surface area is same. Due to this reason, measuring particle concentration accurately required particles of uniform size. To address this challenge, integrating the electrochemical quantification and size fractionation together, we have developed the platform described in Fig. 5.12, which,

following the architecture of Fig. 5.1, consists of a size fractionation module utilizing microfluidic DLD separation and a quantification module featuring electrochemical methods. This combination was specifically chosen to provide real time, continuous, and wearable implementation that enables high spatial and temporal resolution in exposure monitoring, at multiple PM ranges, as individual moves throughout their daily lives.

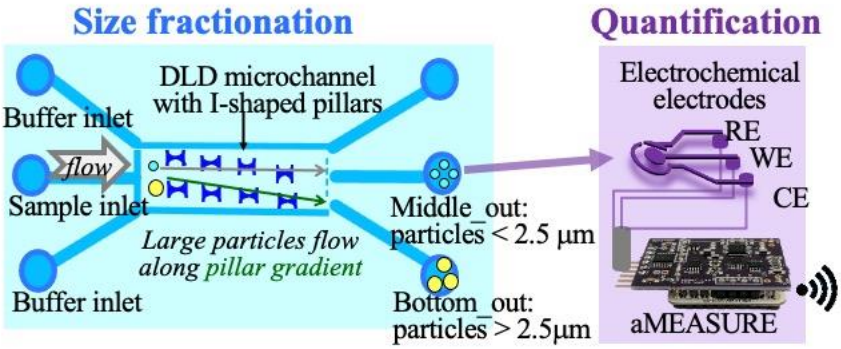

Figure 5.12. Platform for PM2.5 monitoring consisting of separation and detection components.

6 Externally Balanced Cascade DLD for High Dynamic Range Multi-Size Particle Separation

6.1 Motivation

Utilizing the I-shape pillar based DLD separator, we have achieved particle size fractionation across one size, which was set as 2.5 μm. However, the health-relevant PM size range of PM arguably spans from coarse particles PM10 (<10 μm) to ultrafine particles, PM0.1 (<100 nm). Due to the critical role of PM size in determining the health and welfare impact, continuously particulate matter monitoring through microfluidic technologies strongly desire multi-size particle separation function, which can provide the analytical capability across many/all size fractions of the real PM samples [34]. In order to enable environmental health researchers to explore the impact of all relevant PM sizes of airborne PM over the relevant range of aerodynamic/hydrodynamic diameter, PM size separation that enable size-fractionated quantification and classification across all/most of the relevant PM size is required.

DLD devices are inherently designed to separate most efficiently at a single critical size, where expanding the dynamic range of separation quickly results in impractically large devices. Within the developing of single critical dimension DLD technology, a few efforts have been reported for multi-size DLD separation, but they resulted in either separation of only a small dynamic range of particle size or higher dynamic range at the cost of very long devices formed in a serpentine pattern [196], [197], [198], [199]–[207]. These prior efforts implement multi-section DLD devices where each section separates at a different critical size by varying only the pillar gradient, resulting limited dynamic range or extremely long channel. Toward a goal of expanding the dynamic range of particles sizes (with wide spectrum also) that can be separated, in this chapter, we will present a cascaded multi-size gap scaled DLD separator design that permits enlarging dynamic range of size fractionation while optimizing overall device size. Detailed multi-section mathematical model that permits analysis of design

tradeoffs and simulation results from this model are presented in section 6.4 and 6.5 to help designers better understand the design considerations of externally balanced cascaded multi-section DLD separators.

6.2 Externally Balanced Cascade DLD Approach

6.2.1 Externally Balanced Cascade DLD Approach

Theoretical operation of single DLD separation is well established and relies on laminar flow through a periodic array of micrometer-scale pillars, shown in Fig.6 1(a). Varying other pillar geometry parameters, namely the pillar gap, *g*, and pillar size, *w*, we developed an externally balanced cascade DLD approach which can expand the design space and allow a high dynamic range of separation sizes within reasonably long device channels. As shown in Fig.6 1(b), utilizing the cascaded DLD strategy, an externally balanced cascade DLD with section scaling design was designed for multi-size particle separation with a wide dynamic range. In the presented three sections, adjacent to each other, critical diameter has been gradually decreased due to the gap scaling design. Take the second section as an example, Dp2, particle larger than Dc2, will be displaced which can be collected from the output in second section, while all other particles, including Dp3, with a diameter smaller than Dc2, will be conducted into next section for further size fractionation.

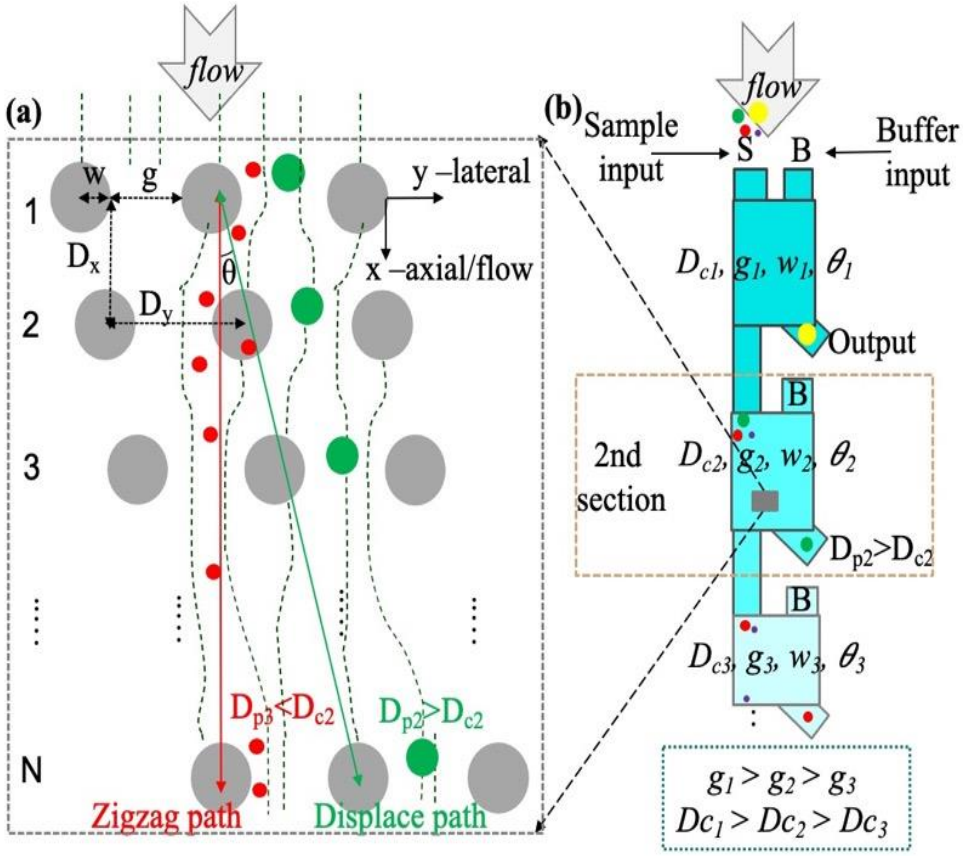

Figure 6.1. (a) Illustration of pillar array for DLD separation showing key model parameters, and (b) concept diagram for externally balanced multi-size DLD separator with multiple cascaded gap-scaled sections.

6.2.2 Fluidic Mechanisms and Design Rules for Multi-section DLD

Because of the lack of understanding of flow filed and particle dynamics in inertial DLD flows with Reynolds number well above unity, currently, DLD devices mainly focus on Reynolds number smaller than unity which determine that the fluid inside the microchannel will work in a laminar or even creeping flow model [208]. Although fluid-only predictions are insufficient to explain experimentally observed critical size behavior, simulation measures agree well with the analytical prediction from an assumed parabolic velocity profile that a finite size limit on experimentally achievable often used row shift range ($0 \leq \varepsilon \leq 0.1$) [208], [209]. In this paper, aiming in applications that work in laminar flow or creeping flow, Reynolds number was set as smaller than 1 and the row shift was set within the range ($0 \leq \varepsilon \leq 0.1$). Although full understanding of particle mode behaviors remains elusive, decades of work on

DLD have concluded that to design a multi-section cascaded DLD device, there are three critical parameters that have to be considered: hydraulic resistance, gap/pillar ratio, and anisotropic affect.

Firstly, hydraulic resistance balance across the lateral direction is critical for all kinds of DLD design. Unbalanced hydraulic resistance design will certainly contradict the predictable intrinsic particle movement due to the great lateral pressure induced by the resistance difference across the interface. In addition, being aware of the hydraulic resistances of each component is the key to determine the applied pressure for successive operation of the DLD system.

The second figure of merit that is essential in design is the gap/pillar ratio that not only affects the pressure drop but also determines the surface area-to-volume ratio for a given overall channel geometry [210]. Moreover, vary the aspect ratio also correlated to the hydraulic resistance modification. In the meantime, pillar shape not only affect how particle was displaced, but also will determine the achievable pillar and gap size range due to fabrication limitation.

Thirdly, anisotropic effect, which will reduce the in-situ critical diameter, has to be carefully considered. The most apparent example is the fluidic resistance of an array of obstacles along the channel wall will introduce lateral pressure difference thus inducing the anisotropic effect. How to design the pillars in the boundary to reduce the anisotropic effect has to be carefully considered when design a DLD device [211][212].

Another parameter that affects the device length or critical size behavior is the D_x/D_y ratio. Modification to row shift fraction can be used to replace the traditional model if chose D_y not equal to D_x [213]. However, the relationship between the D_x/D_y ratio with D_c size is not fully explored. In this paper, we assume D_y equal to D_x. Channel depth is also a critical design

parameter. Increasing the device depth will certainly decrease the array's flow resistance and reduce clogging, however, will limit the pillar or gap feature size due to the surface aspect ratio limitation from the fabrication capability. In this paper, considering about the high dynamic range purpose, we set depth to be larger than the biggest particle, D_{p_max} (D_p, is defined as the hydrodynamic diameter of particle), to avoid particle clogging.

After choosing the design parameters for specific application consideration, the hydraulic resistance of each section can be calculated, suitable balanced methodology, such as long serpentine microchannel design or commercially available value, can be used to balance the hydraulic resistance between sections. Then, by comparing different groups of design parameter choice, the total device length can be set as a figure of merit to analyze the trade-offs. As a summary, all parameters that will be used in this paper are specified in Table 6.1.

Table 6.1. Definition of important variables for the design of externally balanced cascade DLD devices.

Variables		**Definition**
D_{ck}		Critical diameter of particle
D_p	D_{p_max}	Biggest particle that will be separated
	D_{p_min}	Smallest particle that will be separated
w		Diameter of the pillar
g		Gap between pillar (in lateral direction)
D_x		Center to center distance in flow direction
D_y		Center to center distance in lateral direction
L		Total length of the device
NoS		Number of sections
SSF		Section scaling factor
N		Number of rows required for one column shift
γ		Pillar diameter to gap ratio ($\gamma = w/g$)
β		1.1 – design tolerance
θ		The gradient angle ($\tan(\theta)=1/N$)
m		1 (number of columns to be displaced)

6.3 Multi-section Mathematic Model

Based on the fluidic mechanism and design rule analysis, setting the pillar array is the start of a DLD device design. Once the pillar array design parameters are defined, the length of each section and then the whole DLD device can be geometrically calculated. This is important because a key objective when designing a DLD device is to keep its length as short as possible, while maintaining high separation performance. In fact, shorter devices not only have less flow resistance thus increase the throughput but also require less space.

From theoretical analysis and experimental verification, the critical separation diameter and the pillar gradient can be calculated by [148], [214]

$$Dc = 1.4gN^{-0.48} \tag{6.1}$$

$$\tan(\theta) = 1/N \tag{6.2}$$

where g is the gap between pillars and N is the number of rows needed for particles larger than D_c to be shifted by one column from its original position.

The length of a DLD device can be calculated by

$$L = mND_x \tag{6.3}$$

where D_x is the center-to-center distance of the pillar in the flow direction and m represent the number of row-shifts chosen to ensure adequate separation at the output.

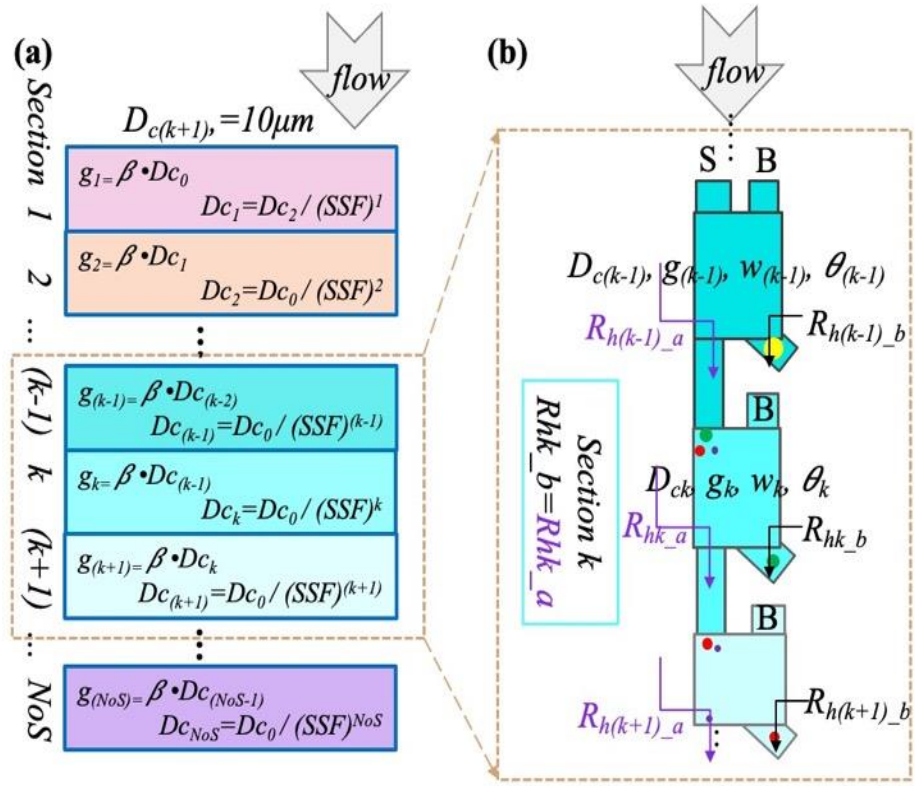

Figure 6.2. Mathematical model that permits analysis of design tradeoffs: (a), the mathematical model shows the relationship between g and D_c with the *SSF* and *NoS* set, (b) section *k-1, k*, and *k+1*, as examples to illustrate how the hydraulic resistance should be externally balanced.

To develop a model for our gap-scaled multi-size DLD separation device, as shown in Fig 6.2, we firstly assume that each cascaded section of the device separates at an increasingly small critical size where a section scaling factor (SSF) defines the critical size ratio from one section to the next. Thus, for any section, *k*

$$Dc_{k+1} = Dc_k/SSF \tag{6.4}$$

Notice that, for any total number of sections (NoS), the separator will generate NoS+1 unique size output. Assuming the left output of each section is input to the next section in a cascade fashion, to avoid clogging the gap in any section needs to be larger than the largest incoming particle, which is determined by D_c of the prior section. Thus,

$$g_{k+1} = Dc_k \cdot \beta \tag{6.5}$$

where β is a design tolerance variable that is set to 1.1 in this work to avoid particle clogging in all sections. If we further assume that cascading sections require that the ratio, γ, between the pillar size and the pillar gap be a constant across all sections, then we have

$$w_k = g_k \cdot \gamma_k \tag{6.6}$$

where the optimum choice of γ_k will be studied in Section 6.5. According to the fluid mechanism study, γ_k can be set as >1 for easier fabrication procedure consideration [210], and as <1 for possible adjusted migration angle consideration [215].

Since D_{p_max} is defined as the largest particle size at the input of section 1, then equation (6.4) and (6.5) permit the following general expressions for any k^{th} section

$$Dc_k = \frac{Dc_0}{SSF^k},\ g_k = \beta \cdot \frac{Dc_0}{SSF^{(k-1)}} \tag{6.7}$$

In this work, D_{p_max} was set to 10μm. This expression allows us to define the maximum resolution (smallest separated particle size), D_{p_min}, for a device with NoS sections as

$$D_{p\_min} = Dc_{Nos} = \frac{Dc_0}{SSF^{Nos}} \tag{6.8}$$

Due to the known tradeoff in DLD separation between device length and particle resolution, we can complete the model by expressing the length, L, of a multi-section device as the sum of lengths of all k^{th} sections using equation (6.3) and (6.6), thus

$$L = \sum_{k=1}^{NoS}[m \cdot N_k \cdot g_k(1+\gamma_k)] \tag{6.9}$$

where N_k is related to D_{ck} and g_k by equation (6.1). In this work, m was set to 1 and the other design parameters are defined above. To explore the design space for multi-size DLD separation with gap-scaled cascaded sections, these modeling equations were implemented in

MATLAB (code in Appendix II) and simulation results across several parameters of interest are presented below.

6.4 Modeling Results and Analysis: Theoretical Limits

The externally balanced cascaded DLD model was first simulated to see relationships and design tradeoffs without any practical fabrication limits. The device length, L, and the separation device resolution, D_{p_min}, were explored to defining the optimal range of the number of sections, *NoS*, and section scale factor, *SSF*. In this preliminary analysis, because the pillar and gap can be as small as we desire ideally, as a start point, in this section, we set γ_k as 3.

6.4.1 L vs NoS Relationship for Different SSF

Fig. 6.3. shows the relationship between total length of the multi-size DLD device and *NoS* for different values of *SSF* ranging from 1.5 to 3.4 with 0.2 steps. This plot shows that L increases with both NoS and *SSF*, as expected. However, L saturates for NoS larger than ~5-10. This reflects the fact that, due to scaling the gap size down, the length of each subsequent section is smaller and smaller, allowing total length to show reach a saturation point that varies with *SSF*.

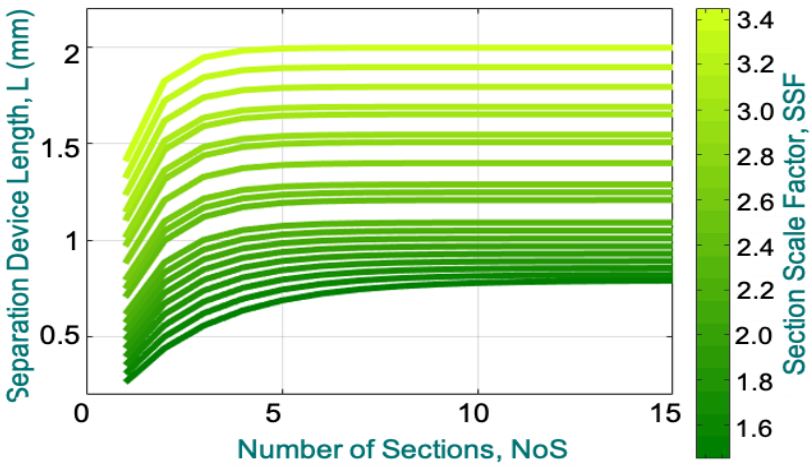

Figure 6.3. Total device length (L) as a function of number of sections (*NoS*) and section scale factor (*SSF*).

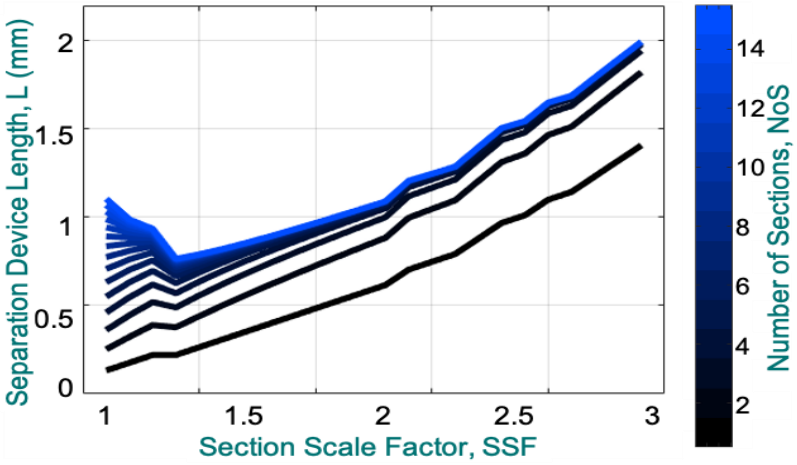

Figure 6.4. Total device length (*L*) as a function of section scale factor (*SSF*) for different values of number of sections (*NoS*).

6.4.2 L vs SSF Relationship for Different NoS

Fig. 6.4 plots the device length as a function of *SSF* for different values of *NoS* ranging from 1 to 15. This plot shows an interesting behavior of *SSF*, with a minimum around *SSF*=1.4 and no increase in *L* for *NoS* greater than ~5. The behavior from Fig. 6.3 and 6.4 are further clarified by the 3D plot in Fig. 6.5, which show *L* as a function of both *NoS* and *SSF*. Here, we can clearly see the valley of lowest *L* values and observe the tradeoff between *NoS* and *SSF*.

6.4.3 L vs SSF Relationship for Different NoS

An important design parameter not considered in Figs. 6.3 and 6.4 is the device resolution, D_{p_min}. Fig. 6.6 plots D_{p_min} (in log scale) as a function of *NoS* for various values of *SFF* ranging from 1.5 to 3.4. This plot helps to determine which values of *NoS* and *SSF* can achieve the desired final particle size separation resolution. For example, very small values of *SSF* would be unable to achieve resolution less than 0.1µm. This helps to put some bounds on useful values of *NoS* and *SSF*. To better highlight this, D_{p_min} values of 0.01 µm, 0.1 µm, and 1 µm (error margin ± 15%) were extracted from data and added to the 3D plot in Fig. 6.5. This allows us to clearly see which values of *NoS* and *SSF* can achieve desired resolution.

6.5 Modeling Results and Analysis: Practical Limits

In practical implementations, multiple design parameters, add constraints to the device length. Here, we define them as secondary design considerations, which including fabrication limit, gamma variation, and pillar shape.

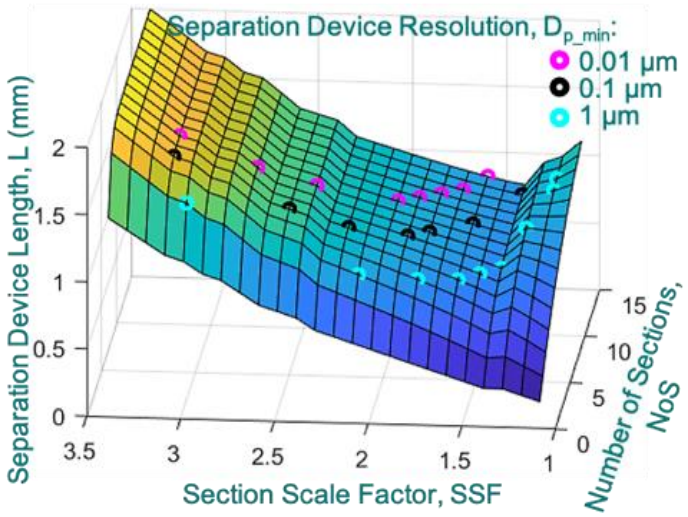

Figure 6.5. 3D plot of L as a function of both *SSF* and *NoS*. Colored dots show where various values of D_{p_min} can be achieved.

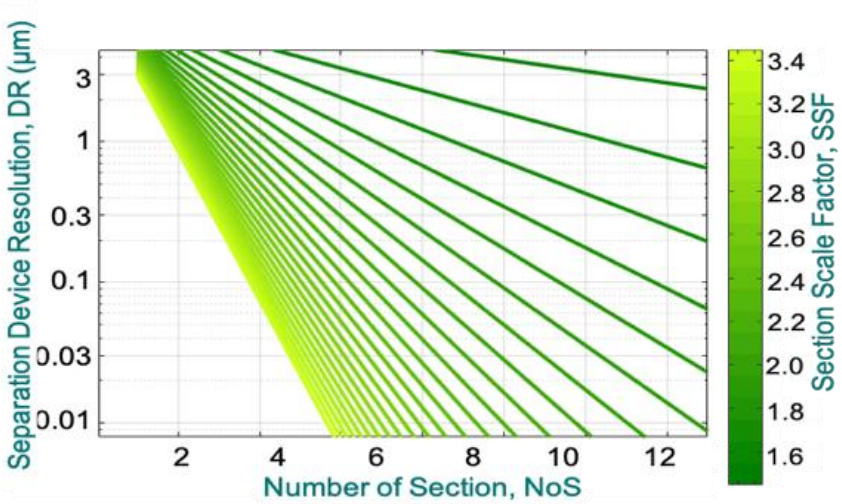

Figure 6.6. Theory analysis to study how section numbers (*NoS*) and section scale factor (*SSF*) affect the device resolution (D_{p_min}).

6.5.1 Fabrication Limits

Noticed, both pillar size and the gap between pillars will experience limits due to

resolutions in fabrication capability. A DLD device is typically fabricated using deep-RIE with traditional soft-lithography process [185]. Deep-RIE process, due to the side effect, will allow limited feature size for specific etching depth, which certainly restrict the gap/pillar ratio, γ_k. For example, if we design a 15um depth channel, side effect will determine the smallest γ_k we can get is about 0.2 ($w_k/(w_k+g_k)>0.2$). E-Beam lithography could provide higher resolution (sub-micron) but is not suitable for centimeter-sized devices. For some applications that do not require extremely high resolution, soft lithography or even 3D printing based DLD device with above 10 micro resolution also exist. To demonstrate the impact of fabrication limits on multi-size gap scaling, parameters, g_{k_fablim} and w_{k_fablim}, as a minimum feature size for the gap and the pillar size, were added to the model. The model was changed by adding equation (6.10) to disable scaling when pillar and gap sizes reach this limit. Moreover, as specified in section II, the actual size limits of pillars will also depend on the pillar shape [198], which will be presented in section 6.5.3.

$$g_k < g_{k\_fablim}, \text{ else, } g_k = g_{k\_fablim}$$

$$w_k < w_{k\_fablim}, \text{ else, } w_k = w_{k\_fablim} \quad (6.10)$$

Due to the fabrication condition limitation, different device fabrication facility may have different fabrication capability. In the simulations, the parameters g_{k_fablim} and w_{k_fablim} can be chosen by the DLD device designer. In our fabrication facilities (Lurie Nanofabrication Facility and W.M. Keck Microfabrication Facility), according to the MEMS process we choose, for circle shaped pillar design, both the smallest gap size and the smallest circle pillar size was set to 1 μm. Fig. 6.7(a) shows that the practical limits significantly change the relationship between *L* and *NoS* and *SSF* compared to Fig. 6.3. We no longer see *L* saturate for large values of *NoS*, and in fact *L* grows to 100s of meters for large *NoS* and *SSF*. Now, once section scaling reaches the fabrication limit, gap can no longer be scaled down and, according to (6.1), the number of

rows, *N*, grow increasingly larger with each subsequent section. Because *L* values in meters are impossibly large, the available design space is significantly constrained. To better show that the model predicts for reasonable values of *L*, as an example shown in Fig. 6.7(b), it can be noticed that 0.01 μm resolution is achieved around *L*=200 mm when we zoom in to specific D_{p_min} value. As an exceptional case, *NoS*=1 means design a single section device. Because it is not practical to design a single section device with the high dynamic range requirement, in this model, *NoS* ≥2.

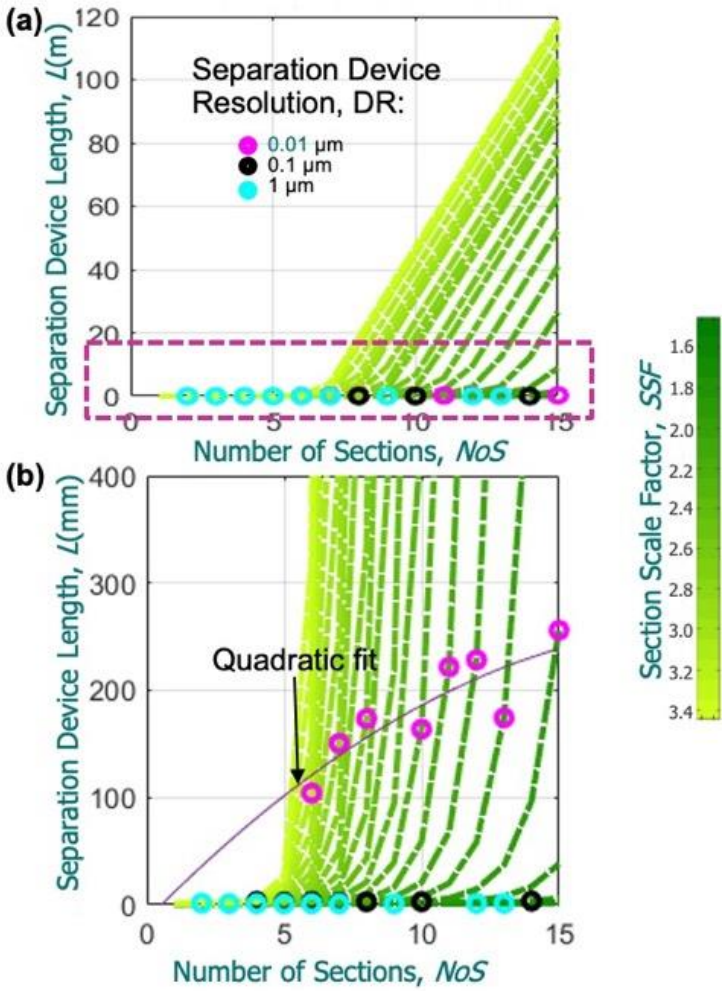

Figure 6.7. *L* as a function *NoS* and *SSF* after implementing practical fabrication limits for circle shaped pillars. Zoom in (b) help to illustrate the design space suitable for achieving 10 nm resolution, D_{p_min}.

6.5.2 Gamma Variation (γk)

To simplify studying the relationship among the critical design parameters of a multi-section cascade DLD device, in section 6.4, γ was set to a constant used across all sections. However, the value of γ strongly influence the device dimension. Thus, to reduce the total length of the device, considering fabrication limits, it is possible to vary the γ value used per section.

To investigate the optimal values of γ for each of the sections, a range of values from 0.3 to 3 were used by the model. For any given device resolution, D_{p_min}, fabrication limit parameters, and *NoS* of interest, the model returns the length of each section for each value of γ evaluated. In addition, D_{p_min} and *NoS,* and *SSF* can be calculated. For example, for applications such as size fractionation of PM samples, that require 0.01 μm particle separation resolution, if *NoS* is set as 10, it means the application require to collect 11 size fractions of particles with a dynamic range as large as 1000. Fig. 6.8 shows simulation results for this case, where the desire device resolution is of 0.01 μm and *NoS* is set to 10. Fig. 6.8(a) presents the section lengths in millimeters for different values of γ. To better appreciate the changes in section length that result from varying the values of γ, for each section, the lengths were normalized by dividing them by the section length resulted from the smallest γ. Results of the normalization are shown in Fig. 6.8(b). For the smallest length device purpose, the smallest length for each section, L_{k_min}, can be achieved by selecting the ideal γ_k value. In the case presented in Fig. 6.8, if $k > 2$, ideal γ_k is 1, while $k \leq 2$, ideal γ_k value will be less than 1.

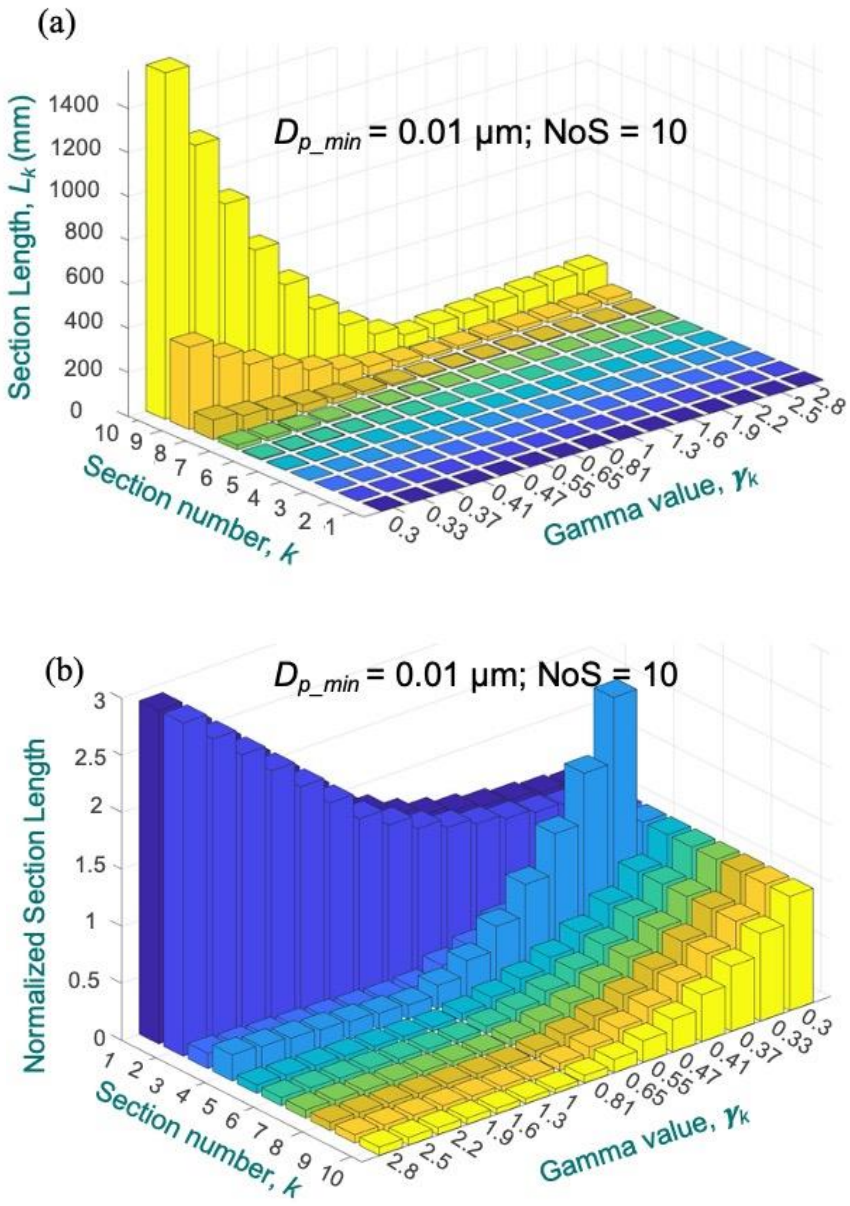

Figure 6.8. Real length of each section, L_k, (a), and normalized value, (b), as a function of γ_k with implementing practical fabrication limits for circle shaped pillars when require D_{p_min} is 10 nm and *NoS* is 10. (In order to show more features, Fig (a) was rotated 180°.)

Same analysis was also performed for application, such as blood separation to analyze all kinds of biological particles, that require 1 µm separation resolution with 11 size fractions. Fig. 6.9 shows simulation results for the case where the desire device resolution is of 1 µm and *NoS* is also set to 10. Fig. 6.9(a) presents the section lengths in millimeters for different values of γ, and Fig. 9(b) presents the same results but with normalized lengths. Here, the smallest device length, L_{k_min}, can be achieved by selecting the γ_k equal to 1 for $k > 6$ and γ_k less than 1 for k

≤ 6.

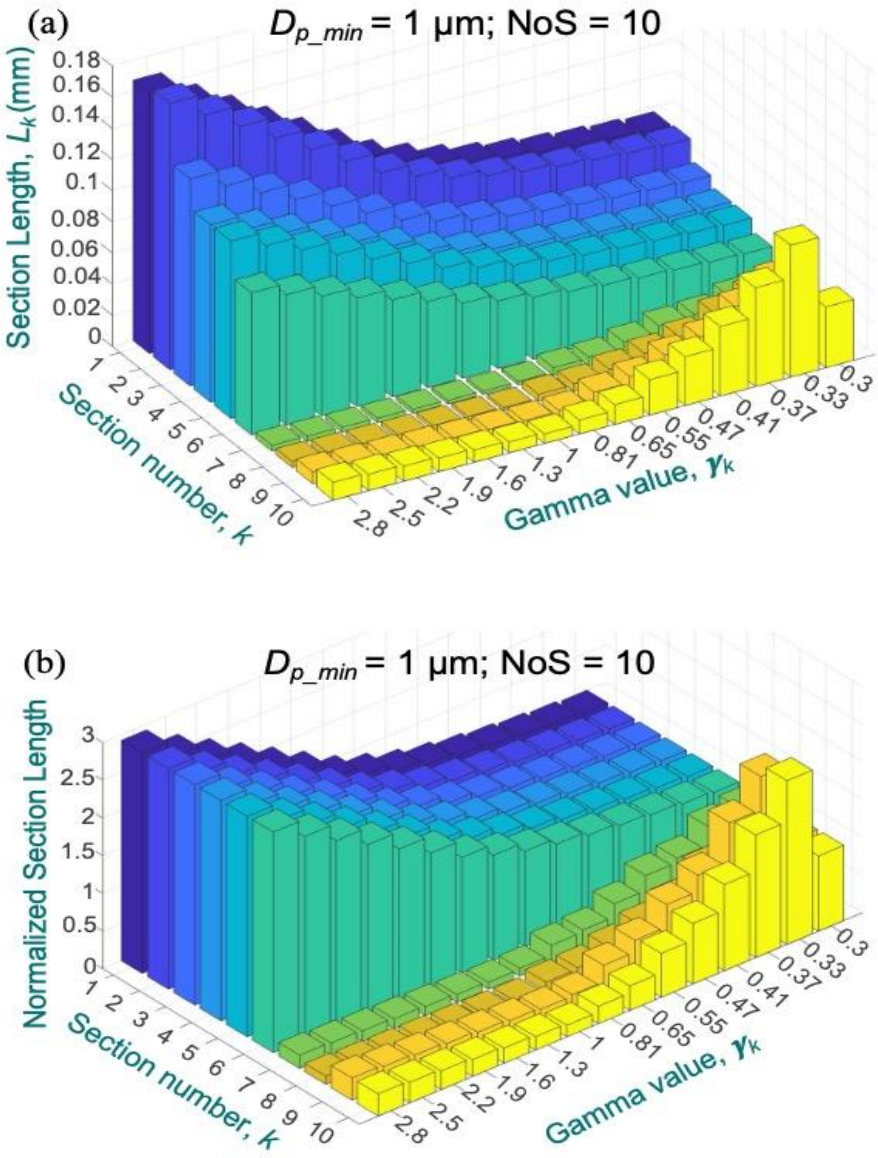

Figure 6.9. Real length of each section, L_k, (a), and normalized value, (b), as a function of γ_k with implementing practical fabrication limits for circle shaped pillars when require D_{p_min} is 1 µm and *NoS* is 10.

Because the optimal γ can vary depending on the number of sections, we set our model to look for the shortest device length when the optimal γ per section are selected for different values of NoS. Fig. 10 shows the results of the shortest device length by adding the shortest

section lengths together as a function of NoS. In general, it can be seen that by increasing the NoS, the total device length can be dramatically decreased. From the inset in Fig. 10(a), results show that increasing the device resolution, D_{p_min}, not necessary increase the device length, as long as the optimal γ is selected each section.

It is worth noticing that, in some cases, setting the same γ value for each section will not necessarily sacrifice the device dimension too much but will extremely simplify the design process. Fig. 10(b) present the ratio of device length when the shortest device length using optimal γ for each section, L, is divided by the shortest device length using the same γ for all sections, L'. The L/L' ratio can predict if it is worth to choose different γ values for different sections, which will increase the design complexity. For example, for the $D_{p\_min} = 0.01$ μm case, choosing optimal gamma for each section could reduce the total device length when NoS increase. However, when NoS is more than 5, as NoS increase, using optimal gamma per section do not reduce the total device length anymore. Since the design and fabrication complexity is increase dramatically, in this situation, it would be better choice to use the same gamma for all sections.

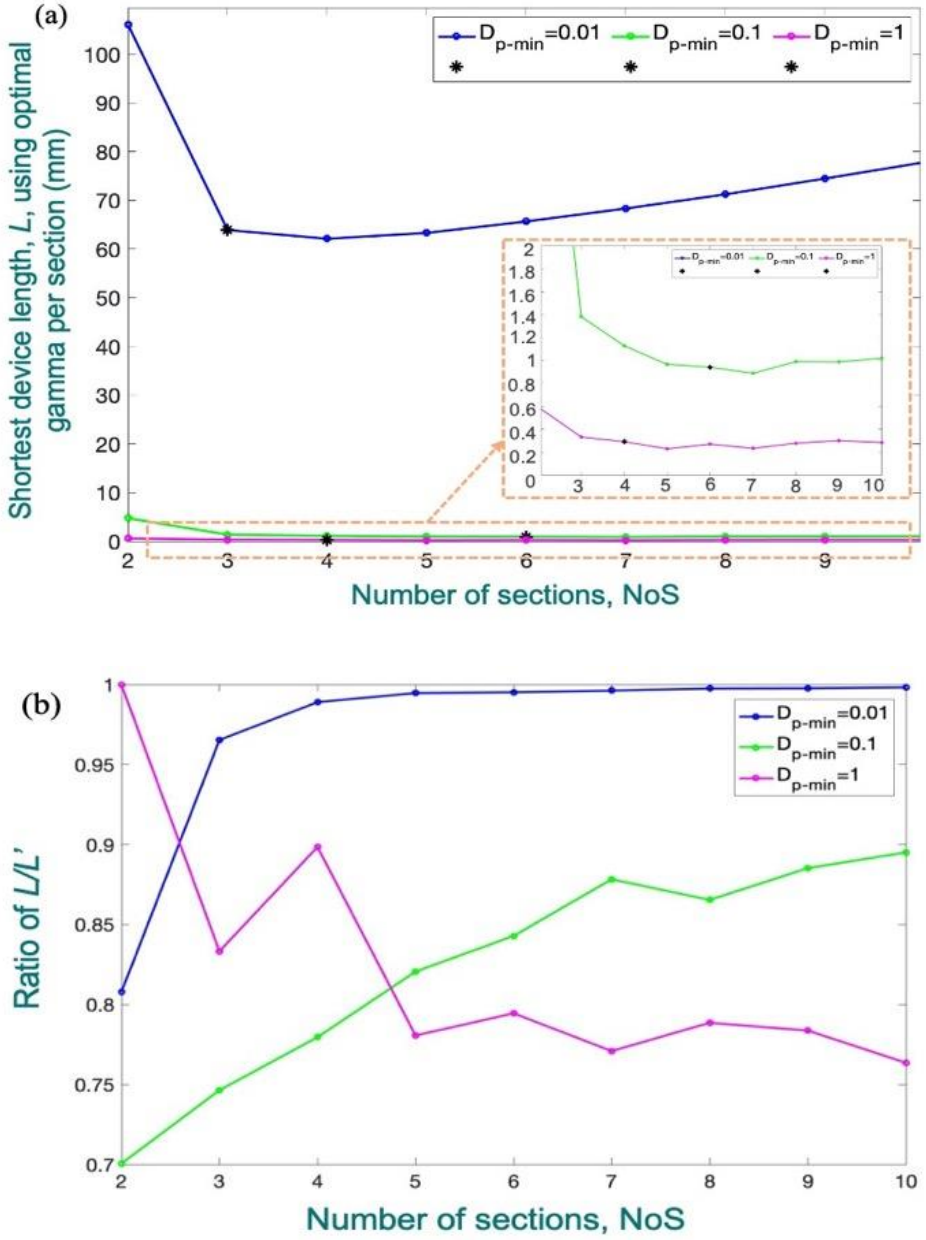

Figure 6.10. (a) Plots of *L vs NoS* for Circle-shaped pillars with fabrication limits. Different D_{p_min} values highlight important regions of consideration; (b) Plots of *L/L'* ratio vs *NoS*, where *L* is the shortest device length using optimal gamma per section, while *L'* is total length using same gamma for all sections.

6.5.3 Pillar Shape

Different pillar shape design, such as circle shape, triangular shape, T-shape, L-shape, I-shape and so on, haven been studied to show different advantage for specific application appeal [198][216]. Different shape designs require different smallest feature size fabrication capabilities. In our model, w_{k_fablim} was used to represent the pillar shape design and further

study how the shape design affects the total device length. In real applications, most particles have fortuitous shape, which can be categorized as non-spherical particles. I-shaped pillar can systematically enhance the separation efficiency for non-spherical particles. Moreover, in comparison to circle shape design, which is the most common pillar shape, I-shape design is a sophisticated design that restrict the fabrication capability much more due to the groove shape design. Here, I-shape is analyzed to show how pillar shape choice can also be included in the model.

For the I-shaped pillar DLD design, the model was altered to set the smallest pillar size to 6 μm and smallest pillar gap to 2 μm. Results for the shortest device length using optimal γ per section are shown in Fig. 6.11(a), where results of the *L/L'* ratio are shown in Fig. 6.11(b), predicting a similar regularity compare to circle shape results. From Fig. 6.11(a), it can be noticed that a 0.01μm resolution can be achieved around *L*=1500 mm in I-shape design, while circle shape design only requires ~100mm. In comparison to circle shape, the total DLD device length is about 15 times longer in I-shape design due to the smaller fabrication limit when D_{p_min} is chosen as 0.01 μm. This suggests 0.01μm resolution would be very difficult to achieve with I-shaped pillars, but 0.1μm resolution is achievable at ~14 mm using *NoS* = 5 and *SSF* around 2.6. In addition, as shown in the inset figure in Fig. 6.11(a), the total device length can be reduced dramatically if sacrifice the dynamic range. Interestingly, as shown in Fig. 6.11(b), choosing optimal γ_k value for each section in the I-shape design can always reduce the total device length. However, as the NoS increase, the gain is gradually decreased.

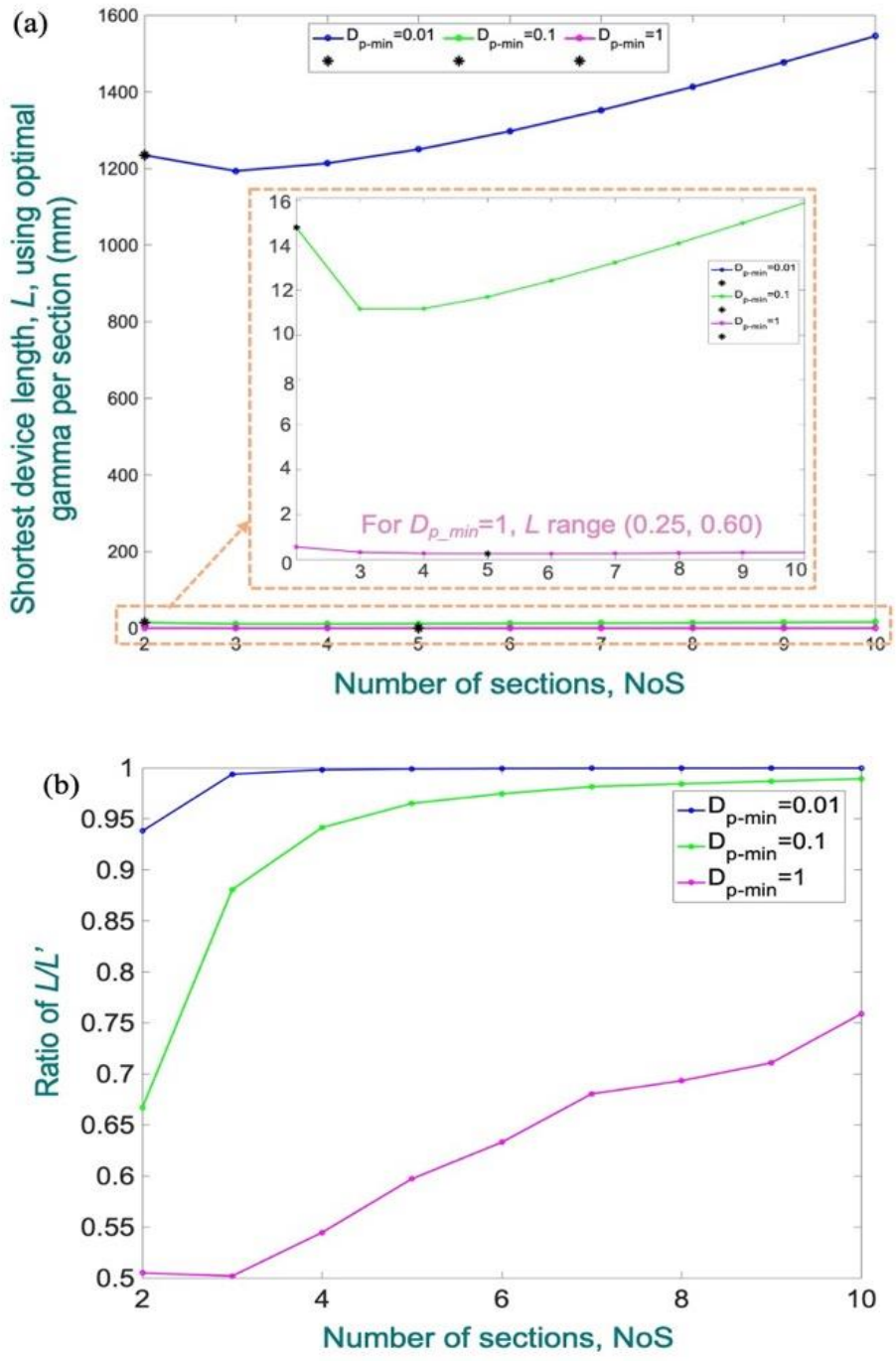

Figure 6.11. (a) Plots of *L vs NoS* for Circle-shaped pillars with fabrication limits; (b) Plots of *L/L'* ratio *vs NoS.*

6.6 Discussion and Case Studies

The mathematical model of the externally balanced cascade DLD can be utilized to predict the total device length based on the specific design parameters. In this section, three case studies are presented with the model. MATLAB code can be found from Appendix II.

6.6.1 Case 1

The first case is to design a one section I-shaped pillar based DLD device for an application that require 1000 as dynamic range and 0.01 μm as the D_{p_min}. This design represents the situation that we only need to collect particles that larger than 0.01 μm (up to 10 μm) and 0.01 μm particle into two different outputs. As calculated by the model, the total device length is around 60 m. Because a 60 m device length is impossible to fabricate, Case 1 demonstrates that it is not practical to achieve both high separation resolution (0.01 μm) and very wide dynamic range (1000) in only one section design. However, as Case 2 and Case 3 will show, the externally balanced cascade DLD concept introduced in this thesis can meet these goals.

6.6.2 Case 2

By cascading multi sections, a DLD device with wide dynamic range can be achieved within a practical length. Assuming 100 nm fabrication limits (such as EB lithography and Stepper lithography) can be realized, using circle shape design, biological particles separation (require D_{p_min} to be 1 μm) can be achieved by design the cascade DLD device as 5 sections with total pillar array length of ~0.3 mm; while the PM fractionation (require D_{p_min} to be 0.01 μm) can be achieved by the design of 4 sections of cascaded DLD device with a total pillar array length of ~41mm. The results show that, to expand the dynamic range, the externally balanced cascade DLD design provide a solution without increase the device length to an impractical size.

6.6.3 Case 3

High resolution fabrication process not only increase the burden to the cost of the process but also increase fabrication complexity. For some applications, such as the mineral processing industry, 1 μm separation resolution is good enough, fabrication method such as 3D-printing or purely PDMS based soft-lithography process with 10 μm fabrication limits can be utilized. In this case, polymer or soft material can be chosen to fabricate the DLD device instead of silicon wafer. Because the total device length restriction is more tolerated, centimeter scale is not necessarily the biggest available device dimension. Designer can simply choose suitable NoS, SSF, and same value for each section to achieve the design goal with less design complexity. For example, for application that require particles to be separated into 5 size bins while D_{p_min} = 1 μm and dynamic range is 100, the DLD device can be design use same gamma for all 5 sections and the total device length is ~8mm.

Table 6.2. Comparison for Different Case Study.

Cases		**DLD device length**
Case 1: I-shape pillar (one section design); g_{k_fablim} = 2 μm; w_{k_fablim} 6 μm;	D_{p_min} = 0.01 μm; D_{p_max} = 10 μm	L = 60 m Dynamic range =1000
Case 2: Circle-shape pillar (cascade design); g_{k_fablim} = w_{k_fablim} = 0.1 μm;	D_{p_min} = 1 μm; D_{p_max} = 10 μm;	L ~ 0.3 mm Dynamic range =10
	D_{p_min} = 0.01 μm; D_{p_max} = 10 μm;	L ~ 41 mm Dynamic range =1000
Case 3: Circle-shape pillar (cascade design); g_{k_fablim} = w_{k_fablim} = 10 μm;	D_{p_min} = 1 μm; D_{p_max} = 100 μm;	L ~ 8 mm Dynamic range =100

6.6.4 Conclusion

In this chapter, we firstly introduced a new approach for multi-size DLD separation using gap-scaled cascaded sections and defined a detailed model of design parameter interactions. Simulations of the model show informative relationships between design variables that aid in

making design tradeoff choices. Applying practical fabrication size limits significantly impact simulation results of device lengths and narrow down the design space. Results for circle and I-shaper pillars highlight design choices that enable achieving desired separation size resolutions.

7 Internally Balanced Cascade DLD for a PM Monitoring Microsystem

7.1 Motivation

The act of cascading DLD devices allows biological and airborne particles to be fractionated across many different sizes. The externally balanced cascade DLD approach introduced in Chapter 6 provides a solution to achieve both high separation resolution (e.g., 0.01 μm) and very wide dynamic range (e.g., 1000). However, because each section needs its own fluid input and output as well as tubing and pump for real implementation, the system complexity and size will be limited its potential to be miniaturized for a wearable PM monitoring microsystem. Noticed the outer diameter of commercially available tubing (e.g., in the smallest ELVEFLOW tubing, inner diameter is 1/64-inch, outer diameter is 1/32-inch) that serve as the input or output in a microfluidic device is typically larger than several hundred micrometers, the un-avoid multiple inputs and outputs limit our ability to short the total device length. In addition, in order to balance the hydraulic resistance, commercial valves are required to ensure its success in multi-size particle separation, which also add extra burden to the power consumption and cost of the system. To better extend the dynamic range of multi-size cascade DLD while make the device highly integrated for real-world PM monitoring, a monolithic design that are capable to solve these practical implementation challenges would be the highly preferred choice.

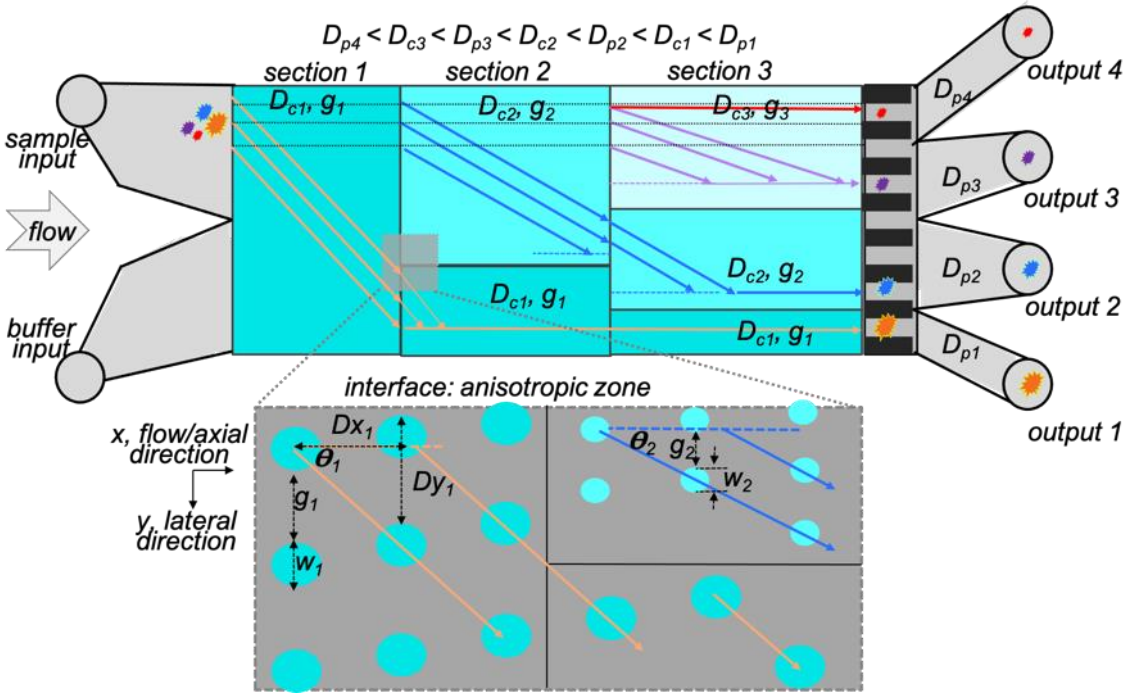

Figure 7.1. Concept diagram for internally balanced cascade DLD approach for multi-size separator with cascaded gap-scaled sections. (Note: section lengths are not to scale).

7.2 Internally Balanced Cascade DLD Approach

In order to fractionize particles into many sizes, gap scaling design that allow a practically implementable device length is the first step. Differing from the externally balanced cascade DLD approach, assembling multiple sections inside single microchannel meet the monolithic requirement. This monolithic scheme will avoid the extra inputs and outputs and also minimize the device fabrication effort. As shown in Fig 7.1, an internally balanced cascade DLD design, which cascades DLD sections by arrange pillar arrays with different gap parallelly, can achieve the monolithic design upshot. The first section consists of an array with single size, with gap/pillar size as g_1/w_1 for a critical size of D_{c1}, is designed to displace the largest particle to the right side. Following that, Section 2 consists of two regions, top region and bottom region, parallel to each other. While bottom region uses the same parameter in Section 1 to avoid particle clogging, in the top region, gap/pillar ratio is set as g_2/w_2 for a critical size of D_{c2}, to displace particles larger than D_{c2} but smaller than D_{c1}. Then, in Section 3, there are 3 regions,

each has different gap/pillar ratio parameter, which are parallelly arranged from top to bottom with progressively increased critical diameter. Through cautiously cascade sections design following this rule, the internally balanced cascade DLD approach can achieve a monolithic multi-size DLD separation with wide dynamic range. For example, in PM monitoring application, in order to perform size fractionation of particles, a five-section design utilize the design parameters listed in Table 7.1 can separate PM particles, from PM10 to UFP, into six size bins.

Table 7.1. A five-section internally cascade DLD design for PM size fractionation from micro- to nano- meter.

Sections	**Dc (μm)**	**g/w (μm/μm)**	**θ (degree)**	**N (rows per column shift)**
1	2.5	10/10	1.582°	~40
2	1	4/4 or 4/8	1.582°	~40
3	0.5	2/3 or 2/6	1.582°	~40
4	0.2	1/2 or 1/4	0.994°	~60
5	0.1	1/1 or 1/2	0.235°	~250

Note: N, rows per column shift, means this design parameter only allow one column displacement. Because the width of one column is smaller than 10 μm which is not wide enough to collect particles into different size bins, in real implementation, a parameter m, explained in Chapter 6, is required to be added.

As discussed above, choosing the gap/pillar ratio following the gradually scaling rule is only the first step. Mixed motion for smaller particles brought by so-called “array-induced anisotropy” was reported to possibly impede the separation efficiency [211], [217]–[222]. Anisotropic permeability, which is tendency of an array to induce a pressure gradient along the lateral direction, has been used to describe this anisotropic effect [211]. Variety of design and experimental factors can induce the non-zero average lateral anisotropic pressure, which could cause a flow shift in the flow direction thus affect particle trajectories. For example, as shown in Fig. 7.1, unsymmetric Dx/Dy (Dx, Dy is the pillar center-to-center distance in flow, lateral direction) design could introduce anisotropic effect. Dx/Dy≥1 was reported to be preferred a design with less anisotropic effect [215], [223]. Moreover, because Dy (lateral gap) is fixed by

the required Dc size, larger Dx could reduce the total hydraulic resistance as well. In this work, take Section 2 as an example, Dx_2 for small lateral gap (e.g., g_2) region will be design as same size as the large lateral gap (e.g., g_1) region, meaning $Dx_2=Dx_1$.

In addition to the Dx/Dy consideration, in order to make the internally balanced cascade multi-section DLD design fully functionally, three key factors need to be considered, including: 1) the gap size design along the boundary (wall edge of the channel); 2) hydraulic resistance balance when multiple lateral gap size exist; 3) design proper interface between sections. Because the flow pattern will be disrupted near boundaries as pillar array follow specific gradient, poor separation performance due to the anisotropic effect was reported to motivate the correcting of the gap along the edge, especially in narrow device [220], [222], [224]. Multiples groups have tried different boundary design strategies to minimize the variation of the cutoff diameter induced by boundary effects at the channel side walls, called the wall effect. In this work, one of the design strategies was applied to take care of edge correction, which will be described in Section 7.3. In laminar flow, flux will shift toward the big gap region which has a lower resistance compare to its adjacent small gap region. This flow shift due to the unbalanced hydraulic resistance will displace small particles even though their size is smaller than Dc, resulting a possible low separation efficiency. In Section 7.4, utilizing a circuit analogy and the finite element method (FEM) through COMSOL simulation, the hydraulic resistance balance approach and design will be presented. Third, through COMSOL simulation, studies for proper interface design along both flow direction and lateral direction to minimize the anisotropic effect will be presented in Section 7.5.

7.3 Boundary Design Strategy to Minimize Wall Effect

Both simulation analyses through finite element method and experimental verifications have been reported to shown appropriately boundary design can reduce the wall effect to avoid

unexpected particle trajectories that may compromise the separation efficiency [220], [222]. A gradient descent method similar to that used in machine learning to evolve the physical geometry for a target flow pattern was performed by Dr. Inglis's group, and a boundary design strategy, named as "Cube Root", that set the gap size along the wall following equation (7.1, 7.2) was reported to be able to achieve decent uniform critical particle size as [224]. In this work, as shown in Fig. 7.2, the Cube Root design strategy was utilized for all simulation models.

$$g_L = \mathrm{g}\left[-0.37\left(\frac{\mathrm{n}}{\mathrm{N}}\right)^2 + 1.08\frac{\mathrm{n}}{\mathrm{N}} + 0.3\right] \quad (7.1)$$

$$g_R = \mathrm{g}\left[-0.35\frac{\mathrm{n}}{\mathrm{N}} + 1.4\right], \text{ when } \left(\frac{\mathrm{n}}{\mathrm{N}} < 1\right)$$

$$g_R = 1.98\ \mathrm{g}, \text{ when } \left(\frac{\mathrm{n}}{\mathrm{N}} = 1\right) \quad (7.2)$$

where the g_L is the negative boundary (define as the wall that is away from the gradient) gap design, g_R is the positive boundary (define as the wall that the gradient is approaching) gap design, n is the nth number of row and N is the total number rows required for one column displacement. As shown in Fig. 7.2, take the first section in the internally cascade DLD design as an example, g_1 is 10 µm, in the second row of the positive boundary, the gap $g_{R(n=2)}$ was set as 13.9 µm instead of 10 µm, while in the negative boundary, the gap $g_{L(n=2)}$ was set as 3.3 µm. The computational fluid dynamic analysis, using COMSOL, represent a result matching with the literature that design the DLD device with edge correction can improve the performance near edges.

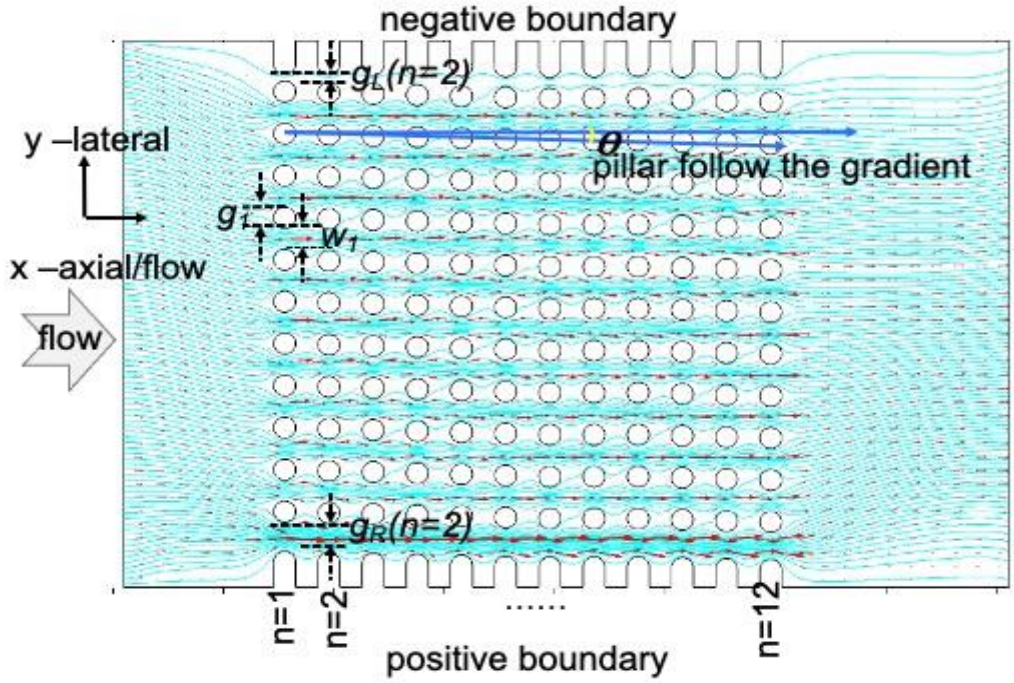

Figure 7.2. One model in CMOSL represent the "Cube Root" boundary design strategy implementation.

7.4 Hydraulic Resistance Balance

7.4.1 Fluid Mechanics

In fluid mechanics, assuming pressure gradient along the channel length is uniform, the Hagen-Poiseuille's law, developed from the Navier-Stokes equations with approximate and shown in equation (7.3), can be used to explain the hydraulic behavior of pressure driven flow (also termed as Poiseuille flow). With the equation, relation between pressure drop, fluidic resistances, and flow rate can be predicted.

$$\Delta p = Q \times R_h \tag{7.3}$$

where Δp is the pressure difference (in Pa) between input and output, Q is the volumetric flow rate (in m^3/s), and R_h is the hydraulic resistance of the channel. Reynolds numbers is conventionally defined as the ratio of inertial forces to viscous forces, shown in equation (7.4), which can be utilized to characterize the fluidic behavior in channels, such as laminar or

turbulent flow.

$$Re = \frac{inertial\ force}{viscous\ force} = \frac{\rho v D}{\eta} \qquad (7.4)$$

where ρ is the fluid density (in Kg/m^3), v is the characteristic velocity (in m/s), D is the characteristic length (in m), η is the fluid viscosity (in Pa·s). Laminar flow has a low Reynolds numbers (Re < ~1) in microchannel, meaning viscous forces are dominant. In a known Re microfluidic study, hydraulic resistance is normally constant for fixed fluidic and microchannel geometry. The hydraulic resistance for common channel design, such as rectangular and circular channel, is well studied. Viewing the space between pillar as a single microchannel, a DLD device can be seen as an array of multiple channels that parallelly connected. Beginning from the hydraulic resistance calculation equation for normal shape and amending by experiment measurement, a revised equation (7.5) have been used to calculate the hydraulic resistance for a DLD device [225].

$$R_h = \frac{12\eta l}{1-0.63(\frac{g}{h})} \times \frac{1}{h \times g^3}, \text{ when } h \geq g \qquad (7.5)$$

where h is the channel depth (in m), g is the gap between pillars, and the l is the length along the flow direction. In this work, l is approximate to be equal to w, the pillar diameter. In order to simplify the analysis, the depth of the DLD device, h, will be set as 11 μm, which is larger than the biggest particle size, 10 μm, to avoid clogging. As shown in Table 7.1, targeting PM size fractionation application with high dynamic range, the gap size in this work will always be smaller than the device depth. Different gap and pillar diameter will change the hydraulic resistance. If the hydraulic resistance of the flow paths across the lateral direction is not balanced, fluid moves to the low resistance region if no additional restricts exist [226]. Correctly designing the internally balanced cascade DLD requires understanding and

controlling the fluidic resistance of the structures and pressure drops that occurs in them.

7.4.2 Hydraulic Resistance Analysis Using Circuit Analogy

Correctly designing the internally balanced cascade DLD requires understanding and controlling the fluidic resistance of the structures and pressure drops that occurs in them. One well known method for understanding hydraulic resistance in microfluidics is hydraulic-electric circuit analogy [227]. For the hydraulic resistance balance analysis of DLD, which is a pressure-driven and flow-dependent microfluidic device, the application of circuit analogy methods to microfluidics is based on the analogous behavior of hydraulic and electric circuits. As shown in Fig. 7.3(a), because the Hagen-Poiseuille's law is directly corelated to the Ohm's law, it is intuitive to consider the fluidic flow as similar to the current flow of electricity. The pressure drops to drive the fluidic flow is correlated to voltage, the volumetric flow rate is correlated to current, and hydraulic resistance is correlated to electric resistance. Applying this microfluidic-circuit-analogy model, as an example, a 4 by 4 pillar array inside the Section 2 (shown in Fig. 7.1) can be analyzed as Fig. 7.3(b). The flow in this area will be branched into three flux, one follows the small gap (g2) path and another two follow the big gap (g1) paths, while the three paths parallel to each other. Because the fluidic flow studied in this work is in laminar flow region, the resistance along the lateral direction was ignored in the analysis. A circuit analogy model, shown in the right of the Fig. 7.3(b), can be utilized to predict the fluidic resistance and flow rate through microchannel. Calculating with equation (7.5), the hydraulic resistance in bottom path, R_{H2}, will be large than the hydraulic resistance in top two paths, R_{H1}, because g_2 is smaller than g_1. As a result, the volumetric flow rate of big gap region, Q_1, is larger than the volumetric flow rate of small gap region, Q_2, meaning a lateral flow is exist in Section 2 due to the flow shifting. The lateral flow will certainly affect the particle trajectory.

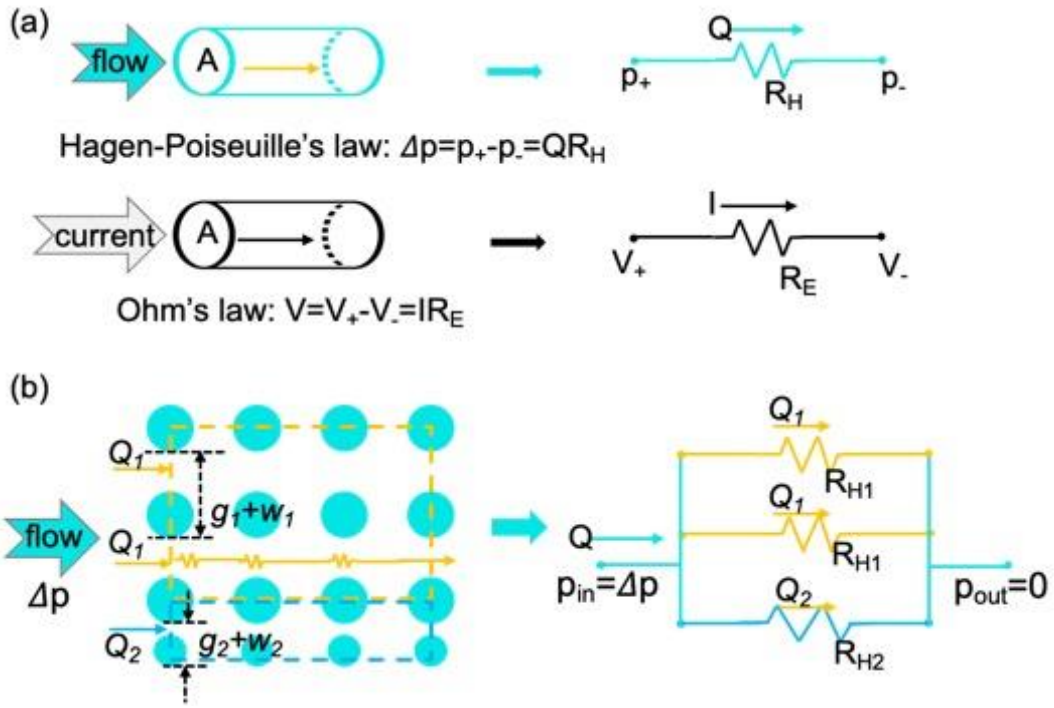

Figure 7.3. Physical correlations between the flow of a fluid and the flow of electricity: (a) Hagen-Poiseuille's law correlated to Ohm's law; (b) The application of hydraulic-electric circuit analogy in a 4 by 4 DLD pillar array.

7.4.3 Approach for Hydraulic Resistance Balance

One approach to address the uneven volumetric flow rate in Section 2 of the internally cascade DLD, specified in Section 7.4.4, is to implement two different input flow for two gap region separately [226]. However, this can only be implemented when there is only single section which allow the carefully controlled input to be applied to very beginning of the section 2 in the internally cascade DLD. In a multi-section cascade DLD, aiming to separate particles into multi size bins, this method cannot be practically implemented. A design that can balance the hydraulic resistance is required.

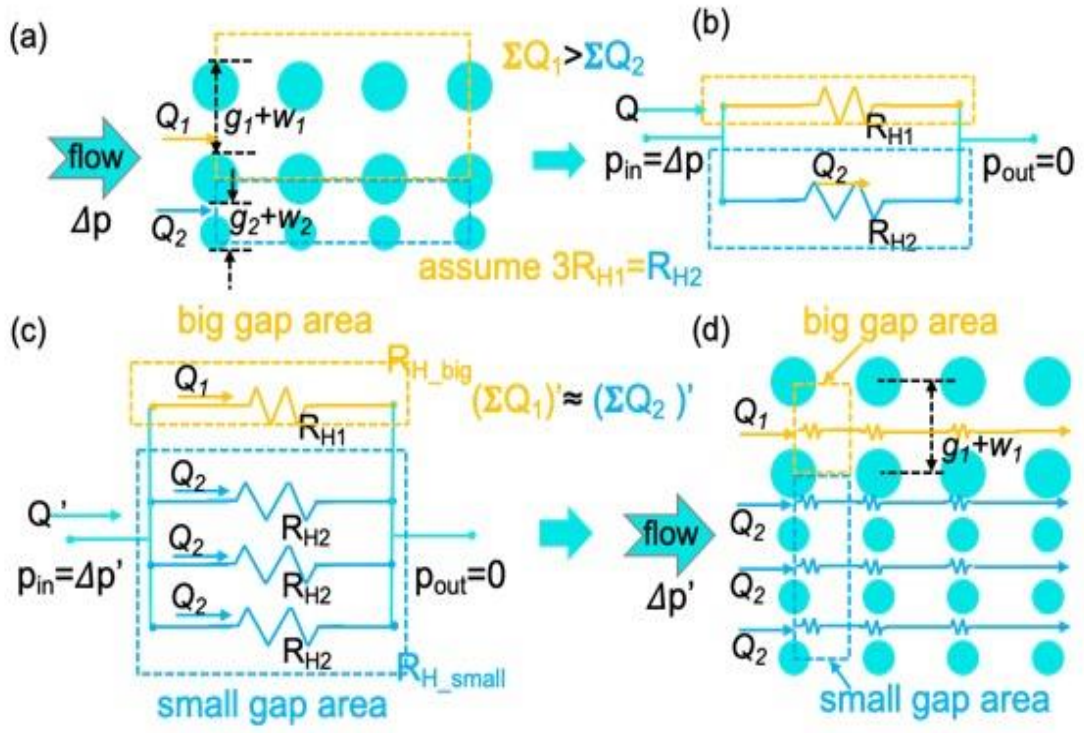

Figure 7.4. Hydraulic resistance balance uses the circuit analogy: (a, b) unbalanced 3 by 4 pillar array and its circuit analogy; (c, d) 5 by 4 balanced pillar array design and its circuit analogy.

Similar to the balance process in an electric circuit, another approach to balance the hydraulic resistance along the axial direction is to set up suitable ratio to make the total resistance of the big gap region equal to the total resistance of the small gap region. Assume in Section 2 of the internally cascade DLD, the gap design ($g_1>g_2$) outcomes $3R_{H1}=R_{H2}$ when calculate use equation (7.5), as shown in Fig. 7.4(a, b). The goal to balance the hydraulic resistance thus can minimize the laminar flow is to make the total flow in big gap region equal to the total flow in small gap region, meaning $(\mathbf{\Sigma}Q_1)' \approx (\mathbf{\Sigma}Q_2)'$ as shown in Fig. 7.4(c, d). Utilizing the circuit analogy analysis, the hydraulic resistances across the lateral direction can be considered to be parallel resistances. Therefore, the total hydraulic resistance of the small gap region, R_{H_small}, can be calculated as $R_{H\_small}= R_{H2}||R_{H2}||R_{H2}= \frac{R_{H2}}{3}$, while the total hydraulic resistance of the big gap region, R_{H_big}, can be calculated as $R_{H\_big}= R_{H1}=\frac{R_{H2}}{3}$. Thus, $R_{H\_big}= R_{H\_small}$, which also means $(\mathbf{\Sigma}Q_1)' \approx (\mathbf{\Sigma}Q_2)'$. Ensuing this analysis, as shown in Fig. 7.4(d), a 5

by 4 pillar array that utilizing 1:3 as the ratio of number of columns for big gap to the number of columns for small gap can be designed to balance the hydraulic resistance of Section 2.

7.4.4 CFD Simulation of Hydraulic Resistance Balance

In order to find the right ratio to balance the hydraulic resistance, a group of computational fluidic dynamic (CFD) studies, varying ratio from 2:9 to 2:30, was performed with COMSOL. Because the angle of the gradient in the internally cascade DLD design is less than 2°, to simplify the model building in COMSOL simulation, non-gradient pillar array, shown in Fig. 7.5(a), was used to find the right number of columns ratio to balance the hydraulic resistance. Parameters, including the fluid properties, input/output/wall condition, gap/pillar size, and mesh, that were used in the COMSOL simulation is listed in Table 7.2.

Table 7.2. Parameters utilized in the COMSOL simulation

fluid properties		from material
material (water)	dynamic viscosity	$8.9*10^{-4}$ (Pa·s)
	density	1000 (Kg/m3)
	temperature	293.15 (K)
wall condition		non-slip
input (normal inflow velocity)		0.001 (m/s)
output		suppress backflow
mesh		finer
big gap region (g1/w1)		10/10 (μm)
small gap region (g2/w2)		4/8 (μm)

As shown in Fig. 7.5(a), one example of Section 2 that choose 2:13 as the ratio was simulated. In Section 2, the hydraulic resistance is different for the small gap region and the big gap region. Because the fluidic flow shifting due to the unbalanced hydraulic resistance happens locally. So, after specific number of rows, the fluid will follow the laminar flow, as shown in the streamlines after 6 rows in Section 2. As analyzed in Section 7.4.3, in a perfectly

balanced design, volumetric flow rate in big gap is will be equal to that in small gap region. Because the depth for all model is same as 11 μm, as an approximate comparison, areal flow rate (m^2/s), which is calculated as the product of the peak velocity (shown in Fig. 7.5(b)) and the total gap width, is used to compare the hydraulic resistance balance results. Ratio of areal flow rate is then calculated by dividing the total areal flow rate in big gap region by the total areal flow rate in small gap region. As shown in Fig. 7.6, in an ideal balanced design, the areal flow rate should be 1, which match with the analysis utilizing the circuit analogy. Because the existing of the hydraulic resistance, the simulation results conclude that a ratio range ~2:13-15 can be set to balance the second section of the internally cascade DLD. Notice the data of the 2:30 ratio design present that more flow follows the small gap region. This is because extra columns of small gap region which is not belong to hydraulic resistance balanced zone was included. Because the anisotropic effect is a local effect in laminar flow, which means beyond the “anisotropic zone”, fluid will follow the laminar flow without shifting. So, when extra columns with same gap size were added, the DLD will still be balanced, which is similar to add parallel resistance to a balanced circuit. When using different ratio to balance, the streamlines presented in the simulation results clearly show us there is still an "anisotropic zone" exist although a suitable ratio was implemented to balance the hydraulic resistance.

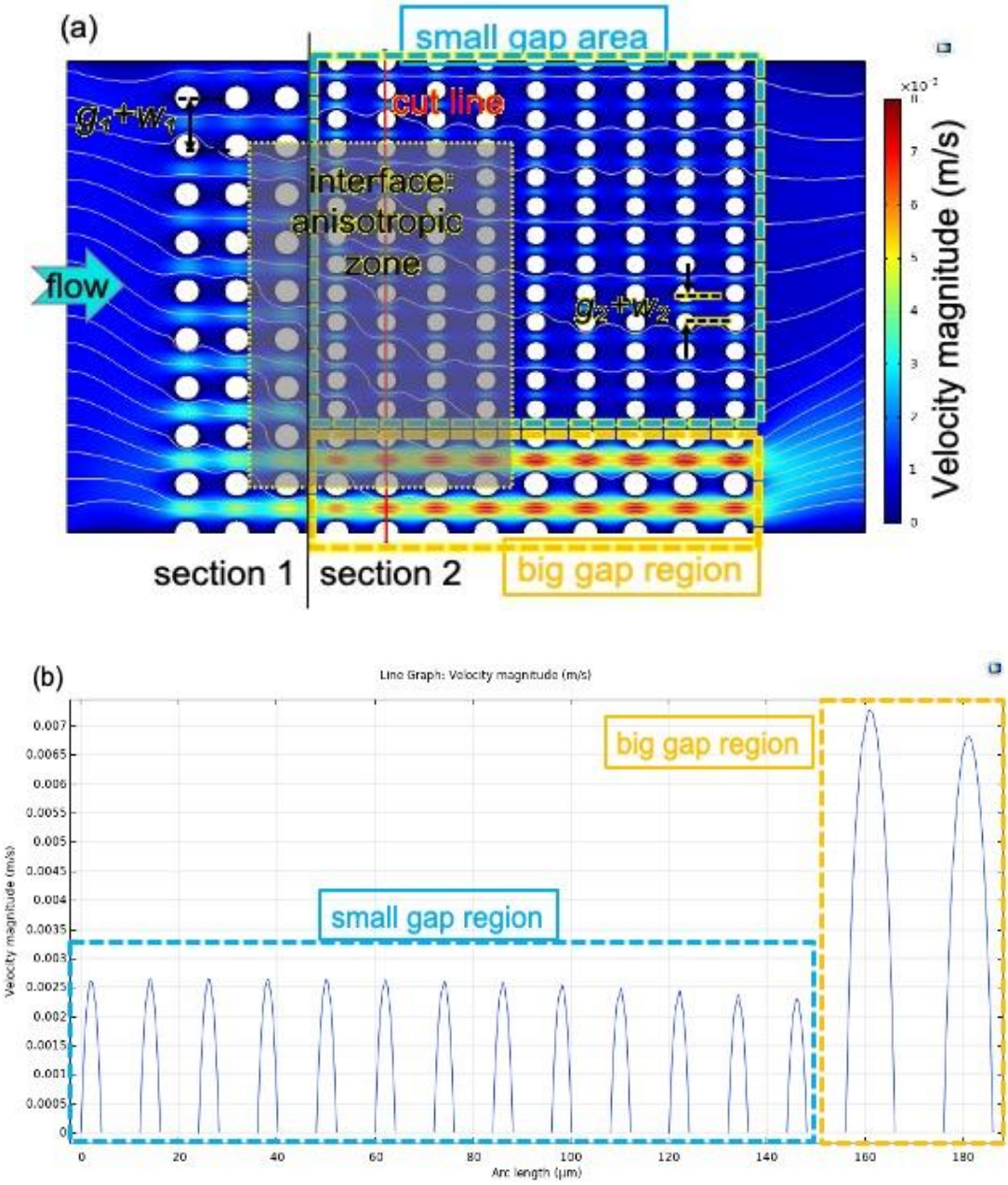

Figure 7.5. (a). COMSOL simulation results of a design that utilize 2:13 ratio to balance the hydraulic resistance in Section 2; (b) the flow velocity across the cut line defined in (a).

To achieve multi-size separation without sacrifice the separation efficiency, the way to implement this hydraulic resistance balance in real cascade DLD device is to make sure: 1) in the anisotropic zone, there are enough columns for small gap region to be set for hydraulic resistance balance; 2) in previous section, the big particle was displaced adequate columns to avoiding small particle get into this anisotropic zone. Notice if the streamline shifting is prominent in hydraulic resistance balance, the small particles are very likely to be displaced

which may not be able to be separated. Moreover, if the number of columns required for hydraulic resistance is large, the previous section could be extremely long because the large particle need to be displaced the required column to avoid particle clogging. Considerations to take care of this issue by design a proper interface will be presented in Section 7.5.

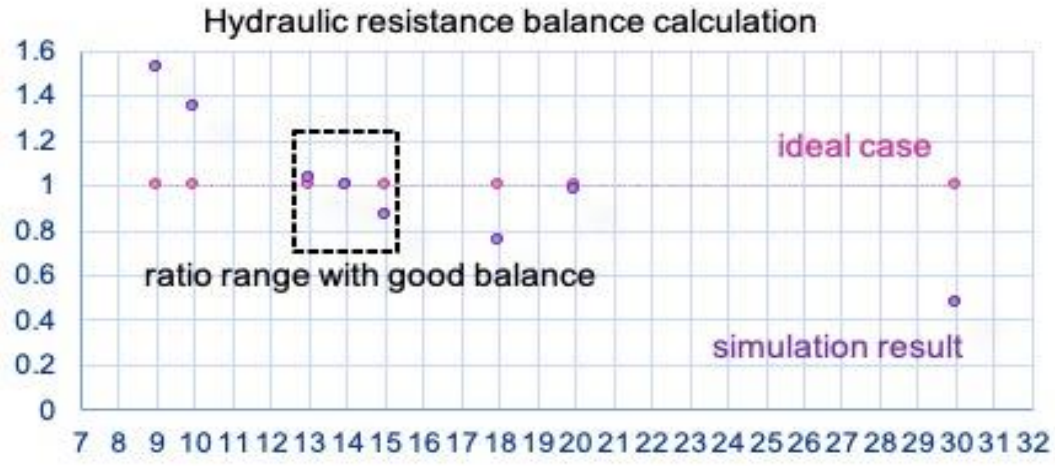

Figure 7.6. Calculation with the flow velocity simulation result to show the range of the ratio that will balance the hydraulic resistance in Section 2 of the internally cascade DLD.

7.5 Section Interface Design

Notice the two-gap design chosen in prior study set the two-gap size as 10 and 4 according to a calculation. As shown in Fig. 7.5(a), there are still ~5 rows belong to the anisotropic zone. Following the laminar streamlines, small particles, which are not supposed to be displaced, will be shifted 1 or 2 columns toward the bottom when get into this zone. Although adding several rows won't add too much burden to the total device dimension, possible unexpected particle displacement can decrease the separation efficiency, especially when particle size is down to nanometer. Several designs were studied to minimize the anisotropic zone, including both consideration along the flow direction and the consideration along the lateral direction. In this section, boundary consideration and pillar gradient will be implemented into the geometry design. Column of small gap to column of big gap ratio is set to be larger than 15:2 to balance

the hydraulic resistance. A block of pillar array with a total area as 920*410 μm^2 was utilized to perform the COMSOL simulation.

7.5.1 Design Along the Flow Direction to Minimize the Anisotropic Zone

As shown in Fig. 7.7(a), adding long wall in the transition space to direct particle manually was firstly simulated. Although this long wall design will prevent small particles to be displaced toward the positive boundary, simulation result shows shifted streamlines still across ~10 rows at both the end of Section1 and at the beginning of Section 2. Notice the streamline titling is extremely obvious in the anisotropic zone, which is serve as the interface to balance the hydraulic resistance. Compare to a design without transition, the long wall does not minimize the flow shifting apparently. The pressure result shown in figure also verify that the long wall design does not reduce the lateral pressure difference, which is ~45 Pa.

Then, a no-pillar transition design, shown in Fig. 7.7(b), was also studied. In this design, the no-pillar transition region serves as a flux buffer. Because there is no pillar inside this region, the flow at the end of this transition section which will enter the Section 2 will follow back to laminar flow. With this flux buffer which has a flow reset function, the flows entering section 2 will perform like the input flow without shift. The simulation results show that, before and after the transition region, the streamline shift was significantly abridged. The biggest lateral pressure variation along the lateral direction, ~34 Pa, also verifies this analysis. However, the streamline distribution in the transition region shows an abrupt shift which will certainly displace small particles thus reduce the separation efficiency.

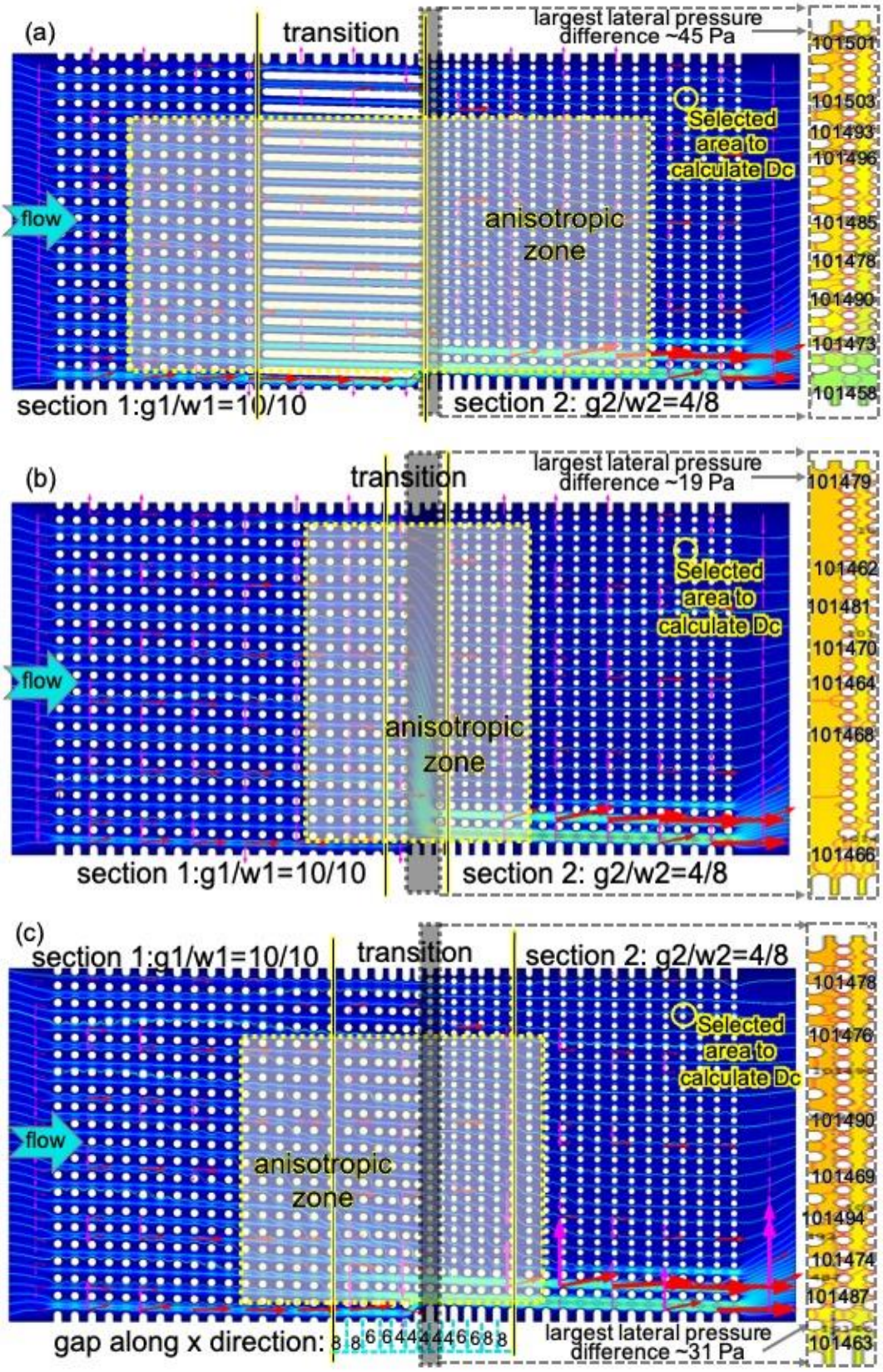

Figure 7.7. (a) Long wall design in the transition serve as a particle direct path; (b) No-pillar interface design serve as flux buffer; (c) Wave transition design, gradually reduce D_{x1} then gradually increase the D_{x2} in the transition region.

As reported, the long wall design and the no-pillar transition design acts as an anisotropic flow shift enablers [211], that allowing the flow to locally recompense for the lateral flow shift. In order to avoid the enabler and minimize the anisotropic zone, a wave transition design was also studied as shown in Fig. 7.7(c), in which the flow direction gap was gradually reduce when approaching Section 2 and then gradually increased back to 10 μm. This wave transition design is to minimize the gap differences between adject pillars to reduce the anisotropic effect. Simulation results show that smaller lateral pressure variation, ~31 Pa, was achieved. Compare to the long wall design, the wave transition design also slightly reduces the number of rows that the streamline will be shifted. As a summary, although the wave transition design does not show better streamline shift correction in Section 2 when compare to no-pillar design, the least lateral pressure variation suggests it's the best option.

7.5.2 Design Approach Along the Lateral Direction to Minimize the Anisotropic Zone

In the flow direction, a wave transition design could play a role to reduce the anisotropic effect. However, because the lateral gap variation is another determination factor of the anisotropic effect, further study along the lateral direction is require. In order to further reduce the anisotropic effect due to the gap different in the interface, a 2-section design, which set g1 as 10 μm while set g2 as 4 μm, 6 μm and 8 μm, was studied. As shown in Fig. 7.8, the case that set g1-w1-g2-w2 as 10-10-8-8 shows a significantly improvement compare to the case shown in Fig. 7.7(c). By adding a 1-2-1 transition section, only ~6 columns show slight streamline shift. The lateral pressure variation result, ~8 Pa, also verify the significant improvement. As shown in the Figures, in the selected area (labeled as yellow circle), the width of the first streamline which is determined by tracing stall line was measured. Because to check D_c is assumed to be twice the width of the first streamline [209], the relative D_c was calculated to study the anisotropic effect. The calculated results show that, although Section 1-2-1 was added, Dc (~1.7 μm) is still slightly smaller than the designed value (2 μm). However, the 1-

2-1 transition section design has the smallest Dc variation. In real implementation of such an internally balanced cascade design for PM size fractionation, this Dc variation could be adjusted by tune the gap size slightly without expanding the total device length dramatically.

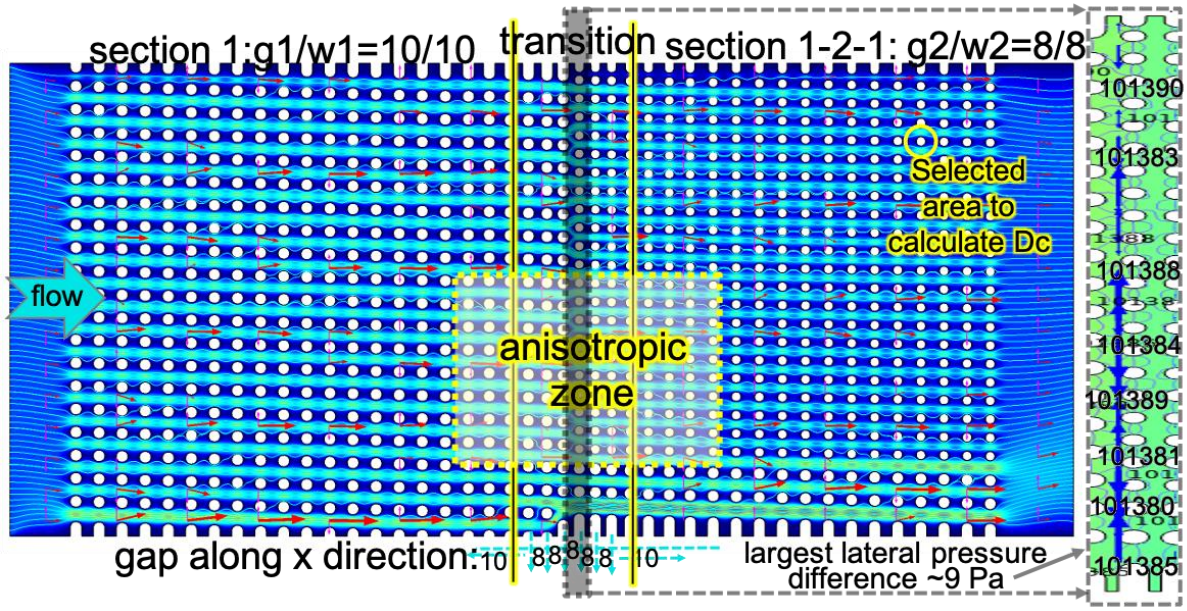

Figure 7.8. Add section 1-2-1 that has less lateral gap size difference. The transition between section 1 and interface section 1-2-1 utilizes the wave transition design.

As a summary of the 4 designs that have been studied, the comparison of the lateral pressure difference and the size of the anisotropic zone are listed Table 7.3. From the comparison, it is clear that the multi-step transition design (1-2-1 and 1-2-2) with wave transition along the flow direction shows the best performance, including less anisotropic effect and smaller required anisotropic zone.

Table 7.3. Comparison of different interface design options

Interface design	Largest lateral pressure difference	Anisotropic zone width (x direction)	Anisotropic zone width (y direction)
Long wall transition	~45 Pa	~420 μm	~260 μm
No-pillar transition	~19 Pa	~270 μm	~380 μm
Wave transition	~31 Pa	~460 μm	~200 μm
Transition section	~9 Pa	~190 μm	~80 μm

Note: In long wall transition, the space for the transition was not count for anisotropic zone because the particle in this region will not be displaced.

7.6 A Five Section Internally Balanced Cascade DLD Design for Coarse to Ultrafine PM Monitoring

The design goal of this internally balanced cascade DLD is to achieve high dynamic range (~1000, PM10 to UFP). Based on previous CFD analysis, transition sections 1-2-1, 1-2-2, and 2-1-3, were added following the multi-step transition method to reduce the gap variation thus reduce the anisotropic effect. A wave transition design will be implemented in all transitions. In addition, because the pillar array following different gradient in sections with multiple gap dimension, the pillar diameter of the two columns right in the interface where gap varied will also need to be adjusted accordingly. In this work, lateral directional pilar size of the two columns, one in the big gap region and one in the small gap region, will be designed to be slightly larger, which will form an ellipse pillar instead of circle pillar to keep the gap dimension consistent. Following the prior analysis and targeting the PM size fraction application, an internally balanced cascade DLD design that can separate PM particles (from PM10 to UFP) into five size bins is shown in Table 7.4.

Table 7.4. Internally balanced cascade DLD design to separate PM particles, from PM10 to UFP, into six size bins

Sections	Dc (μm)	g/w (μm/μm)	θ (degree)	N (rows per column shift)	Anisotropic zone (Z, μm)	Minimum section length (mm)
1	2.5	10/10	1.582°	~40	/	2.4
					72	
1-2-1	/	8/10	1.582°	/		3.2
					56	
1-2-2	/	6/8	1.582°	/		3.2
					72	
2	1	4/8	1.582°	~40		1.6
					60	
2-1-3	/	3/7	1.582°	/		1.6
					64	
3	0.5	2/6	1.582°	~40		1.6
					96	
4	0.2	1/5	0.994°	~60		5
					/	
5	0.1	1/2	0.235°	~250		

Note: Anisotropic zone spans two sections.

Ideally, in last two sections, Section 4 and 5, there is only one column of 10 μm gap is required to guide the largest particle without clogging the DLD device. Notice the gap size of the smallest gap region in Section 4 and 5 are the same, because we can design the gradient angle of Section 5 toward the top, Section 4 and 5 can be consider as one long section, Section 4&5. According to the hydraulic resistance balance analysis with the design parameters list in Table 7.4, the minimum number of columns required for different gap region in Section 4&5 will be 1 for 10 μm, ~2 for 8 μm, ~2 for 6 μm, ~3 for 4 μm, ~3 for 3 μm, ~4 for 2 μm and ~8 for 1 μm. When design each section, the number of columns of small gap region inside the anisotropic zone have to be equal or larger than the minimum number.

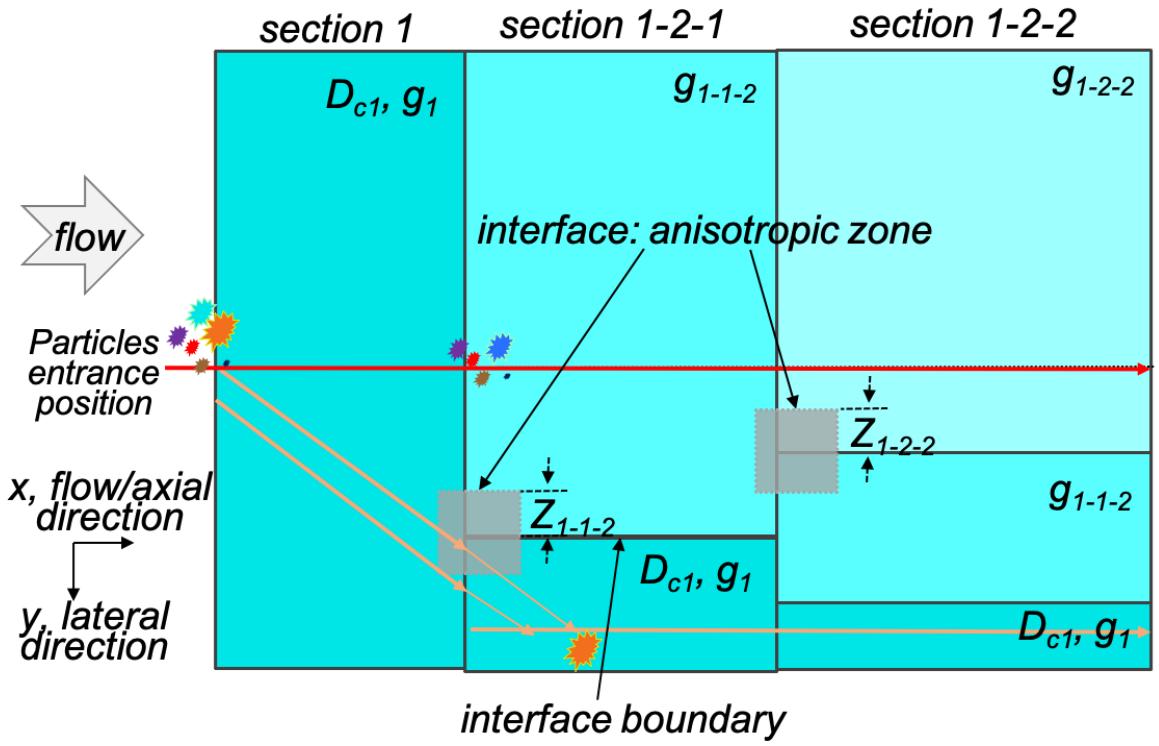

Figure 7.9. Illustration of interface (anisotropic zone) in previous 3 sections for a five section internally balanced cascade DLD design for coarse to ultrafine PM monitoring. (Note: section lengths are not to scale).

For real world PM monitoring, assume the particles that will be introduce from the input includes 9.5 μm (D_{p1}), 1.5 μm (D_{p2}), 0.8 μm (D_{p3}), 0.3 μm (D_{p4}), 0.15 μm (D_{p5}), and 0.01 μm (D_{p6}). Design from Section 1 assume the 9.5 μm particles were displaced 3 columns away from the entrance position, then in transition section 1-2-1, there have to be at least 2 columns (wider than $Z_{1\text{-}1\text{-}2}$ shown in Fig. 6.9) between the interface-boundary and the particle entrance position. Because D_{p5} particles will also be displaced in the transition section, we can design transition section by put the interface-boundary 2 columns away from the particle entrance position. Keep the same design strategy, in Section 4&5, the interface-boundary between 1 μm and 2 μm will be 8 columns away from the particle entrance position. As a summary, length of Section 1 will 2.4 mm; length of transition section 1-2-1 and 1-2-2 will be 3.2 mm; length of Section 2 will be 1.6 mm; length of transition section 2-1-3 will be 1.6 mm; length of Section 3 will be 1.6 mm; length of Section 4&5 will be 5 mm. As a total, the length of the internally balanced

cascade DLD is ~ 15.4 mm, which is shorter than the externally balanced DLD (~41 mm), as shown in Table 7.5. However, compared to externally balanced DLD device, due to the requirement of hydraulic resistance balance and the anisotropic effect zone, the width of the internally balanced DLD device will be much larger. For example, if we consider a lateral distance with 4 columns inside the channel is good enough to collect the particles in the output, the smallest device width is ~ 0.6 mm when introduce the mix of all particles from the middle of the first section. In addition to the device length improvement, the internally balanced DLD will also eliminate the extra resources, such as the extra fluid inlets/outlets and extra pumps and/or valve or additional fluidic segments that are required to balance the hydraulic resistance.

Table 7.5. Comparison between externally and internally balanced cascade DLD design to separate PM particles, from PM10 to UFP, into six size bins

Interface design	Minimum device length	Minimum device width	Fluid inlets/outlets	Required Pumps
Internally balanced cascade DLD	~15.4 mm	~0.6 mm	3/6	3
Externally balanced cascade DLD	~41 mm	~0.08 mm	10/10	6

Note: In each section, 4 column displacement for larger particles is chosen.

7.7 Discussion

DLD device with features of multi-size separation and high dynamic range is required to perform PM size fractionation, from PM10 (micrometer) to UFP (nanometer). The internally balanced cascade DLD design, employing the gap scaling multi-section approach, provides a monolithic solution. However, due to the gap different between adjacent region, the mix motion of small particle induced by the anisotropic effect could potentially decrease the separation efficiency. 2D/3D simulation through FEM method can help to identify promising device configurations and flow conditions. In this chapter, COMSOL simulation was performed to

guiding the design process for a functional internally balanced cascade DLD with proper interface design. Although a DLD device or a DLD section with an invariant critical size throughout is yet unknown, the studies presented in this Chapter could help to achieve that goal.

8 Summary, Contributions, and Future work

8.1 Summary

Exposure to air pollutants, both gaseous air pollutants and PM pollutants, is among the most human health threaten. This dissertation presents integrated microsystem technologies for continuous personal airborne pollutants exposure monitoring to address the spatiotemporal resolution challenges. To address such challenges, this dissertation seeks to develop a microfabricated room temperature ionic liquid gas sensor for gaseous air pollutants monitoring and a microfluidic system for PM monitoring, with the capability to provide high spatiotemporal resolution. A new microfabricated planar room temperature ionic liquid based (MPRE) gas sensor was developed to improve the reliability and repeatability; transient double potential amperometry method was developed to resolve the possible drift issue; and a sensor array consisting of multi MPRE gas sensors was developed to monitor multiple gaseous air pollutants. For PM pollutants monitoring, an autonomous PM monitoring system, consisting of PM trap, size fractionation, quantification, and classification, was developed. An ionic electret effect based electrochemical quantification with microfabricated planar electrodes and compact electronics was developed. Microfabricated deterministic lateral displacement (DLD) particle separation device was developed to perform size fractionation with critical diameter of 2.5 μm around 100% efficiency. Externally balanced cascade multi-section DLD approach was studied through a mathematic model with the goal of high dynamic range. In addition, interface design of the internally balanced cascade DLD design was studied through CFD analysis to provide a monolithic design that enable size fractionation with the features of high dynamic range and multi-size separation.

8.2 Contributions

This dissertation addresses multidisciplinary challenges in personal airborne pollutants

exposure monitoring by inventing new wearable sensor for gaseous air pollutants monitoring and new developed microsystem for PM pollutants monitoring. The significant contributions of this work include:

- *Developed a **new**, low cost, microfabricated electrochemical gas sensor with improved repeatability and long-term reliability that is well suited for personal multiple gaseous air pollutants monitoring.*

The ionic liquid (IL) gas sensing technology shows many promising features for wearable sensors in gaseous air pollutants exposure monitoring. In this work, the microfabricated planar room temperature ionic liquid based (MPRE) gas sensor array was developed through a newly invented microfabrication procedure. Rapid test through a new transient double potential amperometry method was explored to resolve the drift issue with reported 63.2% relative stand variation (RSD) compare to traditional constant potential amperometry. Multiple air pollutants, including methane, sulfur dioxide and ozone, were measured with the MPRE gas sensor with a sensitivity of 0.31 μA / [% methane], 0.13 μA/100 ppm, and 0.064 μA/100 ppm separately. Together with the CMOS circuitry, the MPRE gas sensor provides a promising platform toward a miniaturized, inexpensive, rapid-response, low power, multi-gas sensing array for point-of-exposure monitoring.

- *Developed the **first-ever** microfluidic PM analysis platform, enabling autonomous continuous real-time personal/wearable monitoring with the **unique** features of 1) quantification and 2) chemical classification, both across multiple PM sizes.*

Microfluidic microsystem provides a unique and beneficial combination of PM preconcentration and size-fractionated particle counting and component analysis to develop an easily used, wearable, real-time continuous PM monitoring system with high spatiotemporal resolution. In this work, to solve the spatiotemporal challenge of real-time continuous personal

PM exposure assessment, a microfluidic PM monitoring system consisting of capture, size fractionation, quantification and classification is developed. Approaches for each component of the aPM system were comparative analyzed; utilizing ESP based PM capture, DLD based size fractionation, electrochemical and capacitive quantification, as well as collision based electrochemical classification, this aPM system enabls the capability to perform quantification and component classification analysis across all/many PM size requirement.

- *Developed a **new method** for continuous PM quantification utilizing electrochemical ionic electret effect that is suitable for continuous fine PM measurement within a low power wearable platform.*

Electrochemical detection can offer accurate PM quantification as well as the potential for classification of chemical composition. In this work, the ionic electret effect-based electrochemical measurement of PM concentration was explored using different electrochemical methods and electrode materials, and differential pulse voltammetry (DPV) with gold electrodes was found to give the best sensitivity and repeatability. A compact electrochemical instrumentation system was implemented to demonstrate this detection scheme as a wearable PM monitoring platform. DPV results with polystyrene particles demonstrate a sensitivity of for 1 μm particles of 3 aA/particle. This work paves a path which leads the electrochemical measurement to wearable PM quantification.

- *Explored the externally balanced cascade multi-section deterministic lateral displacement approach through a **new** mathematic model analysis, predicting the trade-offs of design parameters and optimizing the device design to continuously separate PM across multiple size with high dynamic range.*

DLD microfluidic separator provides the capability to continuously separate particles with high separation efficiency and resolution, as well as being predictable and easy to operate. In

this work, an I-shape DLD device was microfabricated to achieve ~100% separation for fine PM. In order to fulfil the requirements of real-time continuous PM size fractionation, including both high dynamic range and the desire to separate particles into multi size bins, an externally balanced cascade multi-section DLD and an internally balanced cascade multi-section DLD were proposed. A mathematic model was built to aid the design for the externally balanced approach.

- *Explored the internally balanced cascade multi-section deterministic lateral displacement design through computational fluidic dynamic analysis and developed a* ***first-ever*** *multi-transition interface design, enabling a monolithic PM size fractionation across multiple sizes with high dynamic range.*

To better extend the dynamic range of multi-size cascade DLD while make the device highly integrated for real-world PM monitoring, a monolithic design that are capable to solve these practical implementation challenges would be the highly preferred choice. Computational fluid dynamic (CFD) simulation was performed to study the interface design for the internally balanced approach. This work provides a suitable approach for microfluidic size fractionation toward a wearable PM pollutants exposure monitoring system covering PM from PM10 to ultra-fine particle (UFP).

8.3 Future work

This work has established the foundation for a wearable gaseous air pollutant monitoring and a microfluidic PM air pollutants monitoring. The following suggestions are made for future work.

- *Integrated the MPRE gas sensor array with a multi-mode resource-sharing CMOS instrumentation circuit tailored to MPRE gas sensor through the lab-on-CMOS*

integration process

The selectivity of the MPRE gas sensor array rely on the fact that sensors which consist of the array have specific combination of design parameters, including electrochemical method, electrode and electrolyte material, when target for specific pollutants. In order to make the sensor array functional that each element can collect data simultaneously, design a multi-mode resource -sharing CMOS circuit tailored to the MPRE gas sensor array is critical. Lab-on-CMOS process which enable a monolithic design, can enhance the system miniaturization.

- *Developed the capacitively particle counter with single particle counting capability*

PM element or component information can be extremely complex, which could make the component classification a heavily data intense work. In addition to the quantification function, a capacitively particle counter with the single particle counting capability could serve as a forerunner for the component classification.

- *Implemented the externally and internally balanced cascade DLD device through microfabrication and microfluidic test*

The externally balanced and internally balanced cascade multi-section DLD approach as well as the design developed in this work build up the foundation of the PM size fractionation system that can separate particles into multiple size bins with high dynamic range. In future, the detailed device design with consideration of input and output, device fabrication, experimental setup, as well as the data analysis are required to implement the cascade multi-section DLD in real world application.

- *Study the alternative internally balanced cascade DLD designs regarding the design implementation*

The computational fluidic analysis of the internally balanced cascade multi-section DLD approach presented in this work build up the foundation of how to implement the internally

balanced cascade DLD in a monolithic PM size fractionation system. In future, regarding the real implementation, alternative designs, such as tilting the channel and add serpentine path in big gap area, that can simplify the device fabrication procedure and enhance the separation performance will be studied.

- *Develop the integration and miniaturization procedure to implement the aPM system with all four component, capture, size fractionation, quantification and classification*

Technologies for capture, size fractionation, quantitation, and classification were studied in this work. In order to develop the aPM system that can be widely distributed for real-time continuous air pollutants monitoring in real world, the integration procedure need to consider many elements, including but not only, device size, power consumption, cost, pump system that drive the fluid, as well as the liquid replacement and waster dispose need to be carefully studied.

APPENDICES

APPENDIX A: Fabrication flow recipes

A.1 MPRE gas sensor

1) Electrode fabrication:

a. Fix the PTFE with cleaned glass wafer.

b. Lithography

b.1 AZ4620 spring coating under 2100rpm.

b.2 Soft bake with hotplate under 95 degree for one minute.

b.3 Exposure ~ 45 s.

b.4 Post-bake with hotplate under 95 degree for one minute.

b.5 Develop with AZ400k for ~ 4 minutes and 30 seconds.

b.6 Check the patter under microscope before next step.

c. Thin film deposition: Deposit 10 nm/ 300 nm Ti/Pt with sputtering.

d. Lift-off: Soak the samples after thin film deposition into acetone for overnight. ~ 1minute ultrasonic treat can be added accordingly.

2) RTIL coating and assembling: Carefully drop several drops of RTIL on top of the fabricated electrode. Then assemble the sensor with O-ring and the 3D printed package.

A.2 DLD device

1) Microchannel etching:

a. Lithography for microchannel:

a.1 First coat the silicon wafer with HDMS and then spring coating SPR220 under 2000rpm with CEE 200X PR Spinner.

a.2 Soft bake with hotplate under 115 degree for 90 seconds.

a.3 Wait for more than 1 hour before exposure.

a.4 Exposure ~ 11 s.

a.5 Post-bake with hotplate under 115 degree for 90 seconds.

a.6 Develop with AZ726 60-60 double process under CEE Developer.

a.7 Check the patter under microscope before next step.

b. Deep-RIE: Use the 15 μm silicon etching recipe with the STS Pegasus 4.

c. Clean the etched silicon wafer: Use acetone and IPA to clean the etched silicon wafer.

2) Soft lithography for PDMS lid:

a. Lithography for SU8 mold:

b.1 SU8-2010 spring coating under 2100rpm.

b.2 Pre-bake with hotplate under 95 degree for two minutes.

b.3 Exposure ~ 14 s.

b.4 Post-bake with hotplate under 95 degree for two minutes.

b.5 Develop with SU8 developer for ~ 3 minutes.

b.6 Check the patter under microscope before next step.

b. PDMS preparation:

b.1 Label the petri dish for specific thickness.

b.2 Weight petri dish and then use “Zero” to eliminate the weight of the petri dish.

b.3 First, use clean pipette 1 to move 1.5 g curing agent into petri dish 1.

b.4 Second, use clean pipette 2 to add 15 g base into the same petri dish following the ratio of 1:10.

b.5 Use a third clean pipette to stir the mixed materials for ~ 5 minutes.

b/6 Pour the mixed material into a glass petri dish with the SU8 mold placed inside.

c. Degas and cut:

c.1 Put the glass petri dish, after mixed PDMS was poured into the petri dish, inside a vacuum chamber for overnight.

c.2 Put the glass petri dish inside oven with pump on at 100 degree for ~ 45 minutes.

3) Bonding:

a. Oxygen plasma treat both surfaces under 100 W for ~ 1 minute.

b. Quickly use the aligner to algin the silicon wafer with PDMS lid and push to bond them.

c. Treat the bonded device inside oven at 130 degree for one hour.

APPENDIX B: MATLAB Code for the Mathematic Model of the Externally Balanced Cascade Multi-size DLD

******Code for section 6.4******

******function******

```
function [L,Dcmin,pos_001, pA_001, pos_01, pA_01, pos_1, pA_1] =
DLD_theory(SSF_array,NoS_array,DR_array)
%Declaration of variables
%Section (Critical Dimension) Scale Factor, SSF [alpha], Dc(k)=SSF*Dc(k+1)
%Number of Section, NoS [k], i form 1 to NoS
%Separation Device Length, L
%Dc, DLD critical dimension
%Separation Device Resolution, DR (Dcmin) = f(SN,SSF)
%**************************Theory***********************************
%*****Fixed variables
gkg = 2;
lkg = 6;
gamma = lkg/gkg;
Beta = 1.1; % 10% more space based on the size of the particule
%initial condition for k=1
%Dc1=5;
g1=10*Beta;

%Values to be evaluated
alfa = SSF_array; %SSF
k = NoS_array; %NoS

%Total length of the device based on the previous declarated variables

for j=1:length(alfa)
   Dck = 10/alfa(j);
   gk = g1;
   for i=1:length(k)
      if i==1
         Nk(j,i) = (Dck(i)/(1.4*gk(i)))^(-1/0.48);
         Dcmin(j,i) = Dck(i);
      else
         Dck(i) = Dck(i-1)/alfa(j);
         gk(i) = Dck(i-1)*Beta;
         Nk(j,i) = (Dck(i)/(1.4*gk(i)))^(-1/0.48);
         Dcmin(j,i) = Dck(i);
      end
      %calculating length of each section
      yk(i) = ceil(Nk(j,i))*(gk(i)+(gk(i)*gamma));
      L(j,i) = sum(yk(1:i));
   end
   clear Dck gk yk
%    for i=1:length(k)
%       L(j,i) = sum(yk(1:i));
%    end
end

%Selection of DCmin values (name in the paper: DR)
```

```
DC_values = DR_array;
Z = size(Dcmin);
for i=1:length(DC_values)
   for j=1:Z(2)
      %for n=1:Z(2)
         temp = find(Dcmin(:,j)<(DC_values(i)+DC_values(i)*0.15) & Dcmin(:,j)>(DC_values(i)-
DC_values(i)*0.15));
         if isempty(temp)==1
            N_Dcmin(i,j) = 0;
         else
            N_Dcmin(i,j) = temp(1);
         end
      %end
   end
end

pos_001 = find(N_Dcmin(1,:) ~= 0);
pA_001 = N_Dcmin(1,pos_001);
pos_01 = find(N_Dcmin(2,:) ~= 0);
pA_01 = N_Dcmin(2,pos_01);
pos_1 = find(N_Dcmin(3,:) ~= 0);
pA_1 = N_Dcmin(3,pos_1);
%pos_001, pA_001, pos_01, pA_01, pos_1, pA_1
end
```

******script******

```
%Declaration of variables
%Section (Critical Dimension) Scale Factor, SSF [alpha], Dc(k)=SSF*Dc(k+1)
%Number of Section, NoS [k], i form 1 to NoS
%Separation Device Length, L
%Dc, DLD critical dimension
%Separation Device Resolution, DR (Dcmin) = f(SN,SSF)
%**************************Theory***********************************
clear all

%% Plot 1 of ISCAS paper; L vs K (1:30) for different alphas(1.5 - 3.4, 0.2 step) without Dcmin
clear all

SSF_array = 1.5:0.1:3.4; %alpha
NoS_array = 1:15; %k
DR_array = [0.01, 0.1, 1];

[L,Dcmin,pos_001, pA_001, pos_01, pA_01, pos_1, pA_1] = DLD_theory(SSF_array,NoS_array,DR_array);
L = L./1000; %to convert units from micrometers to milimeters

%Individual plot for L vs K for different alphas
figure;
CO(:,:,1) = ones(length(SSF_array)).*linspace(0,0.8,length(SSF_array)); % red
CO(:,:,2) = ones(length(SSF_array)).*linspace(0.5,1,length(SSF_array)); % green
CO(:,:,3) = ones(length(SSF_array)).*linspace(0,0.1,length(SSF_array)); % blue
plot(NoS_array,L(1,:),'LineWidth',3,'color',[CO(1,1,1) CO(1,1,2) CO(1,1,3)]);
%legend(strcat('alpha = ',num2str(alfa(1))))
for n=2:length(SSF_array)
   hold on;
   plot(NoS_array,L(n,:),'LineWidth',3,'color',[CO(1,n,1) CO(1,n,2) CO(1,n,3)]);
```

```
    %plot(NoS_array,L(n,:))%,'DisplayName',strcat('alpha = ',num2str(alfa(n))));
end
title('L vs NoS: Theoretical Analysis')
xlabel('Number of Sections, NoS')
ylabel('Separation Device Length, L (mm)') %\mum
grid on
ylim([0.2 2.2]);
figure;imagesc(SSF_array,SSF_array,CO)

%% Plot 2 of ISCAS paper; L vs alpha (1.1 - 3.4) for different NoS (1 - 10)
clear all

SSF_array = 1.1:0.1:3.4; %alpha
NoS_array = 1:15; %k
DR_array = [0.01, 0.1, 1];

[L,Dcmin,pos_001, pA_001, pos_01, pA_01, pos_1, pA_1] = DLD_theory(SSF_array,NoS_array,DR_array);
L = L./1000; %to convert units from micrometers to milimeters
Lt = L';
%Individual plot for L vs K for different alphas
figure;
CO(:,:,1) = ones(length(NoS_array)).*linspace(0,0,length(NoS_array)); % red
CO(:,:,2) = ones(length(NoS_array)).*linspace(0,0.3,length(NoS_array)); % green
CO(:,:,3) = ones(length(NoS_array)).*linspace(0,1,length(NoS_array)); % blue
plot(SSF_array,Lt(1,:),'LineWidth',3,'color',[CO(1,1,1) CO(1,1,2) CO(1,1,3)]);
%legend(strcat('alpha = ',num2str(alfa(1))))
for n=2:length(NoS_array)
    hold on;
    plot(SSF_array,Lt(n,:),'LineWidth',3,'color',[CO(1,n,1) CO(1,n,2) CO(1,n,3)]);
    %plot(NoS_array,L(n,:))%,'DisplayName',strcat('alpha = ',num2str(alfa(n))));
end
title('L vs SSF: Theoretical Analysis')
xlabel('Section Scale Factor, SSF')
ylabel('Separation Device Length, L (mm)') %\mum
grid on
ylim([0 2.2]);
figure;imagesc(NoS_array,NoS_array,CO)

%% Plot 3 of ISCAS paper; 3D plot - L vs NoS vs SSF (1.1 - 3.4) for different NoS (1 - 10)
clear all

SSF_array = 1.1:0.1:3.4; %alpha
NoS_array = 1:15; %k
DR_array = [0.01, 0.1, 1];

[L,Dcmin,pos_001, pA_001, pos_01, pA_01, pos_1, pA_1] = DLD_theory(SSF_array,NoS_array,DR_array);
L = L./1000; %to convert units from micrometers to milimeters
%pos_X is the position on k
%pA_X is the position of the alpha value
figure
surf(NoS_array,SSF_array,L)
xlabel('Number of Sections, NoS')
ylabel('Section Scale Factor, SSF')
zlabel('Separation Device Length, L (mm)') %\mum
hold on
for i=1:length(pos_001)
    hold on; plot3(pos_001(i),SSF_array(pA_001(i)),L(pA_001(i),pos_001(i)),'mo','LineWidth',2,'MarkerSize',5);
end
for i=1:length(pos_01)
```

```
   hold on; plot3(pos_01(i),SSF_array(pA_01(i)),L(pA_01(i),pos_01(i)),'ko','LineWidth',2,'MarkerSize',5);
end
for i=1:length(pos_1)
   hold on; plot3(pos_1(i),SSF_array(pA_1(i)),L(pA_1(i),pos_1(i)),'co','LineWidth',2,'MarkerSize',5);
end
hold off

%% Plot 4
clear all

SSF_array = 1.1:0.1:3.4; %alpha
NoS_array = 1:15; %k
DR_array = [0.01, 0.1, 1];

[L,Dcmin,pos_001, pA_001, pos_01, pA_01, pos_1, pA_1] = DLD_theory(SSF_array,NoS_array,DR_array);

% %***********No log scale
% figure;
% CO(:,:,1) = ones(length(SSF_array)).*linspace(0,0.8,length(SSF_array)); % red
linspace(0.5,1,length(SSF_array))
% CO(:,:,2) = ones(length(SSF_array)).*linspace(0.5,1,length(SSF_array)); % green
linspace(0,0.8,length(SSF_array))
% CO(:,:,3) = ones(length(SSF_array)).*linspace(0,0.1,length(SSF_array)); % blue
linspace(0,0.1,length(SSF_array))
% plot(NoS_array,Dcmin(1,:),'LineWidth',2,'color',[CO(1,1,1) CO(1,1,2) CO(1,1,3)]);
% for n=2:length(SSF_array)
%     hold on;
%     plot(NoS_array,Dcmin(n,:),'LineWidth',2,'color',[CO(1,n,1) CO(1,n,2) CO(1,n,3)]);
% end
% title('DR vs NoS: Theoretical Analysis')
% xlabel('Number of Sections, NoS')
% ylabel('Separation Device Resolution, DR (in \mum)')
% grid on
% figure;imagesc(SSF_array,SSF_array,CO)

%************Log scale
figure;
CO(:,:,1) = ones(length(SSF_array)).*linspace(0,0.8,length(SSF_array)); % red
CO(:,:,2) = ones(length(SSF_array)).*linspace(0.5,1,length(SSF_array)); % green
CO(:,:,3) = ones(length(SSF_array)).*linspace(0,0.1,length(SSF_array)); % blue
semilogy(NoS_array,Dcmin(1,:),'LineWidth',2,'color',[CO(1,1,1) CO(1,1,2) CO(1,1,3)]);
for n=2:length(SSF_array)
   hold on;
   semilogy(NoS_array,Dcmin(n,:),'LineWidth',2,'color',[CO(1,n,1) CO(1,n,2) CO(1,n,3)]);
end
title('DR vs NoS: Theoretical Analysis')
xlabel('Number of Sections, NoS')
ylabel('Separation Device Resolution, DR (in \mum)')
grid on
figure;imagesc(SSF_array,SSF_array,CO)

% %% Individual plot for L vs K for different alphas with Dcmin
% figure;
% plot(k,L(1,:),'k');
% for n=2:length(alfa)
%     hold on; plot(k,L(n,:),'k');
%     for i=1:length(pos_001)
%         hold on; plot(pos_001(i),L(pA_001(i),pos_001(i)),'bo','LineWidth',2,'MarkerSize',5);
%     end
```

```
%     for i=1:length(pos_01)
%         hold on; plot(pos_01(i),L(pA_01(i),pos_01(i)),'go','LineWidth',2,'MarkerSize',5);
%     end
%     for i=1:length(pos_1)
%         hold on; plot(pos_1(i),L(pA_1(i),pos_1(i)),'ro','LineWidth',2,'MarkerSize',5);
%     end
% end
% grid on;
% title('L vs K')
% xlabel('Number of sections, K')
% ylabel('Length of the device')
```

******Code for section 6.5******

******function******

```
function [yk,yk_normalized,gk,Dck,gamma] =
CP_DLD_gamma(Dp_min,Dp_max,gamma_min,gamma_step_less1,gk_fablim,D0k_fablim,NoS,gamma_max,
gamma_step_high1)
%UNTITLED2 Summary of this function goes here
%   CIRCLE PILLARS
%*****Defining gamma range based on gamma_lim and gamma_max (which is
%defined based on the fab limits)
%gamma_max = lkmin2/gkmin;
gamma = [1./((1/gamma_min):(-1*gamma_step_less1):1.1) 1:gamma_step_high1:gamma_max]; %change step
variable for gamma less than 1
%*****Fixed variables
syms x;
SSF = max(double(solve(x^NoS == Dp_max/Dp_min, x, 'Real', true)));
Beta = 1.1; % 10% more space based on the size of the particule
%*******Restrinctions of practical implementation - circle pillars
%gkmin = 1; %lkmin = gkmin*gamma;
%lkmin2 = 1; %this will be a limitation when gamma is less than one... need to check!
DcminR = 0.001;
gamma_fablim = D0k_fablim/gk_fablim;
%initial condition to k=1
g1=ceil(Dp_max*Beta);
gk(1:length(gamma),1) = g1;
Dck = Dp_max/SSF;
%loop variable
q=0;

for i=1:NoS
   for ga=1:length(gamma)
      lkmin = gk_fablim*gamma(ga);
      if (q==0)
        if i==1
            Nk(i) = (Dck(i)/(1.4*gk(ga,i)))^(-1/0.48);
            DRmin(i) = Dck(i);
         else
            Dck(i) = Dck(i-1)/SSF;
            if Dck(i) <= DcminR
               Dck(i) = DcminR;
```

```
            end
            gk(ga,i) = ceil(Dck(i-1)*Beta); % gi=g(i-1) will be the case whenever the fab limits are reached
            if gamma(ga) >= gamma_fablim && (l <= lkmin || gk(ga,i) <= gk_fablim)
               gk(ga,i) = gk_fablim;
               glim = gk_fablim;
               l = lkmin;
               q=1;
            elseif gamma(ga) < gamma_fablim && (l <= D0k_fablim || gk(ga,i) <= gk_fablim) %ASK ABOUT
THIS
               l=D0k_fablim; %lkmin to use
               gk(ga,i) = l/gamma(ga);
               glim = l/gamma(ga); %glim to use
               q=1;
            end
            Nk(i) = (Dck(i)/(1.4*gk(ga,i)))^(-1/0.48);
            DRmin(i) = Dck(i);
         end
         %calculating length of each section
          l=gk(ga,i)*gamma(ga);
          if gamma(ga) >= gamma_fablim && (l <= lkmin || gk(ga,i) <= gk_fablim)
             gk(ga,i) = gk_fablim;
             glim = gk_fablim;
             l = lkmin;
             q=1;
          elseif gamma(ga) < gamma_fablim && (l <= D0k_fablim || gk(ga,i) <= gk_fablim)
             l=D0k_fablim; %lkmin to use
             gk(ga,i) = l/gamma(ga);
             glim = l/gamma(ga); %glim to use
             q=1;
          end
          yk(ga,i) = ceil(Nk(i))*(gk(ga,i)+l);
          %L(j,i) = sum(yk(j,1:i));
      %Second loop that will be used after reaching fabrication
      %limits
      else
         Dck(i) = Dck(i-1)/SSF;
         if Dck(i) <= DcminR
            Dck(i) = DcminR;
         end
         gk(ga,i) = glim; % gi=g(i-1) will be the case whenever the fab limits are reached
         Nk(i) = (Dck(i)/(1.4*gk(ga,i)))^(-1/0.48);
         DRmin(i) = Dck(i);
         yk(ga,i) = ceil(Nk(i))*(gk(ga,i)+l);
         %L(j,i) = sum(yk(j,1:i));
      end
      q=0;
      if i==1
         yk_normalized = yk;
         yk_normalized(:,i) = yk(:,i)./yk(1,i);
      else
         yk_normalized(:,i) = yk(:,i)./yk(1,i);
      end
      %clear Dck gk
   end
%    figure;
%    plot(gamma,(yk(:,i)')./1000,'-o')
%    title(strcat('Length vs Gamma for section',num2str(i)))
%    xlabel('Gamma')
%    ylabel('Section length (mm)')
end
```

```
%end of function
end
```

******script******

```
clear all

%Outputs of function CP_DLD_gamma are [yk,gk,Dck],
%where yk is matrix with length values for each section (columns) and each
%gamma value (rows), gk is matrix with gap values for each section (columns) and each
%gamma value (rows), and Dck an array of particle size being filter by each
%section

% CIRCLE PILLARS
%% Select the desire DR, NoS, and gamma_min
%(can modify other values as desired except for gamma_max)
%Variables related to particule sizes
Dp_min = 1;
Dp_max = 100;
%Number of sections (each section will be k)
NoS_k = 5;
%Parameters to evaluate pillar diameter to gap ratio
gamma_min = 0.3;
gamma_step_less1 = 0.3;
gamma_step_high1 = 0.3;
gamma_max = 3;
%Fabrication limits
gk_fablim = 10;
D0k_fablim = 10;

%Calling function "CP_DLD_gamma"
[yk,yk_normalized,gk,Dck,gamma] = ...
    CP_DLD_gamma(Dp_min,Dp_max,gamma_min,gamma_step_less1,...
    gk_fablim,D0k_fablim,NoS_k,gamma_max,gamma_step_high1);

%*****Plots*****
figure;bar3(yk_normalized)
xlabel('k, section number')
ylabel('Gamma')
set(gca,'YTick',1:length(gamma))
set(gca,'YTickLabel',gamma)
%yticklabels(num2str(gamma))
zlabel('Length, L (normalized)')

figure;bar3(yk./1000)
xlabel('k, section number')
ylabel('Gamma')
set(gca,'YTick',1:length(gamma))
set(gca,'YTickLabel',gamma)
%yticklabels(num2str(gamma))
zlabel('Section length (mm)')

%% Fig. 7 of the paper
Dp_array = [0.01 1];
NoS = [5 10];
for i=1:length(Dp_array)
```

```
    for NoS_k=1:length(NoS)   %Number of sections (each section will be k)
        %Variables related to particule sizes
        Dp_min = Dp_array(i);
        Dp_max = 10;
        %Parameters to evaluate pillar diameter to gap ratio
        gamma_min = 0.3;
        gamma_step_less1 = 0.3;
        gamma_step_high1 = 0.3;
        gamma_max = 3;
        %Fabrication limits
        gk_fablim = 10;
        D0k_fablim = 10;

        %Calling function "CP_DLD_gamma"
        [yk,yk_normalized,gk,Dck,gamma] = ...
            CP_DLD_gamma(Dp_min,Dp_max,gamma_min,gamma_step_less1,...
            gk_fablim,D0k_fablim,NoS(NoS_k),gamma_max,gamma_step_high1);

        %*****Plots*****
        figure;bar3(yk_normalized)
        xlabel('k, section number')
        ylabel('Gamma')
        set(gca,'YTick',1:length(gamma))
        set(gca,'YTickLabel',gamma)
        zlabel('Length, L (normalized)')
        title(strcat('Dp_min =',num2str(Dp_min),' and NoS = ',num2str(NoS(NoS_k))))

        figure;bar3(yk./1000)
        xlabel('k, section number')
        ylabel('Gamma')
        set(gca,'YTick',1:length(gamma))
        set(gca,'YTickLabel',gamma)
        zlabel('Section length (mm)')
        title(strcat('Dp_min =',num2str(Dp_min),' and NoS = ',num2str(NoS(NoS_k))))

    end
end

%% Fig.8 and Fig. 9: Total length of a device vs NoS for different Dp values
col_array = ['b','g','m'];
Dp_array = [0.01 0.1 1];
NoS_init = 2;
figure;
for i=1:length(Dp_array)
    for NoS_k=1:10
        %Variables related to particule sizes
        Dp_min = Dp_array(i);
        Dp_max = 10;
        %Parameters to evaluate pillar diameter to gap ratio
        gamma_min = 0.3;
        gamma_step_less1 = 0.3;
        gamma_step_high1 = 0.3;
        gamma_max = 3;
        %Fabrication limits
        gk_fablim = 10;
        D0k_fablim = 10;

        %Calling function "CP_DLD_gamma"
        [yk,yk_normalized,gk,Dck,gamma] = ...
```

```
        CP_DLD_gamma(Dp_min,Dp_max,gamma_min,gamma_step_less1,...
        gk_fablim,D0k_fablim,NoS_k,gamma_max,gamma_step_high1);

    for j=1:NoS_k
        Min_length(j)=min(yk(:,j));
        s(i).gamma(NoS_k,j)=gamma(find(yk(:,j)==min(yk(:,j))));
    end
    if NoS_k==1
        TotalMinL_samegamma(i,NoS_k)=min(yk);
        TotalMinL_samegamma_value(i,NoS_k)=gamma(find(yk==min(yk)));
    else
        TotalMinL_samegamma(i,NoS_k)=min(sum(yk'));
        TotalMinL_samegamma_value(i,NoS_k)=gamma(find(sum(yk')==min(sum(yk'))));
    end

    LvsNoS(i,NoS_k)=sum(Min_length);
    clear Min_length
  end

  plot(NoS_init:NoS_k,LvsNoS(i,NoS_init:end)./1000,'--o','Color',col_array(i),'LineWidth', 2,'MarkerSize',5)
  %ylim([0 1000]) %[0 6]
  hold on

plot(find(LvsNoS(i,NoS_init:end)==min(LvsNoS(i,NoS_init:end))),LvsNoS(i,find(LvsNoS(i,NoS_init:end)==
min(LvsNoS(i,NoS_init:end))))/1000,...
      '*','Color','k','LineWidth', 2,'MarkerSize',9)
end
xlabel('NoS')
ylabel('Overall shortest length when using different gammas per section')
hold off

figure
for i=1:length(Dp_array)
  plot(NoS_init:NoS_k,LvsNoS(i,NoS_init:end)./TotalMinL_samegamma(i,NoS_init:end),'--
o','Color',col_array(i),'LineWidth', 2,'MarkerSize',5)
  hold on
end
xlabel('NoS')
ylabel('Ratio of overall shortest length using different gammas per section and shortest length using the same
gamma for all')
hold off
```

BIBLIOGRAPHY

BIBLIOGRAPHY

[1] World Health Organization, “Ambient (Outdoor) Air Quality and Health,” 2018.

[2] World Health Organization, “Household air pollution and health,” 2018.

[3] M. Ahmed Bhuiyan, H. U. Rashid Khan, K. Zaman, and S. S. Hishan, “Measuring the impact of global tropospheric ozone, carbon dioxide and sulfur dioxide concentrations on biodiversity loss,” *Environ. Res.*, vol. 160, no. July 2017, pp. 398–411, 2018.

[4] J. A. Bernstein *et al.*, “Health effects of air pollution,” *J. Allergy Clin. Immunol.*, vol. 114, no. 5, pp. 1116–1123, 2004.

[5] B. Freedman, “Chapter 16 ~ Gaseous Air Pollution” .

[6] A. Saxon and D. Diaz-Sanchez, “Air pollution and allergy: You are what you breathe,” *Nat. Immunol.*, vol. 6, no. 3, pp. 223–226, 2005.

[7] A. Heinzerling, J. Hsu, and F. Yip, “Respiratory Health Effects of Ultrafine Particles in Children: A Literature Review,” *Water. Air. Soil Pollut.*, vol. 227, no. 1, 2016.

[8] L. Martelletti and P. Martelletti, “Air Pollution and the Novel Covid-19 Disease: a Putative Disease Risk Factor,” *SN Compr. Clin. Med.*, vol. 2, no. 4, pp. 383–387, 2020.

[9] F. D. Xiao Wu, Rachel C Nethery, M Benjamin Sabath, Danielle Braun, “Exposure to air pollution and COVID-19 mortality in the United States: A nationwide cross-sectional study,” *Hilos Tensados*, 2020.

[10] N. G. Mowbray *et al.*, “Safe management of surgical smoke in the age of COVID-19,” *Br. J. Surg.*, 2020.

[11] D. Contini and F. Costabile, “Does air pollution influence COVID-19 outbreaks?,” *Atmosphere (Basel).*, vol. 11, no. 4, p. 377, 2020.

[12] L. Bourouiba, “Turbulent Gas Clouds and Respiratory Pathogen Emissions: Potential Implications for Reducing Transmission of COVID-19,” *JAMA - J. Am. Med. Assoc.*, vol. 323, no. 18, pp. 1837–1838, 2020.

[13] M. Oakes, L. Baxter, and T. C. Long, “Evaluating the application of multipollutant exposure metrics in air pollution health studies,” *Environ. Int.*, vol. 69, pp. 90–99, 2014.

[14] D. Dias and O. Tchepel, “Spatial and temporal dynamics in air pollution exposure assessment,” *Int. J. Environ. Res. Public Health*, vol. 15, no. 3, 2018.

[15] J. J. Zhang and P. J. Lioy, “Human exposure assessment in air pollution systems.,” *ScientificWorldJournal.*, vol. 2, no. August 2014, pp. 497–513, 2002.

[16] U.S. Environmental Protection Agency (EPA), “Criteria Air Pollutants.”

[17] Risk Assessment Forum and U. S. E. P. Agency, “Guidelines for Human Exposure Assessment Guidelines for Human Exposure Assessment,” no. October, 2019.

[18] S. Citation, *Human Exposure Assessment for Airborne Pollutants*. 1991.

[19] R. T. Burnett, M. Smith-doiron, D. Stieb, S. Cakmak, and J. R. Brook, “Effects of Particulate and Gaseous Air Pollution on Cardiorespiratory Hospitalizations,” *Arch. Environ. Health*, vol. 54, no. 2, pp. 130–139, 1999.

[20] “www.epa.gov/criteria-air-pollutants/naaqs-table.” .

[21] R. D. Brook, “Cardiovascular effects of air pollution,” *Clin. Sci.*, vol. 115, no. 6, pp. 175–187, 2008.

[22] bill Freedman, *Environmental Science: A Canadian Perspective*, vol. 14, no. 3. 2000.

[23] “www.valleyair.org.” [Online]. Available: www.valleyair.org.

[24] P. Hyde and A. Mahalov, “Contribution of bioaerosols to airborne particulate matter,” *J. Air Waste Manag. Assoc.*, vol. 70, no. 1, pp. 71–77, 2020.

[25] T. Šantl-Temkiv *et al.*, “Bioaerosol field measurements: Challenges and perspectives in outdoor studies,” *Aerosol Sci. Technol.*, vol. 54, no. 5, pp. 520–546, 2020.

[26] World Health Organization Press, “WHO Air quality guidelines for particulate matter, ozone, nitrogen dioxide and sulfur dioxide,” 2005.

[27] WHO, “Health Aspects of Air Pollution with Particulate Matter, Ozone and Nitrogen Dioxide,” *Rep. a WHO Work. Gr. Bonn, Ger. 13–15 January 2003*, no. January, p. 98, 2003.

[28] J. Curtius, “Nucleation of atmospheric particles,” in *EPJ Web of Conferences*, 2009.

[29] S. Salvador and E. Salvador, “Air Quality Index (AQI) Air Quality Communication Workshop,” 2012.

[30] L. B. Lave and E. P. Seskin, “Air pollution and human health,” *Science (80-.).*, 2013.

[31] B. O. Encyclopedia, “Air pollution,” 2020. .

[32] M. Kampa and E. Castanas, “Human health effects of air pollution,” *Environ. Pollut.*, vol. 151, no. 2, pp. 362–367, 2008.

[33] T. Boningari and P. G. Smirniotis, “Impact of nitrogen oxides on the environment and human health: Mn-based materials for the NOx abatement,” *Curr. Opin. Chem. Eng.*, vol. 13, no. x, pp. 133–141, 2016.

[34] K. H. Kim, E. Kabir, and S. Kabir, “A review on the human health impact of airborne particulate matter,” *Environ. Int.*, vol. 74, pp. 136–143, 2015.

[35] A. S. V Shah *et al.*, "Global association of air pollution and heart failure: A systematic review and meta-analysis," *Lancet*, vol. 382, no. 9897, pp. 1039–1048, Sep. 2013.

[36] M. Fu, F. Zheng, X. Xu, and L. Niu, "Advances of Study on Monitoring and Evaluation of PM2.5 Pollution," *Meteorol. Disaster Reduct. Res.*, vol. 34, pp. 1–6, 2011.

[37] Y. F. Xing, Y. H. Xu, M. H. Shi, and Y. X. Lian, "The impact of PM2.5 on the human respiratory system," *J. Thorac. Dis.*, vol. 8, no. 1, pp. E69–E74, 2016.

[38] WHO, "Health damage caused by fine particulate matter Fine particulate matter is a major health risk," *World Heal. Organ.*, 2015.

[39] and R.-H. X. Yi, Ye, Philip NP Lagniton, Sen Ye, Enqin Li, "COVID-19: what has been learned and to be learned about the novel coronavirus disease," *Int. J. Biol. Sci.*, vol. 16, no. 10, p. 1753, 2020.

[40] C. Wadman, M., Couzin-Frankel, J., Kaiser, J., & Matacic, "How does coronavirus kill," *Clin. trace a ferocious rampage through body, from brain to toes*, 2020.

[41] Pope CA III et al., "Lung cancer, cardiopulmonary mortality, and long-term exposure to fine particulate air pollution," *J. Am. Med. Assoc.*, vol. 287, no. 9, pp. 1132–1141, 2002.

[42] K. D. et Al, "Extended follow-up and spatial analysis of the American Cancer Society linking particulate air pollution and mortality," Boston, 2009.

[43] S. E. et Al, "Acute effects of ambient particulate matter on mortality in Europe and North America: results from the APHENA Study," *Environ. Health Perspect.*, vol. 116, no. 11, pp. 1480–1486, 2008.

[44] B. R. et Al., "Long-term effects of traffic-related air pollution on mortality in a Dutch cohort (NLCS-AIR Study)," *Environ. Health Perspect.*, vol. 116, no. 2, pp. 196–202, 2008.

[45] W. R. O. for Europe, "Air quality guidelines: global update 2005. Particulate matter, ozone, nitrogen dioxide and sulfur dioxide," Copenhagen, 2006.

[46] WHO, "Health Effects of Particulate Matter," 2013.

[47] B. Gelaye, M. Rondon, P. R. Araya, and P. M. A, "New methods for personal exposure monitoring for airborn particles," vol. 3, no. 10, pp. 973–982, 2016.

[48] S. S. Amaral, J. A. de Carvalho, M. A. M. Costa, and C. Pinheiro, "An overview of particulate matter measurement instruments," *Atmosphere (Basel).*, vol. 6, no. 9, pp. 1327–1345, 2015.

[49] E. A. Quality and P. H. Health, "Air Quality Measurements for Science and Policy Managing and Evaluating Air Quality to Protect Human Health and the Environment," no. May, 2012.

[50] I. Azzouz, F. Marty, and T. Bourouina, "Recent advances in micro-gas chromatography-The opportunities and the challenges," *Symp. Des. Test, Integr. Packag. MEMS/MOEMS, DTIP*

2017, no. May, 2017.

[51] T. V. Dinh, I. Y. Choi, Y. S. Son, and J. C. Kim, "A review on non-dispersive infrared gas sensors: Improvement of sensor detection limit and interference correction," *Sensors Actuators, B Chem.*, vol. 231, pp. 529–538, 2016.

[52] A. Dey, "Semiconductor metal oxide gas sensors: A review," *Mater. Sci. Eng. B Solid-State Mater. Adv. Technol.*, vol. 229, no. July 2017, pp. 206–217, 2018.

[53] H. Nazemi, A. Joseph, J. Park, and A. Emadi, "Advanced micro-and nano-gas sensor technology: A review," *Sensors (Switzerland)*, vol. 19, no. 6, 2019.

[54] C. Hagleitner *et al.*, "Smart single-chip gas sensor microsystem.," *Nature*, vol. 414, no. 6861, pp. 293–296, 2001.

[55] J. Philippe *et al.*, "Fully monolithic and ultra-compact NEMS-CMOS self-oscillator based-on single-crystal silicon resonators and low-cost CMOS circuitry," *Proc. IEEE Int. Conf. Micro Electro Mech. Syst.*, pp. 1071–1074, 2014.

[56] M. Y. Afridi *et al.*, "A monolithic CMOS microhotplate-based gas sensor system," *IEEE Sens. J.*, vol. 2, no. 6, pp. 644–655, 2002.

[57] S. Santra *et al.*, "ZnO nanowires grown on SOI CMOS substrate for ethanol sensing," *Sensors Actuators, B Chem.*, vol. 146, no. 2, pp. 559–565, 2010.

[58] M. L. Johnston, H. Edrees, I. Kymissis, and K. L. Shepard, "Integrated VOC vapor sensing on FBAR-CMOS array," *Proc. IEEE Int. Conf. Micro Electro Mech. Syst.*, no. February, pp. 846–849, 2012.

[59] S. K. Islam *et al.*, "Integrated circuit biosensors using living whole-cell bioreporters," *IEEE Trans. Circuits Syst. I Regul. Pap.*, vol. 54, no. 1, pp. 89–98, 2007.

[60] T. Tzeng *et al.*, "A Portable Micro Gas Chromatography System for Lung Cancer Associated Volatile Organic Compound Detection," vol. 51, no. 1, pp. 259–272, 2016.

[61] G. Barillaro and L. M. Strambini, "An integrated CMOS sensing chip for NO2 detection," *Sensors Actuators, B Chem.*, vol. 134, no. 2, pp. 585–590, 2008.

[62] H. Yin, X. Mu, H. Li, X. Liu, and A. J. Mason, "CMOS Monolithic Electrochemical Gas Sensor Microsystem Using Room Temperature Ionic Liquid," *IEEE Sens. J.*, vol. 18, no. 19, pp. 7899–7906, 2018.

[63] U.S. Environmental Protection Agency, "Integrated Review Plan for the National Ambient Air Quality Standards for Particulate Matter," p. 173, 2016.

[64] I. Priorities, *Research Priorities for Airborne Particulate Matter*. 1999.

[65] E. Kennedy, T. Fischbach, and R. Song, "Guidelines for air sampling and analytical method development and evaluation." p. 112, 1995.

[66] EPA, “List of designated reference and equivalent methods.” 2017.

[67] E. K. Ashley, D. Ph, and P. F. O. Connor, “NIOSH Manual of Analytical Methods (NMAM), 5th Edition Forew o rd,” *NIOSH Man. Anal. Methods*, no. 5th Edition, pp. 1–860, 2016.

[68] U S Environmental Group, “PARTICULATE MATTER (PM 2 . 5) SPECIATION GUIDANCE Final Draft,” 1999.

[69] K. Weingartner, E., Burtscher, H., HUGLIN, C., & Ehara, “Semi-Continuous Mass Measurement,” in *Aerosol measurement: principles, techniques, and applications*, 2011.

[70] J. Zhao, M. Liu, W. Wang, and J. Xie, “Airborne particulate matter classification and concentration detection based on 3D printed virtual impactor and quartz crystal microbalance sensor,” *Proc. IEEE Int. Conf. Micro Electro Mech. Syst.*, vol. 2016-Febru, pp. 824–827, 2016.

[71] “Libelium dust sensor.” .

[72] “Dylos Air quality monitor.” .

[73] “M-Dust Particle sensing unit.” [Online]. Available: https://www.vpen.it/index.php.

[74] “DFROBOT Air Quality Monitor.” [Online]. Available: https://www.dfrobot.com/product-1612.html.

[75] “Wynd-air-quality-tracker.” [Online]. Available: https://shop.hellowynd.com/products/wynd-air-quality-tracker.

[76] and R. S. Malings, Carl, Rebecca Tanzer, Aliaksei Hauryliuk, Provat K. Saha, Allen L. Robinson, Albert A. Presto, “Fine particle mass monitoring with low-cost sensors: Corrections and long-term performance evaluation.,” *Aerosol Sci. Technol.*, vol. 54, no. 2, pp. 160–174, 2020.

[77] I. Paprotny, F. Doering, and R. M. White, “MEMS Particulate Matter (PM) monitor for cellular deployment,” *Proc. IEEE Sensors*, pp. 2435–2440, 2010.

[78] R. M. White and J. Black, “Development of a Low-Cost Particulate Matter Monitor,” 2008.

[79] I. Paprotny, F. Doering, P. A. Solomon, R. M. White, and L. A. Gundel, “Microfabricated air-microfluidic sensor for personal monitoring of airborne particulate matter: Design, fabrication, and experimental results,” *Sensors Actuators, A Phys.*, vol. 201, pp. 506–516, 2013.

[80] R. M. White, “MICROFABRICATED PARTICULATE MATTER MONITOR,” 2014.

[81] D. J. Sorensen, C. M., Gebhart, J., O’Hern, T. J., & Rader, “Optical Measurement Techniques: Fundamentals and Applications,” in *Aerosol Measurement: Principles, Techniques, and Applications*, 2011.

[82] J. Pich, *Aerosol Measurement*, vol. 11, no. 2. 1980.

[83] X. Wang *et al.*, "A novel optical instrument for estimating size segregated aerosol mass concentration in real time," *Aerosol Sci. Technol.*, vol. 43, no. 9, pp. 939–950, 2009.

[84] T. Gao, "Integration of a Chemical sensor and a Particle detector," *Thesis*, no. May, 2012.

[85] L. Yuen, W. C. Chu, and B. Stoeber, "Microfluidic-based Real-time Detector for Fine Particulate Matter," 2014.

[86] X. Li *et al.*, "Miniaturized particulate matter sensor for portable air quality monitoring devices," *Proc. IEEE Sensors*, vol. 2014-Decem, no. December, pp. 2151–2154, 2014.

[87] M. Dong, E. Iervolino, F. Santagata, G. G. Zhang, and G. G. Zhang, "Silicon microfabrication based particulate matter sensor," *Sensors Actuators, A Phys.*, vol. 247, pp. 115–124, 2016.

[88] M. Dong, E. Iervolino, F. Santagata, G. Y. Zhang, and G. Zhang, "Integrated Virtual Impactor Enabled PM2.5 Sensor," *IEEE Sens. J.*, vol. 17, no. 9, pp. 1–1, 2017.

[89] K. Chun *et al.*, "MEMS for TPMS and exhaust of automobiles," *Proc. IEEE Sensors*, pp. 4–7, 2012.

[90] R. dan D. K. Hilmianti, "Peran Pememrintah Daerah dalam Pengelolaan Hutan Mangrove (Studi Kasus Di Kecamatan Padang Cermin Pesawaran Tahun 2010)," *J. Ilm. Adm. i Publik dan Pembang.*, vol. 2, no. 2, pp. 62–65, 2011.

[91] W. A. Tapie, D. Prato Garcia, and H. Sánchez Guerrero, "Biodegradación de vinazas de caña de azúcar mediante el hongo de pudrición blanca Pleurotus ostreatus en un reactor de lecho empacado," *Trop. Subtrop. Agroecosystems*, vol. 19, no. 2, pp. 145–150, 2016.

[92] M. Carminati *et al.*, "Capacitive detection of micrometric airborne particulate matter for solid-state personal air quality monitors," *Sensors Actuators, A Phys.*, vol. 219, pp. 80–87, 2014.

[93] P. Ciccarella, M. Carminati, M. Sampietro, and G. Ferrari, "Multichannel 65 zF rms Resolution CMOS Monolithic Capacitive Sensor for Counting Single Micrometer-Sized Airborne Particles on Chip," *IEEE J. Solid-State Circuits*, vol. 51, no. 11, pp. 2545–2553, 2016.

[94] D. Križaj, I. Iskra, and M. Remškar, "Numerical modeling of a capacitive type detector of airborne nanoparticles," *IFMBE Proc.*, vol. 37, pp. 1303–1306, 2011.

[95] I. Iskra *et al.*, "Capacitive-type counter of nanoparticles in air," *Appl. Phys. Lett.*, vol. 96, no. 9, 2010.

[96] K. Mohammad, D. A. Buchanan, and D. J. Thomson, "Integrated 0.35 pm CMOS capacitance sensor with atto-farad sensitivity for single cell analysis," *Proc. - 2016 IEEE Biomed. Circuits Syst. Conf. BioCAS 2016*, pp. 22–25, 2017.

[97] D. Križaj, I. Iskra, and M. Remškar, "(Quasi 3D) Numerical simulation of operation of a capacitive type nanoparticle counter," *J. Electrostat.*, vol. 69, no. 6, pp. 533–539, 2011.

[98] G. Jaramillo, C. Buffa, M. Li, F. J. Brechtel, G. Langfelder, and D. A. Horsley, "MEMS electrometer with femtoampere resolution for aerosol particulate measurements," *IEEE Sens. J.*, vol. 13, no. 8, pp. 2993–3000, 2013.

[99] C. Elbuken, T. Glawdel, D. Chan, and C. L. Ren, "Detection of microdroplet size and speed using capacitive sensors," *Sensors Actuators, A Phys.*, vol. 171, no. 2, pp. 55–62, 2011.

[100] T. Huang, Q. Kang, X. Zhu, Z. Zhang, and D. Shen, "Determination of water-soluble ions in PM2.5 using capillary electrophoresis with resonant contactless conductometric detectors in a differential model," *Anal. Methods*, vol. 5, no. 23, pp. 6839–6847, 2013.

[101] M. M. Mentele, J. Cunningham, K. Koehler, J. Volckens, and C. S. Henry, "Micro fluidic Paper-Based Analytical Device for Particulate Metals," *Anal. Chem.*, vol. 84, no. 10, pp. 4474–4480, 2012.

[102] P. Rattanarat, W. Dungchai, D. Cate, J. Volckens, O. Chailapakul, and C. S. Henry, "Multilayer paper-based device for colorimetric and electrochemical quantification of metals," *Anal. Chem.*, vol. 86, no. 7, pp. 3555–3562, 2014.

[103] M. Carminati, G. Ferrari, and M. Sampietro, "Emerging miniaturized technologies for airborne particulate matter pervasive monitoring," *Meas. J. Int. Meas. Confed.*, vol. 101, pp. 250–256, 2017.

[104] A. Thi and P. Tran, "Drone in Particulate Matter Measurement," no. May, 2019.

[105] J. Redelstein *et al.*, "Assessment of three-dimensional, fine-granular measurement of particulate matter by a smart air quality network in urban area," in *Proc. of SPIE*, 2019, no. October 2019, p. 20.

[106] J. Li *et al.*, "Spatiotemporal distribution of indoor particulate matter concentration with a low-cost sensor network," *Build. Environ.*, vol. 127, no. September 2017, pp. 138–147, 2018.

[107] Xiaoyi Mu, "Wearable Gas Sensor Microsystem for Personal Healthcare and Environmental Monitoring," 2013.

[108] Xiaoyi Mu, Zhe Wang, Min Guo, Xiangqun Zeng, and A. J. Mason, "Fabrication of a miniaturized room temperature ionic liquid gas sensor for human health and safety monitoring," *2012 IEEE Biomed. Circuits Syst. Conf.*, vol. 1, pp. 140–143, 2012.

[109] X. J. Huang, L. Aldous, A. M. Omahony, F. J. Del Campo, and R. G. Compton, "Toward membrane-free amperometric gas sensors: A microelectrode array approach," *Anal. Chem.*, vol. 82, no. 12, pp. 5238–5245, 2010.

[110] R. Toniolo, N. Dossi, A. Pizzariello, A. P. Doherty, and G. Bontempelli, "A Membrane Free Amperometric Gas Sensor Based on Room Temperature Ionic Liquids for the Selective Monitoring of NO x," *Electroanalysis*, vol. 24, no. 4, pp. 865–871, 2012.

[111] M. C. Buzzeo, C. Hardacre, and R. G. Compton, “Use of room temperature ionic liquids in gas sensor design,” *Anal. Chem.*, vol. 76, no. 15, pp. 4583–4588, 2004.

[112] A. J. Bard and L. R. Faulkner, *Electrochemical Methods: Fundamentals and Applications*, vol. 8. 2000.

[113] X. Mu, S. Member, Z. Wang, X. Zeng, A. J. Mason, and S. Member, “A Robust Flexible Electrochemical Gas Sensor Using Room Temperature Ionic Liquid,” *IEEE SENSORS*, vol. 13, no. 10, pp. 3976–3981, 2013.

[114] M. Ibrahim, J. Claudel, D. Kourtiche, and M. Nadi, “Geometric parameters optimization of planar interdigitated electrodes for bioimpedance spectroscopy,” *J. Electr. Bioimpedance*, vol. 4, no. 1, pp. 13–22, 2013.

[115] S. F. Cogan, J. Ehrlich, and T. D. Plante, “The effect of electrode geometry on electrochemical properties measured in saline,” *2014 36th Annu. Int. Conf. IEEE Eng. Med. Biol. Soc. EMBC 2014*, pp. 6850–6853, 2014.

[116] F. Zhang *et al.*, “Reference and counter electrode positions affect electrochemical characterization of bioanodes in different bioelectrochemical systems,” *Biotechnol. Bioeng.*, vol. 111, no. 10, pp. 1931–1939, 2014.

[117] D. Ruffatto, A. Parness, and M. Spenko, “Improving controllable adhesion on both rough and smooth surfaces with a hybrid electrostatic/gecko-like adhesive,” *J. R. Soc. Interface*, vol. 11, no. 93, 2014.

[118] J. Lee, G. Du Plessis, D. W. M. Arrigan, and D. S. Silvester, “Towards improving the robustness of electrochemical gas sensors: impact of PMMA addition on the sensing of oxygen in an ionic liquid,” *Anal. Methods*, vol. 7, no. 17, pp. 7327–7335, 2015.

[119] H. Yin, H. Wan, L. Lin, X. Zeng, and A. J. Mason, “Miniaturized planar RTIL-based eletrochemical gas sensor for real-time point-of-exposure monitoring,” *2016 IEEE Healthc. Innov. Point-of-Care Technol. Conf. HI-POCT 2016*, pp. 85–88, 2016.

[120] H. Yin, X. Mu, H. Li, X. Liu, and A. J. Mason, “CMOS Monolithic Electrochemical Gas Sensor Microsystem Using Room Temperature Ionic Liquid,” *IEEE Sensors J.*, vol. Accepted, 2018.

[121] A. U. Sardesai, V. N. Dhamu, A. Paul, S. Muthukumar, and S. Prasad, “Design and electrochemical characterization of spiral electrochemical notification coupled electrode (SENCE) platform for biosensing application,” *Micromachines*, vol. 11, no. 3, 2020.

[122] K. V. Singh, A. M. Whited, Y. Ragineni, T. W. Barrett, J. King, and R. Solanki, “3D nanogap interdigitated electrode array biosensors,” *Anal. Bioanal. Chem.*, vol. 397, no. 4, pp. 1493–1502, 2010.

[123] C. Gabrielli, M. Keddam, N. Portail, and P. Rousseau, “Model for Impedance Response of Micro-disk Electrodes in a Thin-Layer-Cell,” *ECS Meet. Abstr.*, p. 11620, 2006.

[124] R. L. Birke and Z. Huang, “Theoretical and Experimental Investigation of Steady-State

Voltammetry for Quasi-Reversible Heterogeneous Electron Transfer on a Mercury Oblate Spheroidal Microelectrode," *Anal. Chem.*, vol. 64, no. 14, pp. 1513–1520, 1992.

[125] Z. M. Zain *et al.*, "Development of an implantable d-serine biosensor for in vivo monitoring using mammalian d-amino acid oxidase on a poly (o-phenylenediamine) and Nafion-modified platinum-iridium disk electrode," *Biosens. Bioelectron.*, vol. 25, no. 6, pp. 1454–1459, 2010.

[126] H. Wan, H. Yin, and A. J. Mason, "Rapid measurement of room temperature ionic liquid electrochemical gas sensor using transient double potential amperometry," *Sensors Actuators, B Chem.*, vol. 242, pp. 658–666, 2017.

[127] E. E. Switzer, R. Zeller, Q. Chen, K. Sieradzki, D. A. Buttry, and C. Friesen, "Oxygen reduction reaction in ionic liquids: The addition of protic species," *J. Phys. Chem. C*, vol. 117, no. 17, pp. 8683–8690, 2013.

[128] H. Li, C. S. Boling, and A. J. Mason, "CMOS Amperometric ADC With High Sensitivity, Dynamic Range and Power Efficiency for Air Quality Monitoring," *IEEE Trans. Biomed. Circuits Syst.*, vol. 10, no. 4, pp. 817–827, Aug. 2016.

[129] J. H. Riemer, N., Ault, A. P., West, M., Craig, R. L. & Curtis, "Aerosol Mixing State: Measurements, Modeling, and Impacts," *Rev. Geophys.*, 2019.

[130] G. D. Lippmann, M., Chen, L.-C., Gordon, T., Ito, K. & Thurston, "National Particle Component Toxicity (NPACT) Initiative: integrated epidemiologic and toxicologic studies of the health effects of particulate matter components," *Res. Rep. Heal. Eff. Inst.*, vol. 5, p. 13, 2013.

[131] J. J. Shea, "Fundamentals and Applications of Microfluidics [Book Review]," *IEEE Electr. Insul. Mag.*, vol. 19, no. 5, pp. 73–73, 2003.

[132] R. Zengerle and H. Sandmaier, "MICROFLUIDICS," pp. 13–20, 2000.

[133] M. Masson *et al.*, "Sampling of suspended particulate matter using particle traps in the Rhône River: Relevance and representativeness for the monitoring of contaminants," *Sci. Total Environ.*, vol. 637–638, pp. 538–549, 2018.

[134] L. C. F. YUEN, "A REAL-TIME FINE PARTICULATE MATTER MONITOR BASED ON INERTIAL SIZE-SEPARATION AND OPTICAL DETECTION IN A MICROCHANNEL," 2015.

[135] S. Du, S. Shojaei-Zadeh, and G. Drazer, "Liquid-based stationary phase for deterministic lateral displacement separation in microfluidics," *Soft Matter*, vol. 13, pp. 7649–7656, 2017.

[136] V. Der Wijngaart, "A 3D microfluidic cage collector for airborne particles," pp. 79–81, 2015.

[137] G. Pardon, L. Ladhani, N. Sandström, M. Ettori, G. Lobov, and W. Van Der Wijngaart, "Aerosol sampling using an electrostatic precipitator integrated with a microfluidic interface,"

Sensors Actuators, B Chem., vol. 212, pp. 344–352, 2015.

[138] W. Sandström, Niklas, Frisk, T., Stemme, G., Van Der Wijngaart, N. Sandström, T. Frisk, G. Stemme, and W. Van Der Wijngaart, "Electrohydrodynamic enhanced transport and trapping of airborne particles to a microfluidic air-liquid interface," *Proc. IEEE Int. Conf. Micro Electro Mech. Syst.*, vol. 212, no. 3, pp. 595–598, 2015.

[139] W. Ladhani, Laila, Pardon, Gaspard, Meeuws, Hanne, Van Wesenbeeck, Liesbeth, Schmidt, Kristiane, Stuyver, Lieven, Van Der Wijngaart, "Sampling and detection of airborne influenza virus towards point-of-care applications," *PLoS One*, vol. 12, no. 3, 2017.

[140] T. Frisk, D. Rönnholm, W. Van Der Wijngaart, and G. Stemme, "A micromachined interface for airborne sample-to-liquid transfer and its application in a biosensor system," *Lab Chip*, vol. 6, no. 12, pp. 1504–1509, 2006.

[141] S. C. Hong, J. S. Kang, J. E. Lee, S. S. Kim, and J. H. Jung, "Continuous aerosol size separator using inertial microfluidics and its application to airborne bacteria and viruses," *Lab Chip*, vol. 15, no. 8, pp. 1889–1897, 2015.

[142] J. Choi, S. C. Hong, W. Kim, and J. H. Jung, "Highly Enriched, Controllable, Continuous Aerosol Sampling Using Inertial Microfluidics and Its Application to Real-Time Detection of Airborne Bacteria," *ACS Sensors*, vol. 2, no. 4, pp. 513–521, 2017.

[143] J. McGrath, M. Jimenez, and H. Bridle, "Deterministic lateral displacement for particle separation: a review.," *Lab Chip*, vol. 14, no. 21, pp. 4139–58, 2014.

[144] F. L. Doering, I. Paprotny, and R. M. White, "MEMS Air-Microfluidic Sensor for Portable Monitoring of Airborne Particulates," *Hilt. Head*, no. c, pp. 315–319, 2012.

[145] and I. P. D. Fahimi, O. Mahdavipour, T. Cados, T. Kirchstetter, P. Solomon, L. Gundel, R. M. White, M. Lunden, N. Fukushima, H. Nagai, M. Saitoh, "Mems Air-Microfluidic Lab-on-a-Chip Sensor for Personal Monitoring of Airborne Particulate Matter," 2016, no. June, pp. 336–339.

[146] I. Paprotny, F. Doering, P. A. Solomon, and M. Richard, "Microfabricated air-microfluidic sensor for personal monitoring of airborne," 2012.

[147] Y. Zhou, Z. Ma, M. Tayebi, and Y. Ai, "Submicron Particle Focusing and Exosome Sorting by Wavy Microchannel Structures within Viscoelastic Fluids," *Anal. Chem.*, vol. 91, no. 7, pp. 4577–4584, 2019.

[148] K. K. Zeming, S. Ranjan, and Y. Zhang, "Rotational separation of non-spherical bioparticles using I-shaped pillar arrays in a microfluidic device.," *Nat. Commun.*, vol. 4, p. 1625, 2013.

[149] S. Ranjan, K. K. Zeming, R. Jureen, D. Fisher, and Y. Zhang, "DLD pillar shape design for efficient separation of spherical and non-spherical bioparticles.," *Lab Chip*, vol. 14, no. 21, pp. 4250–62, 2014.

[150] L. R. Huang, "Continuous Particle Separation Through Deterministic Lateral

Displacement," *Science (80-.).*, vol. 304, no. 5673, pp. 987–990, 2004.

[151] K. K. Zeming, N. V. Thakor, Y. Zhang, and C.-H. H. Chen, "Real-time modulated nanoparticle separation with an ultra-large dynamic range," *Lab Chip*, vol. 16, no. 1, pp. 75–85, 2016.

[152] N. Li, Q. Zhou, X. Li, W. Chu, J. Adkins, and J. Zheng, "Electrochemical detection of free glycerol in biodiesel using electrodes with single gold particles in highly ordered SiO2 cavities," *Sensors Actuators, B Chem.*, vol. 196, pp. 314–320, 2014.

[153] Y. Zhou *et al.*, "Electrochemical sensor for determination of ractopamine based on aptamer/octadecanethiol Janus particles," *Sensors Actuators, B Chem.*, vol. 276, no. August, pp. 204–210, 2018.

[154] X. yue Chen, R. tian Ma, W. Ha, and Y. ping Shi, "Direct colorimetric detection of aspartic acid in rat brain based on oriented aggregation of Janus gold nanoparticle," *Sensors Actuators, B Chem.*, vol. 274, no. July, pp. 668–675, 2018.

[155] H. Li, X. Liu, L. Li, X. Mu, R. Genov, and A. Mason, "CMOS Electrochemical Instrumentation for Biosensor Microsystems: A Review," *Sensors*, vol. 17, no. 1, p. 74, Dec. 2017.

[156] C. Grenvall, C. Antfolk, C. Z. Bisgaard, and T. Laurell, "Two-dimensional acoustic particle focusing enables sheathless chip Coulter counter with planar electrode configuration," *Lab Chip*, vol. 14, no. 24, pp. 4629–4637, 2014.

[157] T. Geiling, "Fine Dust Measurement with Electrical Fields Concept for a Capacitive Setup," *23rd MICROMECHANICS MICROSYSTEMS Eur. Work.*, 2012.

[158] P. W. Oluwasanya, G. Rughoobur, and L. G. Occhipinti, "Comparison of analytical and numerical methods of obtaining coplanar capacitance of microelectrodes for particulate matter detection," *IEEE Sens. J.*, vol. 20, no. 15, pp. 1–1, 2020.

[159] Y. Huang and A. J. Mason, "Lab-on-CMOS integration of microfluidics and electrochemical sensors," *Lab Chip*, vol. 13, no. 19, pp. 3929–3934, 2013.

[160] L. Li, H. Yin, and A. J. Mason, "Epoxy Chip-in-Carrier Integration and Screen-Printed Metalization for Multichannel Microfluidic Lab-on-CMOS Microsystems," *IEEE Trans. Biomed. Circuits Syst.*, vol. 12, no. 2, pp. 416–425, 2018.

[161] Y. H. Ghallab and Y. Ismail, "CMOS based lab-on-a-chip: Applications, challenges and future trends," *IEEE Circuits Syst. Mag.*, vol. 14, no. 2, pp. 27–47, 2014.

[162] S. M. Khan, A. Gumus, J. M. Nassar, and M. M. Hussain, "CMOS Enabled Microfluidic Systems for Healthcare Based Applications," *Adv. Mater.*, vol. 30, no. 16, pp. 1–26, 2018.

[163] L. Li and A. J. Mason, "Post-CMOS parylene packaging for on-chip biosensor arrays," in *Proceedings of IEEE Sensors*, 2010, pp. 1613–1616.

[164] L. Li, X. Liu, W. A. Qureshi, and A. J. Mason, "CMOS amperometric instrumentation

and packaging for biosensor array applications," *IEEE Trans. Biomed. Circuits Syst.*, vol. 5, no. 5, pp. 439–448, 2011.

[165] A. Weltin *et al.*, "Cell culture monitoring for drug screening and cancer research: A transparent, microfluidic, multi-sensor microsystem," *Lab Chip*, vol. 14, no. 1, pp. 138–146, 2014.

[166] T. Datta-Chaudhuri, P. Abshire, and E. Smela, "System-on-chip considerations for CMOS fluidic and biointerface applications," *Proc. - IEEE Int. Symp. Circuits Syst.*, pp. 2009–2012, 2014.

[167] F. F López-Huerta *et al.*, "Alternative post-processing on a CMOS chip to fabricate a planar microelectrode array," *Sensors*, vol. 11, no. 11, pp. 10940–10957, 2011.

[168] H. Lee, Y. Liu, D. Ham, and R. M. Westervelt, "Integrated cell manipulation system - CMOS/microfluidic hybrid," *Lab Chip*, vol. 7, no. 3, pp. 331–337, 2007.

[169] D. Welch and J. B. Christen, "Seamless integration of CMOS and microfluidics using flip chip bonding," *J. Micromechanics Microengineering*, vol. 23, no. 3, 2013.

[170] Y. Huang and A. J. Mason, "Lab-on-CMOS integration of microfluidics and electrochemical sensors.," *Lab Chip*, vol. 13, no. 19, pp. 3929–34, 2013.

[171] L. Li and A. Mason, "Development of an integrated CMOS-microfluidic instrumentation array for high throughput membrane protein studies," in *Proceedings - IEEE International Symposium on Circuits and Systems*, 2014, pp. 638–641.

[172] T. Datta-Chaudhuri, P. Abshire, and E. Smela, "Packaging commercial CMOS chips for lab on a chip integration," *Lab Chip*, vol. 14, no. 10, p. 1753, 2014.

[173] M. Lindsay *et al.*, "Scalable hybrid integration of CMOS circuits and fluidic networks for biosensor applications," *2017 IEEE Biomed. Circuits Syst. Conf. BioCAS 2017 - Proc.*, vol. 2018-Janua, no. C, pp. 1–4, 2018.

[174] M. Lindsay *et al.*, "Heterogeneous Integration of CMOS Sensors and Fluidic Networks Using Wafer-Level Molding," *IEEE Trans. Biomed. Circuits Syst.*, vol. PP, pp. 1–10, 2018.

[175] J. H. Lau *et al.*, "Fan-Out Wafer-Level Packaging for Heterogeneous Integration," *IEEE Trans. Components, Packag. Manuf. Technol.*, vol. PP, pp. 1–17, 2018.

[176] J. H. Lau, *Fan-Out Wafer-Level Packaging*. .

[177] J. Lau *et al.*, "2018 IEEE 68th Electronic Components and Technology Conference Reliability of Fan-Out Wafer-Level Packaging with Large Chips and Multiple Re-Distributed Layers," *2018 IEEE 68th Electron. Components Technol. Conf.*, vol. 1, no. 2, pp. 1574–1582, 2018.

[178] J. Lau *et al.*, "Warpage Measurements and Characterizations of Fan-Out Wafer-Level Packaging with Large Chips and Multiple Redistributed Layers," *IEEE Trans. Components, Packag. Manuf. Technol.*, vol. PP, pp. 1–9, 2018.

[179] S. Y. N. Jiang, F. Yang, K. L. Chan, and Z. Ning, "Water solubility of metals in coarse PM and PM2.5 in typical urban environment in Hong Kong," *Atmos. Pollut. Res.*, vol. 5, no. 2, pp. 236–244, 2014.

[180] S. J. Kwon, F. R. F. Fan, and A. J. Bard, "Observing iridium oxide (IrOx) single nanoparticle collisions at ultramicroelectrodes," *J. Am. Chem. Soc.*, vol. 132, no. 38, pp. 13165–13167, 2010.

[181] S. Parsnejad, Y. Hu, H. Wan, E. Ashoori, and A. J. Mason, "Wide dynamic range multi-channel electrochemical instrument for in-field measurements," in *IEEE SENSORS*, 2016.

[182] M. M. Dysart, B. R. Galvis, A. G. Russell, and T. H. Barker, "Environmental particulate (PM2.5) augments stiffness-induced alveolar epithelial cell mechanoactivation of transforming growth factor beta," *PLoS One*, vol. 9, no. 9, 2014.

[183] Sigma-Aldrich Techinical Staff, "SIGMA-ALDRICH polystyrene latex beads," 2007.

[184] USEPA, "A Guide to Air Quality and Your Health," 2014.

[185] H. Yin, H. Wan, and A. J. Mason, "Separation and Electrochemical Detection Platform for Portable Individual PM2 . 5 Monitoring," in *IEEE International Symposium on Circuits and Systems*, 2017.

[186] L. S. McCarty, A. Winkleman, and G. M. Whitesides, "Ionic electrets: Electrostatic charging of surfaces by transferring mobile ions upon contact," *J. Am. Chem. Soc.*, vol. 129, no. 13, pp. 4075–4088, 2007.

[187] L. S. McCarty and G. M. Whitesides, "Electrostatic charging due to separation of ions at interfaces: Contact electrification of ionic electrets," *Angew. Chemie - Int. Ed.*, vol. 47, no. 12, pp. 2188–2207, 2008.

[188] K. Prather, S. M. Toner, L. G. Shields, M. Yandell, C. J. Gaston, and M. J. K. Moore, *Determination of the spatial and temporal variability of size-resolved PM2.5 composition and mixing state in multiple regions in California*. 2009.

[189] R. Thakur, D. Das, and A. Das, "Electret air filters," *Sep. Purif. Rev.*, vol. 42, no. 2, pp. 87–129, 2013.

[190] H. Zhang, J. Liu, X. Zhang, C. Huang, and X. Jin, "Design of electret polypropylene melt blown air filtration material containing nucleating agent for effective PM2.5 capture," *RSC Adv.*, vol. 8, no. 15, pp. 7932–7941, 2018.

[191] A. M. Schaap, W. C. Chu, and B. Stoeber, "Continuous size-separation of airborne particles in a microchannel for aerosol monitoring," *IEEE Sens. J.*, vol. 11, no. 11, pp. 2790–2797, 2011.

[192] S. Ranjan, K. K. Zeming, R. Jureen, D. Fisher, and Y. Zhang, "DLD pillar shape design for efficient separation of spherical and non-spherical bioparticles," *Lab Chip*, vol. 14, no. 21, pp. 4250–4262, 2014.

[193] L. R. Huang, “Continuous Particle Separation Through Deterministic Lateral Displacement,” *Science (80-.).*, vol. 304, no. 5673, pp. 987–990, 2004.

[194] E. Pariset, J. Berthier, C. Pudda, F. Navarro, B. Icard, and V. Agache, “Particle Separation with Deterministic Lateral Displacement (DLD): The Anisotropy Effect,” *Proceedings*, vol. 1, no. 5, p. 313, 2017.

[195] “www.EngineeringToolBox.com.” .

[196] E. Pariset *et al.*, “Purification of complex samples: Implementation of a modular and reconfigurable droplet-based microfluidic platform with cascaded deterministic lateral displacement separation modules,” *PLoS One*, vol. 13, no. 5, pp. 1–18, 2018.

[197] S. John A. Davis, David W. Inglis, Keith J. Morton, David A. Lawrence, Lotien R. Huang and and R. H. A. Y. Chou, James C. Sturm, “Deterministic hydrodynamics : Taking blood apart,” *Nat. Commun.*, pp. 1–8, 2006.

[198] S. Ranjan, K. K. Zeming, R. Jureen, D. Fisher, and Y. Zhang, “DLD pillar shape design for efficient separation of spherical and non-spherical bioparticles.,” *Lab Chip*, vol. 14, no. 21, pp. 4250–4262, 2014.

[199] N. M. Karabacak *et al.*, “Microfluidic, marker-free isolation of circulating tumor cells from blood samples,” *Nat. Protoc.*, vol. 9, no. 3, pp. 694–710, 2014.

[200] D. Holmes *et al.*, “Separation of blood cells with differing deformability using deterministic lateral displacement,” *Interface Focus*, vol. 4, no. 6, 2014.

[201] D. W. Inglis *et al.*, “Microfluidic device for label-free measurement of platelet activation,” *Lab Chip*, vol. 8, no. 6, pp. 925–931, 2008.

[202] S. H. Holm, J. P. Beech, M. P. Barrett, and J. O. Tegenfeldt, “Separation of parasites from human blood using deterministic lateral displacement,” *Lab Chip*, vol. 11, no. 7, pp. 1326–1332, 2011.

[203] K. K. Zeming, N. V. Thakor, Y. Zhang, and C. H. Chen, “Real-time modulated nanoparticle separation with an ultra-large dynamic range,” *Lab Chip*, vol. 16, no. 1, pp. 75–85, 2016.

[204] A. J. Laki, L. Botzheim, K. Iván, V. Tamási, and P. Civera, “Separation of Microvesicles from Serological Samples Using Deterministic Lateral Displacement Effect,” *Bionanoscience*, vol. 5, no. 1, pp. 48–54, 2014.

[205] S. John A. Davis, David W. Inglis, Keith J. Morton, David A. Lawrence, Lotien R. Huang and and R. H. A. Y. Chou, James C. Sturm, “Deterministic hydrodynamics-Taking blood apart,” *PNAS*, 2006.

[206] “Deterministic hydrodynamics: Taking blood apart -support,” 2006.

[207] S. H. Au *et al.*, “Microfluidic isolation of circulating tumor cell clusters by size and asymmetry,” *Sci. Rep.*, vol. 7, no. 1, pp. 1–10, 2017.

[208] A. Hochstetter *et al.*, "Deterministic Lateral Displacement – Challenges and Perspectives," *ACS Nano*, pp. 1–26, 2020.

[209] D. W. Inglis, J. A. Davis, R. H. Austin, and J. C. Sturm, "Critical particle size for fractionation by deterministic lateral displacement," *Lab Chip*, vol. 6, no. 5, pp. 655–658, 2006.

[210] J. Yeom, D. D. Agonafer, J. H. Han, and M. A. Shannon, "Low Reynolds number flow across an array of cylindrical microposts in a microchannel and figure-of-merit analysis of micropost-filled microreactors," *J. Micromechanics Microengineering*, vol. 19, no. 6, 2009.

[211] R. Vernekar, T. Krüger, K. Loutherback, K. Morton, and D. W. Inglis, "Anisotropic permeability in deterministic lateral displacement arrays," *Lab Chip*, vol. 17, no. 19, pp. 3318–3330, 2017.

[212] D. Inglis, "The fluidic resistance of an array of obstacles and a method for improving boundaries in deterministic lateral displacement arrays-ESM," p. 368, 2020.

[213] K. K. Zeming, T. Salafi, C. H. Chen, and Y. Zhang, "Asymmetrical Deterministic Lateral Displacement Gaps for Dual Functions of Enhanced Separation and Throughput of Red Blood Cells," *Sci. Rep.*, vol. 6, no. February, pp. 1–10, 2016.

[214] J. a Davis *et al.*, "Deterministic hydrodynamics: taking blood apart.," *Proc. Natl. Acad. Sci. U. S. A.*, vol. 103, no. 40, pp. 14779–14784, 2006.

[215] S. C. Kim, B. H. Wunsch, H. Hu, J. T. Smith, R. H. Austin, and G. Stolovitzky, "Broken flow symmetry explains the dynamics of small particles in deterministic lateral displacement arrays," *Proc. Natl. Acad. Sci. U. S. A.*, vol. 114, no. 26, pp. E5034–E5041, 2017.

[216] K. Loutherback, K. S. Chou, J. Newman, J. Puchalla, R. H. Austin, and J. C. Sturm, "Improved performance of deterministic lateral displacement arrays with triangular posts," *Microfluid. Nanofluidics*, vol. 9, no. 6, pp. 1143–1149, 2010.

[217] T. Kulrattanarak *et al.*, "Mixed motion in deterministic ratchets due to anisotropic permeability," *J. Colloid Interface Sci.*, vol. 354, no. 1, pp. 7–14, 2011.

[218] R. Vernekar, T. Krüger, K. Loutherback, K. Morton, and D. W. Inglis, "Anisotropic permeability in deterministic lateral displacement arrays," *Lab Chip*, 2017.

[219] E. Pariset, J. Berthier, C. Pudda, F. Navarro, B. Icard, and V. Agache, "Particle Separation with Deterministic Lateral Displacement (DLD): The Anisotropy Effect," *Proceedings*, vol. 1, no. 10, p. 313, 2017.

[220] E. Pariset *et al.*, "Anticipating Cutoff Diameters in Deterministic Lateral Displacement (DLD) Microfluidic Devices for an Optimized Particle Separation," *Small*, vol. 13, no. 37, pp. 1–11, 2017.

[221] S. Feng, A. M. Skelley, and D. Inglis, "Solving the DLD boundary problem using iterative CFD," *22nd Int. Conf. Miniaturized Syst. Chem. Life Sci. MicroTAS 2018*, vol. 4, no. November, pp. 2063–2066, 2018.

[222] D. Inglis, R. Vernekar, T. Krüger, and S. Feng, “The fluidic resistance of an array of obstacles and a method for improving boundaries in deterministic lateral displacement arrays,” *Microfluid. Nanofluidics*, vol. 24, no. 3, pp. 1–8, 2020.

[223] K. K. Zeming, T. Salafi, C. H. Chen, and Y. Zhang, “Asymmetrical Deterministic Lateral Displacement Gaps for Dual Functions of Enhanced Separation and Throughput of Red Blood Cells -supplement,” vol. 4, no. 1, pp. 51–60, 2016.

[224] S. Feng, A. M. Skelley, and D. Inglis, “Solving the DLD boundary problem using iterative CFD,” *22nd Int. Conf. Miniaturized Syst. Chem. Life Sci. MicroTAS 2018*, vol. 4, no. December, pp. 2063–2066, 2018.

[225] J. Choi, J. C. Hyun, and S. Yang, “On-chip Extraction of Intracellular Molecules in White Blood Cells from Whole Blood,” *Sci. Rep.*, vol. 5, pp. 1–12, 2015.

[226] D. Inglis, “Thesis: Microfluidic Devices for Cell Separation,” no. September, p. 99, 2007.

[227] K. W. Oh, K. Lee, B. Ahn, and E. P. Furlani, “Design of pressure-driven microfluidic networks using electric circuit analogy,” *Lab Chip*, vol. 12, no. 3, pp. 515–545, 2012.